DISSECTING THE ROLES OF WHIP-TRIM14-PPP6C IN INNATE ANTIVIRAL IMMUNITY AND MYELOID BECLIN1 IN TUMOR IMMUNITY

A Dissertation

by

PENG TAN

Submitted to the Office of Graduate and Professional Studies of
Texas A&M University
in partial fulfillment of the requirements for the degree of

DOCTOR OF PHILOSOPHY

Chair of Committee,	Margie M. Moczygemba
Co-Chair of Committee,	Rongfu Wang
Committee Members,	Yubin Zhou
	Qi Cao
	Yi Xu
Head of Program,	Warren E. Zimmer

May 2018

Major Subject: Medical Sciences

ABSTRACT

The innate immune system has the ability to tune the inflammatory environment by modulating pathogen-recognition receptors (PRRs) signaling, which can either induce oncogenic changes or generate antitumor immunity through cross-talking with adaptive immunity. Thus, tight regulation of innate immune signaling pathways is essential either for an effective immune response against viral infections and tumor or for preventing detrimental autoimmunity.

Mitochondrial antiviral-signaling protein MAVS acts as a central hub for RIG-I receptor proximal signal propagation. However, key components in the assembly of the MAVS mitochondrial platform that promote RIG-I mitochondrial localization and optimal activation are still largely undefined. Employing pooled RNAi and yeast two-hybrid screenings, we report that the mitochondrial adaptor protein TRIM14 provides a docking platform for the assembly of the mitochondrial signaling complex required for maximal activation of RIG-I-mediated signaling, consisting of WHIP and protein phosphatase PPP6C. Following viral infection, the ubiquitin-binding domain in WHIP bridges RIG-I with MAVS through the binding to polyUb chains of RIG-I at lysine 164. ATPase domain in WHIP contributes to the stabilization of RIG-I-dsRNA interaction. Moreover, phosphatase PPP6C is responsible for RIG-I dephosphorylation. Together, our findings define the WHIP-TRIM14-PPP6C mitochondrial signalosome required for RIG-I-mediated innate antiviral immunity.

Giving the embryonic lethality of Beclin1 (Becn1) homozygous mice, roles of myeloid Becn1 in cancer-associated inflammation and tumor immunity remain elusive. We demonstrate herein that mice with myeloid loss of Becn1 (*Becn1*$^{\Delta M}$) show high risk of precursor (pre)-B cell lymphoma associated with neutrophilia. Becn1 deficiency stabilizes neutrophil MEKK3

independent of autophagy, resulting in the aberrant p38 activation and exaggerated tumorigenic inflammation that triggers the expressions of PD-L1 and pro-survival genes in pre-B cells. Importantly, we identify low Becn1 expression of neutrophils correlates with programmed death ligand 1 (PD-L1) levels and cancer recurrence in patients with pre-B acute lymphoblastic lymphoma (ALL). In a mouse model of melanoma, expansion and infiltration of neutrophils and B cells due to Becn1 deficiency favor metastasis of B16 melanoma. Thus, homeostatic maintenance of Becn1 level in neutrophils will contribute to the outcome of the tumorigenic process of pre-B cells.

ACKNOWLEDGEMENTS

I would like to express my deepest gratitude to my supervisor, a well-known immunologist, Dr. Rong-Fu Wang, for his valuable time, extreme patience and huge support, and his intellectual contributions to my Ph. D. study and my development as a future scientist. He always gave me freedom to think independently and explore the unknown research areas. He provided all resources I would need and excellent research environment for my projects. Especially during my paper revisions, he taught me how to edit my manuscript and response letters sentence-by-sentence, which I learned and developed my skills in the writing and data presentations. He trained me with the highest standards and his dedication to the science inspired me and motivated me to be a creative graduate student with honesty and integrity.

I would also like to thank my program, dissertation committee and experts off-campus not only for their time and precious advice to my projects, but also their recommendations and endless support to my career development. To Dr. Margie Moczygemba, for scheduling each committee and qualify exams and for speeding my program progress toward graduation. To Dr. Yubin Zhou and Yun "Nancy" Huang for their scientific advices, technique supports and giving me a lot opportunity to attend scientific conferences and to develop grant writing skills, which I would also like to take this opportunity to thank the Crohn's & Colitis Foundation of America for giving me the student research fellowship award to explore the area of epigenetic regulation of innate lymphoid cell development in the context of inflammatory bowel diseases. To Drs. Dekai Zhang, Magnus Hook, Qi Cao and Yi Xu, for their brilliant comments and grateful help to my projects. I would like to express my special thanks to Dr. Mingyao Liu, for giving me the opportunity to study the G-protein coupled-receptor signaling in prostate stem cells and prostate

cancer *in vivo* TRAMP and *Pten*-null mouse model with the help with Drs. Weijia Luo and Kunrong Tan, where I gained the animal research experiences and skills and published my first co-first author paper. To Drs. Leng Han and Deqiang Sun, for their help in the analysis of the next-generation sequencing data and patient gene expression profiling. To Dr. James M. You, for providing me the precursor acute lymphoblastic leukemia/lymphoma patient samples and for teaching me the background knowledge and how to do hemato-pathological analysis in the pathogentic samples from my mouse and human studies.

Last but not the least, I would like to thank Helen Yicheng Wang and lab members of Dr. Rong-Fu Wang, for their love, encouragement, and assistance to my projects and personal life.

DEDICATION

To my grandma, my parents and my wife and son, to all of my wonderful friends and extended family for your continuous love, support, and encouragement.

CONTRIBUTORS AND FUNDING SOURCES

This work was supervised by Professor Rong-Fu Wang (Supervisor) of the Center for Inflammation and Epigenetics in Houston Methodist Research Institute, Weill Cornell Medicine of Cornell University, and a dissertation committee consisting of Professors Margie M. Moczygemba, Yi Xu, Dekai Zhang (former committee member), and Magnus Höök (former committee member) of the Center for Infectious and Inflammatory Diseases in Texas A&M Institute of Biosciences and Technology, and Professor Yubin Zhou of the Center for Translational Cancer Research in Texas A&M Institute of Biosciences and Technology, and Professor Qi Cao of the Center for Inflammation and Epigenetics in Houston Methodist Research Institute, Weill Cornell Medicine of Cornell University.

The RNA-sequencing and human Gene Expression Profile data analyzed for Chapter III were provided by Professor Leng Han of the Department of Biochemistry and Molecular Biology in the University of Texas Health Science Center at Houston McGovern Medical School and Professor Deqiang Sun of the Center for Epigenetics & Disease Prevention in Texas A&M Insitute of Biosciences and Technology. Human patient samples analyzed for Chapter III was provided by Professor James M. You of the Department of Hematopathology at the University of Texas MD Anderson Cancer Center. All work for the dissertation was completed independently by the student.

This work was made possible in part by grants from the National Institutes of Health (R01CA09327, https://www.nih.gov/), Cancer Prevention and Research Institute of Texas (RP170537, http://www.cprit.state.tx.us/), Department of Defense (DoD) Breast Cancer Research Program (BCRP) (W81XWH-16-1-0417, http://cdmrp.army.mil/bcrp/) and Golfer against cancer

foundation to Rong-Fu Wang. The funders had no role in study design, data collection, and analysis, decision to publish, or preparation of the dissertation.

NOMENCLATURE

APC	Antigen-presenting cell
APEX	Engineered ascorbate peroxidase
AMPK	AMP-activated protein kinase
BCL6	B-cell lymphoma 6
BCR	B cell receptor
BLNK	B cell linker protein
BTK	Bruton's tyrosine kinase
CAF	Cancer-associated fibroblasts
CAR	Chimeric antigen receptor
CARD	Caspase activation and recruitment domain
cGAS	Cyclic guanosine monophosphate-adenosine monophosphate (GMP-AMP) synthase
CRISPR	Clustered regularly interspaced short palindromic repeats
CSN5	COP9 signalosome 5
CTLA-4	Cytotoxic T lymphocyte antigen 4
DAMP	Damage-associated molecular patterns
DC	Dendritic cell
dLN	Tumor-draining lymph node
Drp1	Dynamin-related protein 1
EMCV	Encephalomyocarditis virus

FOXO1	Forkhead box O1
HECT	Homologous to E6-AP COOH terminus
HMGB1	High mobility group box 1
HSV-1	Herpes simplex virus-1
IFN	Interferon
IDO	Indoleamine 2,3-dioxygenase
IL	Interleukin
IRAK	IL-1 receptor-associated kinase
ISRE	IFN-stimulated response element
LAP	Microtubule-associated protein 1 light chain 3 (LC3)-associated phagocytosis
LGP2	Laboratory of genetics and physiology 2
LPS	lipopolysaccharide
MAM	Mitochondrial-associated membrane
MAPK	Mitogen-activated protein kinase
MAVS	Mitochondrial antiviral-signaling protein
MCL1	Myeloid cell leukemia 1
MDA5	Melanoma differentiation-associated protein 5
MDSC	Myeloid-derived suppressor cell
mTOR	Mechanistic target of rapamycin
mtROS	Mitochondrial reactive oxygen species
MyD88	Myeloid differentiation primary response gene 88
NET	Neutrophil extracellular trap
NF-κB	Nuclear factor-κB

Nrf2	Nuclear factor erythroid 2-related factor 2
NLR	Nuclear oligomerization domain (NOD)-like receptor
Opa1	Optic atrophy protein 1
PAMP	Pathogen-associated molecular pattern
Pax5	Paired box protein 5
PD-L1	Programmed death-ligand 1
PD-1	Programmed cell-death protein 1
PPP6C	Protein phosphatase 6 catalytic subunit
PRR	Pattern-recognition receptor
pre-B ALL	Precursor B cell acute lymphoblastic leukemia/lymphoma
RD	Repressor domain
RIG-I	Retinoic acid-inducible gene I
RIP	Receptor-interacting serine/threonine-protein kinase
RLR	RIG-I-like receptor
ROR	Retinoic acid related orphan receptor
SeV	Sendai virus
sgRNA	Single guide RNA
SLE	Systemic lupus erythematosus
SLO	Secondary lymphoid organ
STAT	Signal transducer and activator of transcription
SYK	Spleen tyrosine kinase
TBK1	TANK-binding kinase 1
TCR	T cell receptor

TdT	Terminal deoxynucleotidyl transferase
TNF	Tumor necrosis factor
TRIF	TIR-domain-containing adapter-inducing interferon-β
TRIM	Tripartite motif
TSC	Tuberous sclerosis complex
TLR	Toll-like receptor
VSV	Vesicular stomatitis virus
WHIP	Werner helicase-interacting protein 1

TABLE OF CONTENTS

Page

LIST OF FIGURES

Page

CHAPTER I

INTRODUCTION AND LITERATURE REVIEW

Innate sensing at the interface of immunity and cancer

Sensing of pathogen infection or tissue damage/injury by pattern recognition receptors (PRRs) of the host innate immune system triggers the activation or cross-activation of type I IFN, nuclear factor-κB (NF-κB), Mitogen-activated protein kinase (MAPK), and inflammasomes, leading to the production of pro-inflammatory cytokines [1, 2]. Rapid termination of the immune response by negative feedback inhibition protects the host from cytokine storm but also the viral immune-evasion mechanisms of the co-evolution of viruses with hosts [3]. Toll-like, Nod-like, RIG-like, AIM2-like, C-type lectin, OAS-like receptors are the primary cellular sensors and germline-encoded PRRs expressed not only in professional innate immune cells (i.e., macrophages, dendritic cells, etc.) but also in majority of non-hematopoietic cells epithelial cells, fibroblasts and endothelial cells [1]. Innate sensing is important for the defense of infection and sounds alarms when environmental and metabolic changes are detected to maintain tissue homeostasis. Dysfunctional or unbalanced innate sensing system is closely related to human diseases such as cancer (**Figure 1**). In this study, we discuss in particular the vital intracellular sensors of viral RNA or DNA and extracellular sensor on the plasma membrane, with a focus on RIG-I-like receptors (RLRs), cyclic GMP-AMP synthase (cGAS), and TLR4 in pathogen defense, cancer inflammation, and the cancer immunoediting [4].

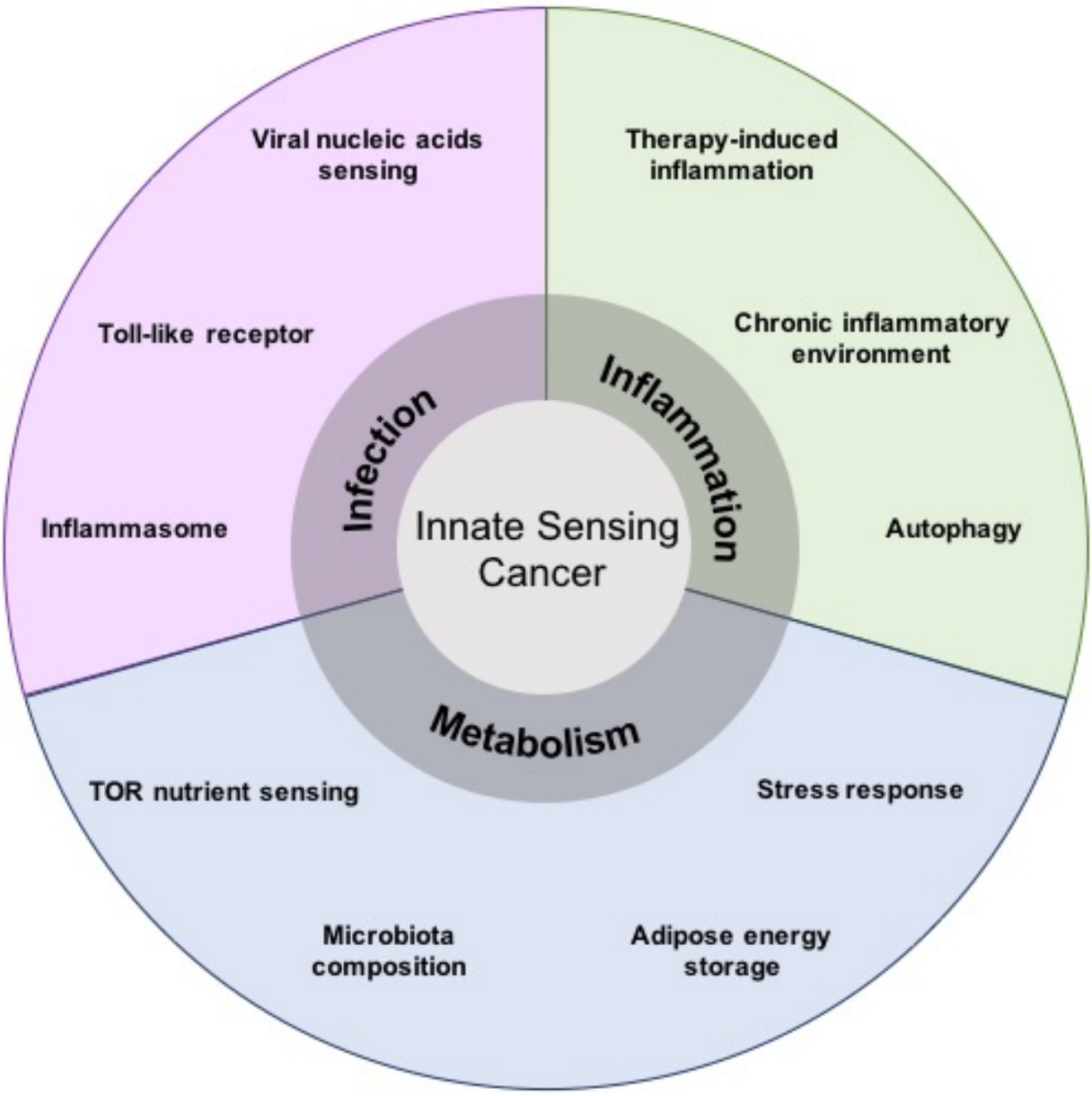

Figure 1. Innate sensing at the interface of innate immunity and cancer.
Innate sensing pathways including viral nucleic acids receptor, Toll-like receptor, and inflammasome pathways are critical for host protection against pathogen infections. Interplay between metabolic changes, microbial metabolites, and cellular degradation machinery shapes host innate immunity and inflammation status. Dysregulation of innate sensing and environmental immune response leads to chronic inflammation and cancer development.

RIG-I-like receptors and cGAS-STING

DExD/H-box RNA helicases of the RLR family are essential cytoplasmic sensors of RNA viruses. RLR family proteins comprises the retinoic acid-inducible gene-I protein (RIG-I, encoded by DDX58), melanoma differentiation-associated protein 5 (MDA5, encoded by IFIH1) and LGP2 (encoded by DHX58). RLRs harbor a central DExD/H-box helicase domain and a C-terminal regulatory domain (RD), which are both required for RNA binding. RIG-I and MDA5 also contain two tandem caspase recruitment domains (CARDs) at the N-terminus essential for activation of antiviral signaling. Whereas LGP2 does not have the CARD, its intact ATP hydrolysis activity exerts a synergetic effect with MDA5 on the effective antiviral response [5]. RIG-I recognizes 5'-triphosphate capped single-stranded RNA (5'ppp-ssRNA), short double-stranded RNAs (dsRNAs, up to 1 kb), such as the polyinosinic-polycytidylic acid (poly (I:C) and dsRNAs containing a 5'-triphosphate moiety transcribed from AT-rich dsDNA by RNA polymerase III. MDA5 detects long dsRNAs (more than 2 kb) [6]. Analyses of Rig-I$^{-/-}$ and Mda5$^{-/-}$ mice have shown that RIG-I is essential for the production of type I IFNs in response to various RNA viruses, including vesicular stomatitis virus (VSV), Sendai virus (SeV), whereas MDA5 is critical for the detection of picornaviridae such as encephalomyocarditis virus (EMCV). Post-translational modifications and regulatory host enzymes tightly control signaling transduction mediated by RIG-I and MDA5. In uninfected cells, RIG-I and MDA5 are constitutively phosphorylated by protein kinase C at serine or threonine residues in their CARDs, thus kept in an inactive state [7]. Besides, RIG-I is held in an auto-inhibitory closed configuration through the interaction of RD with CARD [3]. Binding of viral dsRNA releases the CARDs, resulting in a conformational change that permits removal of the phosphate groups at S8 and T170 of the RIG-I CARDs and S88 of the MDA5 CARDs by phosphatase PP1 [8]. Subsequent binding of K63 polyubiquitin (polyUb) chains to

RIG-I catalyzed by E3 ubiquitin ligases tripartite motif protein 4 (TRIM4), TRIM25 and Riplet (encoded by RNF135) induces tetramerization of RIG-I [9, 10]. A mitochondrial trafficking chaperone protein 14-3-3ε in complex with TRIM25 was then recruited for RIG-I translocation to mitochondria for interaction with the adaptor protein MAVS. It is still unclear if K63 ubiquitination mark is necessary for MDA5 signaling since the binding of MDA5 to long dsRNA is sufficient to trigger the formation of MDA5 filaments and binding to MAVS. Aggregation of MAVS into prion-like filament structures leads to the assembly of a large signaling platform and the recruitment of TBK1 and IKK to activate IRF3, IRF7 and NF-κB that leads to the production of interferons (IFNs) and proinflammatory cytokines such as TNF and Interleukin-6 (IL-6) [11]. Secreted IFNs can bind to IFN receptors through autocrine and paracrine fashions to induce JAK-STAT signaling and the expression of hundreds of IFN-stimulated genes (ISGs) which target critical steps of viral life-cycle as well as for shaping an effective adaptive immune response [12]. Cytoplasmic DNA sensor cGAS binds with viral dsDNA and produces the cyclic dinucleotide cyclic GMP-AMP (cGAMP) with an unusual 2'-5' phosphodiester bond. The second messenger cGAMP subsequently binds to endoplasmic reticulum (ER)-resident membrane adaptor protein STING (encoded by TMEM173), leading to the STING dimerization and K63 ubiquitination mediated by TRIM56 [13, 14]. Activated STING translocates from ER to Golgi apparatus and perinuclear regions where it interacts with TBK1 and triggers the activation of IRF3 and production of type I IFNs [11]. However, cGAS is not stable and either degraded by proteasome and autophagy pathways through ubiquitination and desumoylation or cleaved by caspase-1 upon inflammasome activation [15-17]. Deubiquitination by TRIM14-USP14 complex and sumoylation by TRIM38 ensures the protein stability of cGAS and optimal activation of the cGAS-STING pathway [16, 17].

Mitochondria as a signaling organelle in the regulation of innate immunity

Mitochondria as biosynthetic and bioenergetics cellular compartment contribute an active metabolic state to provide signaling intermediates during the immune response. Mitochondrial reactive oxygen species (mtROS) is critical for PRRs signaling such as nuclear oligomerization domain (NOD)-like receptors (NLRs) forming multi-subunit oligomers termed inflammasome. Diverse pathogen-associated molecular patterns (PAMPs) and damage-associated molecular patterns (DAMPs) including LPS, ATP, K^+, and uric acids lead to increase in ROS and lysosomal membrane permeabilization, resulting in NEK7-dependent NLRP3 activation, proteolytic cleavage and maturation of the pro-inflammatory cytokine IL-1β by activated caspase-1 [18, 19]. Following NLRP3 activation, caspase-1 inhibits mitophagy to induce mitochondrial damage [20] whereas NF-κB that primes NLRP3-inflammation for activation also prevents the excessive inflammasome-induced inflammation via inducing p62/SQSTM1 for Parkin-dependent mitophagic clearance [21]. Mitochondrial-associated membrane (MAM) provides a mitochondrial/endoplasmic reticulum interface for inter-organelle communication such as the regulation of mitochondrial fusion/fission, inflammasome formation and autophagy [22]. It serves as a signaling platform for RLR-activated antiviral immunity was evident by the identification of the RLR mitochondrial adaptor protein MAVS [23]. Notably, MAVS is also localized on the peroxisome membrane. While mitochondrial MAVS induces mainly the IRF3-dependent IFN β, peroxisomal MAVS induces IRF1-dependent type III IFN- λ [24]. Besides the antiviral function in immune cells, MAVS in the nonhematopoietic origin such as colonic epithelial cells is essential for protection against intestinal commensal bacteria and DSS-induced colitis through RIG-I detection of bacterial RNA species and production of cytokine IFN-β and antimicrobial peptides RegIIIγ [25]. Mitochondria dynamics are also critical for immune cell metabolism and function.

While healthy mitochondria display in a fused network promotes, mitochondria fission is indicative of damaged mitochondria that inhibits RLR signaling. Under nutrient-restricted conditions, mitochondria fuse into large interconnected networks that are essential to sustain intramitochondrial fatty acids exchange to maintain mitochondrial respiration and cell survival. By contrast, nutrient-rich and cellular damage condition promote mitochondrial fragmentation and degradation through mitophagy. Mitochondrial fission is regulated by GTPase dynamin-related protein 1 (Drp1) whereas mitochondrial fusion is regulated by mitofusin (Mfn)1 and 2 on the outer mitochondrial membrane and optic atrophy protein 1 (Opa1) on the inner mitochondrial membrane [26]. It is possible that lipids, metabolites or ROS released from mitochondria during mitochondrial morphological changes are necessary for optimal MAVS aggregation and activation [27]. MAVS is required for optimal NLRP3 inflammasome activation by mediating the recruitment of NLRP3 to mitochondria [28], suggesting the convergence of RLR signaling and NLRP3 inflammasome signaling on the mitochondria, although RNA viruses also activate NLRP3 inflammasome independent of RLR through RIP1 and RIP-3 complex-mediated Drp1 mitochondrial translocation and phosphorylation at Ser616 to induce aberrant mitochondrial fission [29]. Inter-organelle communication by a number of proteins with dual localization provides an inter-membrane integration point for innate immune signaling. Nuclear factor erythroid 2-related factor 2 (Nrf2) is normal sequestered and localized on the outer mitochondrial membrane. It becomes a key transcription factor for redox balance in response to mtROS oxidative stress which is also critical for optimal NF-κB activation [30]. Recent studies show that ubiquitin-binding autophagy receptor p62 is required for induction of hepatocellular carcinomas and pancreatic ductal adenocarcinoma through Nrf2 signaling [31, 32], suggesting a link between chronic inflammation and oncogenic transformation of epithelial tissues. Therefore, to understand

the signaling and metabolic events in the membrane contact sites are important for mounting an effective immune response and preventing overwhelming and detrimental cytokine storm.

TLR4 signaling

The stimulation of TLR4 by lipopolysaccharide (LPS) induces MyD88-dependent or TIR-domain-containing adapter-inducing interferon-β (TRIF)-dependent pathways, leading to the activation of NF-κB and MAPK or type I IFN signaling, respectively. Of note, intracellular LPS also activates caspase-11 non-canonical inflammasome independently of TLR4 [33]. On the other hand, NF-κB activation restricts inflammasome activation by eliminating damaged mitochondria by PARKIN-induced ubiquitination and p62 selective autophagy degradation [21]. TLR4 initiates innate immune responses by activating signaling pathways dependent on the adaptor myeloid differentiation primary response gene 88 (MyD88) that is sequentially inducing the activation of IL-1 receptor-associated kinase (IRAK) 1 and IRAK4, which in turn recruit the RING-domain E3 ubiquitin ligase, tumor necrosis factor (TNF)-receptor-associated factor (TRAF) 6. TRAF6-dependent activation of several MAP3Ks (TAK1, ASK1, MEKK3) in turn activate IKK complex or MKKs to activate downstream MAPKs 1) MKK1 and MKK2 activate Erk1/2, 2) MKK3 and MKK6 activate p38 3) MKK4 and MKK7 activate JNK [34]. In the TRIF-dependent pathway, TRIF interacts with TRAF6 and TRAF3. TRAF6 recruits receptor-interacting serine/threonine-protein kinase 1 (RIP1), which in turn activates TAK1 complex. TRAF3, on the other hand, recruits TBK1 for IRF3 activation to induce type I IFN genes. Although most cell types share general mechanism in the receptor signaling pathway, the manner of signaling transduction and amount of cytokine production differ in various types of cells [35].

Innate sensing in the immunosurveillance of cancer cells

The innate immune sensing of tumor-derived DNA and other DAMPs activates the cGAS-STING pathways in antigen-presenting cells (APCs). The resulted production of type I IFNs, in turn, enable and expand a subset of Batf3 or $CD103^+$ dendritic cells (DCs) recruited by tumor-derived CCL4 [36]. Matured $CD103^+$ DCs are able to transport intact tumor-antigens to tumor-draining lymph nodes and prime $CD8^+$ T cells, leading to the activation and clonal expansion of tumor antigen-specific cytotoxic $CD8^+$ T cells. $CD8^+$ T cells are recruited back to the tumor microenvironment under the influence of CXCL9 and CXCL10 and directly contact tumor cells, resulting in tumor cell death [37]. In a mouse model of melanoma, $CD103^+$ DCs were required to promote anti-PD-L1-mediated anti-tumoral effects when combined with FLT3L and poly (I:C) injections [36]. Radiotherapy and chemotherapy induce DNA double-stranded break damage to lead to the formation of micronuclei. cGAS is relocalized to the micronuclei and triggers the activation of inflammatory gene expression through cGAS-STING pathway [38]. Reports have described that T-cell-dependent antitumor response outside of the irradiated field, an abscopal effect most often seen in combination with anti-cytotoxic T lymphocyte antigen 4 (CTLA-4) immune checkpoint blockade. STING signaling is crucial for the regression of distal tumors in the combination of radiotherapy and anti-CTLA4 blockade. These findings suggest a model that cell cycle checkpoint inhibition by genotoxic therapies has the beneficial function in conjunction with immune checkpoint blockade through activation of local type I IFN production [39]. However, deletion of TBK1, the major downstream targets of STING and MAVS, in DCs displays a robust antitumor T cells response. These and other studies suggest that distinct nature of PAMPs, the signature of type I IFNs, and subtype of DCs might determine distinct roles in modulating the immunostimulatory function of DCs and antitumor T cell response [40-42]. Similarly, high

mobility group box 1 (HMGB1), a nuclear non-histone chromatin-binding protein released by necrotic cells activates TLR4 signaling but suppresses tumor-associated DCs activation through binding to the T-cell immunoglobulin and mucin-domain-containing-3 (TIM-3) [43, 44]. Thus, the study of innate immune signaling in pathogen defense might provide mechanistic insights into tumor immunity for therapeutic purposes.

TRIM family proteins in innate immunity and cancer

TRIM family proteins, most of which contain RING-finger domain and function as E3 ligase, play various roles in cellular processes including innate immune signaling, autophagy, development and carcinogenesis through post-translational modifications [45]. Typically, TRIM proteins are characterized by an N-terminal RING-finger domain for its E3 ligase function, one or two B boxes and its associated coiled-coil region, C-terminal PRY and SPRY domain (**Figure 2**). TRIM proteins have been shown to modulate protein stability through proteasome or autophagy pathways through ubiquitination [45]. Ubiquitin conjugation is catalyzed by the E1 ubiquitin-activating enzyme, E2 ubiquitin-conjugating enzymes, and E3 ubiquitin ligases. Base on the domain structure, E3 ligases have been classified into the homologous to E6-AP COOH terminus (HECT) family and the RING-finger-containing protein family. The linkage or conjugation of ubiquitin chain through seven internal lysine residues, including K6, K11, K27, K29, K33, K48 and K63, determines either the proteolytic function ubiquitin chain followed by proteasome- or autophagy- degradation, or non-proteolytic functions including protein kinase activation in innate immunity, histone regulation, protein translocation and DNA repair [45].

1) TRIM protein in innate immune signaling: TRIM30α suppresses NF-κB activation by promoting TLR-mediated TAB2 and TAB3 degradation [46]. TRIM56 induces K335 mono-ubiquitination of cGAS and TRIM14 recruits USP14 to cGAS K48 deubiquitination at K414 [17,

47]. TRIM25 and TRIM4 synthesize K63 ubiquitin chains of RIG-I at K172 and K164 respectively [48-50]. Although previously thought to mediate protection solely in the extracellular environment, recent studies have revealed that antibody-mediated protection extends to the cytosolic compartment of cells. Viral pathogens coated with antibody isotypes enter the cytosol, TRIM21 functioning as an Fc receptor is rapidly recruited and efficient neutralization occurs before the virus has had the time to replicate through its Ig binding PRY/SPRY domain [51]. By utilizing the antibody-binding activity of TRIM21, a recently developed method was reported for the degradation of endogenous proteins [52].

2) TRIM protein in autophagy: Proteins of TRIM family interact with cargo recognizing autophagy adaptor proteins (e.g., p62, NBR1, HDAC6, NIX, NDP52, OPTN), and autophagy core regulators ULK1 and Beclin1 to form a protein-recognition/degradation platform. For example, TRIM5α interacts with activated ULK1 and Beclin1 and concentrates them in specialized intracellular location for autophagy initiation. On the contrary, TRIM17 appears as a negative regulator of autophagy by altering the localization of ULK1, suggesting that co-localization of autophagic machinery with different TRIM proteins determines the activity of autophagy and localization of autophagosome [53, 54].

3) TRIM protein in cancer: Upregulation of TRIM59 have been found in gastric tumors and glioblastoma through modulating p53 stability and STAT3 activation, respectively [55, 56]. TRIM24 acts as a tumor suppressor in hepatocellular carcinoma via restricting retinoic acid receptor alpha (RARα)-mediating signaling [57]. AMP-activated protein kinase (AMPK) inhibits anabolic and facilitates catabolic processes to maintain energy homeostasis, which plays a tumor suppressor role in multiple cancers. For example, AMPK inhibits ACC1 and mechanistic target of rapamycin (mTOR) to block fatty acid synthesis and promotes autophagy via ULK1. In cancer,

growth-restrictive AMPK pathway is suppressed by cancer/testis antigen melanoma antigen (MAGE)-A3/6-TRIM28 complex [58]. TRIM29 lacking the RING-domain, the expression of which has an inverse relationship with TWIST1 in breast cancer, feedback inhibits TWIST1-mediated EMT and invasive phenotype of breast cancer [59]. TRIM29 as a histone-binding protein involves in DNA damage responses through phosphorylation of H2AX in response to ionizing radiation [60].

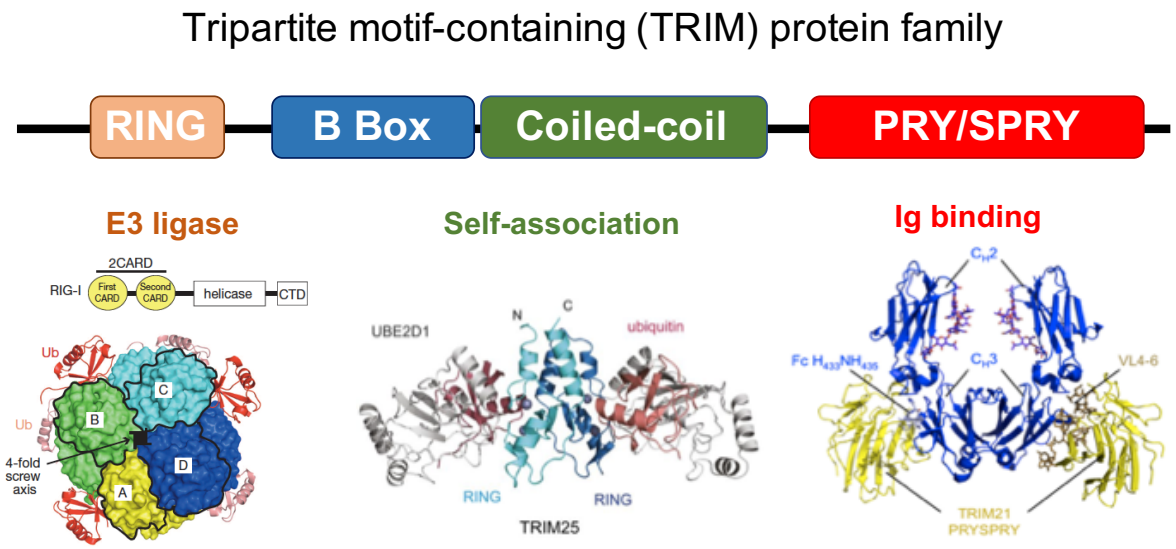

Figure 2. Functional domains of the tripartite motif-containing protein family. Adapted and reprinted from [49] and [61]. The conserved domains of known human TRIM proteins are represented schematically including an E3 ligase RING-finger domain [49], B box and coiled-coil domain for protein-protein interaction or self-association [61], and a C-terminal PRY/SPRY domain with a unique function in antibody binding.

B cell lymphomas: Intrinsic signaling and tumor microenvironment

B cell signaling and B cell malignancy

B cell-intrinsic signaling programs downstream of B cell receptor (BCR), TLR, CD40 and cytokine receptors affect B cell function, alternations in signaling lead to the pathogenesis of

autoimmunity and B cell malignancies. For example, enhanced positive signaling or disrupted negative signaling downstream of the pre-BCR promotes B cell acute lymphoblastic leukemia. Rearrangement of immunoglobulin heavy-chain variable (V), diversity (D) and joining (J) gene segments results in the expression of IgM heavy chain paired with non-polymorphic surrogate light chains to form pre-BCR at early B cell commitment stage or large pre-B cell stage. Chromosomal translocations and gene mutations at this stage give rise to B cell acute lymphoblastic leukemia/lymphoma such as BCR-ABL1 translocation, mutations in mixed-lineage leukemia (MLL) and pre-B cell leukemia homeobox1 (PBX1). Immature B cells acquire a functional BCR and egress from the bone marrow to complete maturation and differentiation into follicular B cells, marginal zone B cells and germinal center B cells in spleen or lymph nodes. According to different origins of B cell lymphomas in periphery, non-Hodgkin's B cell lymphomas are divided into 1) Circulating and follicular-derived: B cell chronic lymphocytic leukemia (CLL) (derives from mature CD5 positive B cells) and Mantle cell lymphoma, 2) Marginal zone-derived: splenic marginal zone lymphoma (SMZL) and mucosa-associated lymphoid tissue (MALT) lymphoma, and 3) Germinal center-derived: follicular lymphoma, diffuse large B cell lymphoma (DLBCL), Burkitt's lymphoma (BL), and multiple myeloma (plasma cell malignancy). Pre-B cell survival and proliferation is driven by IL-7R signaling, which induces the activation of STAT5. Pre-BCR signaling activation through CD79A/B activates spleen tyrosine kinase (SYK) and Bruton tyrosine kinase (BTK) phosphorylate the B cell linker protein (BLNK). BLNK inhibits the AKT activation, thereafter promoting the nuclear translocation of forkhead box protein O1 (FOXO1). FOXO1 targets the transcriptional repressor B cell lymphoma 6 (BCL6), which inhibits cyclin D2 and Myc. BLNK also suppresses STAT5 activation. Increased paracrine and autocrine IL-7 stimulation leads to excessive STAT5 activation in pre-B ALL patients. Inactivation

mutations in BLNK release the inhibition of AKT resulting in cytoplasmic retention of FOXO1 and lack of BCL6 expression. Hyperactivation of RAS pathway due to RAS mutations promotes ELK1 and cyclic AMP-responsive-element-binding protein (CREB) target genes. Two main modes of BCR signaling including tonic signaling, which is activated by PI3K and active signaling activates NF-kB by the CARD1-BCL-10-MALT1 complex. Alternations in pre-BCR and BCR signaling is closely linked to the pathogenic progression of B cell lymphomas. Thus, the intrinsic and tumor environmental stimuli that lead to oncogenic transformation of B cells are needed to be studied and reconciled.

Immune checkpoint in B cell malignancy

Stimulation of the TCR via major histocompatibility complex (MHC) antigen cross-presentation by APCs activates T cells. Co-stimulatory receptors and co-inhibitory receptors (or immune checkpoint molecules) co-localize with TCR at the immunological synapse where they promote or inhibit T cell activation and function [62, 63] (**Figure 3**). The finding of programmed cell-death protein ligand 1/2 (PD-L1/2) is upregulated in lymphoid malignancies whereas CTLA-4 and PD-1 receptors are highly expressed on tumor-infiltrating lymphocytes (TILs) [64]. The activation of CD28 initiates the membrane translocation of CTLA-4 to compete with CD28 for engaging with shared ligands CD80 and CD86, thus downregulates the T-cell response. In contrast to CTLA-4, PD-1 does not affect co-stimulation, whose expression requires 6-12 h transcriptional activation. PD-1 recruits phosphatase SHP-2 and PP2A to directly inhibit TCR signaling. PD-L1 and PD-L2 are expressed by tumor cells as well as infiltrating leukocytes upon exposure to IFN-γ produced by activated T cells or natural killer cells. Immune evasion through the aberrant expression of PD-L1 in B cell lymphomas that binds to PD-1 on $CD4^+$ and $CD8^+$ T cells induces T cell exhaustion [65, 66]. The clinical trial using anti-PD-1 antibody nivolumab and anti-PD-L1

antibody pembrolizumab have durable responses in non-small cell lung cancer and triple negative breast cancer. In B cell lymphoma, anti-PD-1 antibody pidilizumab phase I trial showed a response in more than 33% of patients including CLL and DLBCL. Studies have been focusing on the molecular mechanisms underlying the expression of PD-1/PD-L1 for better immunotherapies. Biallelic inactivation of *Lkb1* and *Pten* in lung leads to squamous cell carcinoma (SCC) expressing KRT5, p63 and SOX2 associated with infiltrated neutrophils. The $SCA1^{+}NGFR^{+}$ cell fractions in the SCC highly express PD-L1 leading to tumor immune escape [67]. Oncogene MYC was found to directly bind to the promoters of two immune checkpoint proteins, CD47 and PD-L1. MYC inactivation downregulates CD47 and PD-L1 leading to suppressed tumor growth, which could be reversed by ectopic expression of CD47 and PD-L1 [68]. Cyclin-dependent kinase 5 (Cdk5) is highly active in medulloblastoma as a critical mediator of IFN-γ-induced PD-L1 upregulation. Cdk5 deletion results in persistent expression of IRF2 and IRF2BP2, two transcriptional repressors of PD-L1, leading to potent $CD4^{+}$ T cell-mediated tumor rejection [69]. A recent study in commensal bacteria strain *Bifidobacterium* suggests an emerging role of the microbiome in the modulating of antitumor immunity by augmenting dendritic cells and enhancing $CD8^{+}$ T cell priming [70]. Combination therapy by oral administration of *Bifidobacterium* and anti-PD-L1 therapy abolishes tumor outgrowth [70]. In a mouse model of chronic inflammation-induced liver cancer, accumulation of IgA^{+} $B220^{-}$ $CD138^{+}$ B cells with elevated expression of PD-L1 and immunosuppressive phenotype that promotes HFD-induced liver cancer. Anti-PD-L1 antibody blockade induces liver cancer regression through clonal expansion of liver $CD8^{+}$ T cells [71]. Thus, how to identify the critical immune cell and stromal cell composition that dictates the local and systemic tumor microenvironment for tumor cell evasion and metastasis is important for the design of combination therapy to treat cancer.

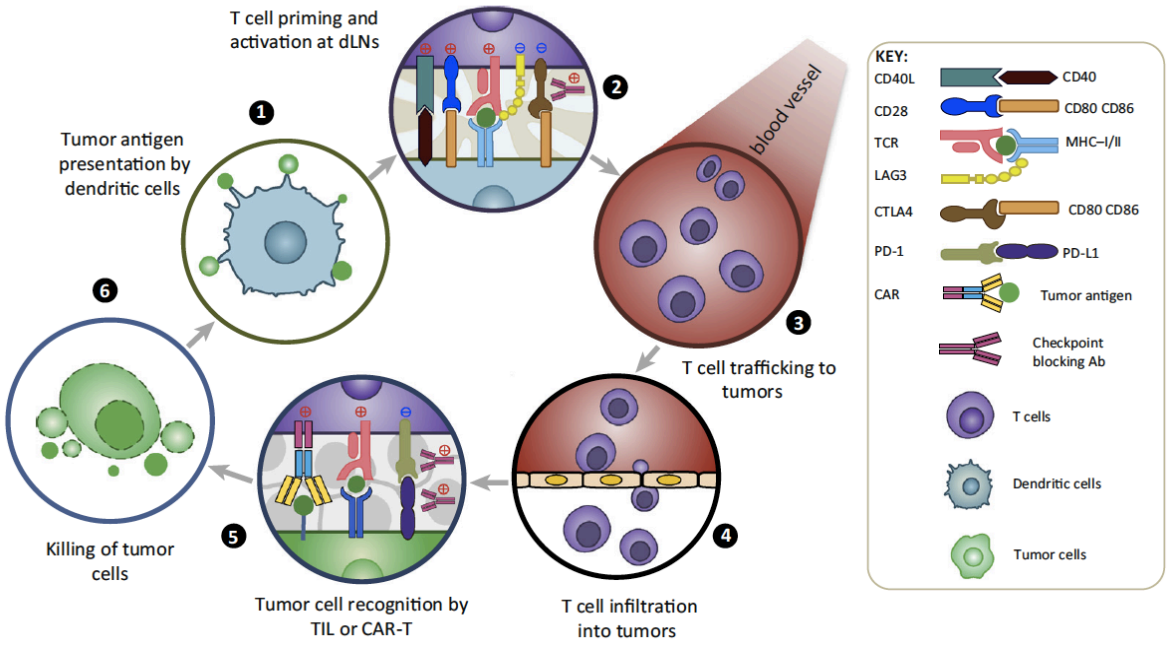

Figure 3. The cancer immunity cycle. Reprinted from [64]. A typical antitumor immune response involves the following major steps: (1) Tumor antigens are released and captured by DCs for processing; (2) DCs present processed antigens to T cells to prime and activate T cell receptor (TCR) signaling against tumor-specific antigens in tumor-draining lymph nodes (dLNs). T cell antitumor activity is balanced by the coordinated actions of both stimulatory (red-cross) and inhibitory (blue-cross) signals. (3) Activated effector T cells travel through blood vessels and (4) infiltrate tumor sites by crossing the endothelial barrier. (5) Tumor-infiltrating T cells (TILs) recognize cancer cells through the interaction between TCR and cognate antigens bound to MHC-I on tumor cells. Engineered therapeutic T cells expressing chimeric antigen receptor (CAR-T) are also used in the clinic to boost tumor killing. Immunomodulatory monoclonal antibodies can overcome local immunosuppression by blocking suppressive PD-1receptors and (6) eventually initiate the tumor cell killing machinery.

Multi-faceted roles of MDSCs in the tumor immunosuppression

MDSCs are one of the major components with potent immunosuppressive activity in tumor microenvironment through remodeling the tumor microenvironment and establishing pre-metastatic niche [72, 73]: 1) production of T cell suppressive cytokines arginase (Arg1), inducible NOS (iNos), reactive oxygen species (ROS); 2) suppressing T cell activity via deprivation of L-cysteine and L-arginine 3) TGF-β, IL-10 to induce regulatory T cells (Tregs). MDSCs are broadly defined as $CD11b^{+}$ myeloid cells, including $Ly6G^{+}Ly6C^{lo}$ polymorphonuclear (PMN)-MDSCs

(similar to neutrophils) and $Ly6G^{-}Ly6C^{hi}$ monocytic (M)-MDSCs. For example, accumulation of a subset of MDSCs, $CD14^{+}HLA\text{-}DR^{lo}$ M-MDSCs, in CLL patients has the capacity to inhibit T cells activation and induce Treg by indoleamine 2,3-dioxygenase (IDO) [74]. The increase of $CD66b^{+}CD33^{lo}$ HLA-DR^{-} PMN-MDSCs in peripheral blood was found with Arg1 activity in a cohort of 31 indolent lymphomas [75]. MDSCs has been recently shown to diminish the efficacy of immune checkpoint blockade. Anti-CTLA4 or anti-PD1/PD-L1 antibody checkpoint blockade generates a durable therapeutic response in a variety of cancer types but not prostate cancer. One of the mechanisms underlying patient resistance to immune checkpoint blockade is the observations of PMN-MDSCs accumulation in a prostate carcinoma mouse model and patients with metastatic castration-resistant prostate cancer [76, 77]. Specifically, Hippo-YAP signaling induces CXCL5 secretion by prostate cancer cells to attract CXCR2-expressing MDSCs. Cocktail inhibitors targeting MDSCs infiltration frequency and immunosuppressive activity (SX-682, Cabozantinib, BEZ235, PI-3065, GSK2636771) can synergize with immune checkpoint blockade to invigorate anti-tumor T cell response [76, 77]. Similarly, macrophage-derived TNF-α induces expression of COP9 signalosome 5 (CSN5) in tumor cells leading to the deubiquitination and stabilization of immune checkpoint molecule PD-L1. CSN5 inhibition by curcumin sensitizes tumor cells to anti-CTLA combinational therapies [78]. Interestingly, tumor-associated macrophages express PD-1 and M2-like surface profile. Blockade of PD-1/PD-L1 in vivo promotes macrophage phagocytosis and reduces tumor growth [79], suggesting that the immune checkpoint blockade therapy may also have a direct effect on the M2 subtype of tumor-associated macrophages.

Autophagy: Inflammation and Cancer

Autophagosome biogenesis and non-canonical autophagy

Autophagy, or macroautophagy, is a cellular homeostatic machinery involved in the disposal of the damaged organelle, invaded pathogens and denatured proteins through lysosomal degradation pathway, which have been intensively studied in the past decade [80, 81]. Under glucose starvation, AMPK promotes autophagy through phosphorylation of ULK1 at Ser317 and Ser777, a component of the autophagy initiation ULK1 complex (ULK1/ATG13/FIP200/ATG101) [82]. In resting state or nutrient abundant, the mTOR represses autophagy through phosphorylation of ULK1 at Ser757 thus disrupting the ULK1-AMPK interaction [82]. During nucleation stage, AMPK activates the PI3KC3 VPS34 complex (VPS34/Beclin1/VPS15/ATG14L) by phosphorylating S91/S94 in Beclin1 upon glucose withdrawal [83], while ULK1 phosphorylates Beclin1 at Ser14 [84] and enhances the activity of class III PI3K complex upon amino acid withdrawal. Of note, ULK1 is required only for short-term starvation where the VPS34 complex is needed for both long- and short-term starvation-induced autophagy [83]. In expansion stage, the ATG12-ATG5-ATG16L complex is recruited by phosphatidylinositol-3-phosphate (Ptdlns3P)-binding protein WIPI2 to the autophagosome precursor structure. The ATG16L1 complex is generated through ubiquitin-like conjugation reaction, in which ATG12 is conjugated to ATG5 by ATG7 and ATG10. ATG16L1 then non-covalently binds the ATG5-ATG12 conjugate to form a multimeric complex. In parallel, microtubule-associated protein 1 light chain 3 (LC3) is processed by the protease ATG4 and subjected to a second ubiquitin-like conjugation reaction via ATG7 and ATG3. ATG16L1 complex facilitates the lipidation of LC3 with phosphatidylethanolamine (PE) to form LC3-II [85]. LC3-II is recruited to autophagosomal membranes and is required for the fusion with lysosome-

mediated by class C vacuolar protein sorting (VPS) and SNARE-like proteins for both non-selective and selective autophagy-mediated degradation [86-88]. Subsets of canonical autophagy pathway have been observed to function independently of other components of the autophagy machinery. 1) LC3-associated phagocytosis (LAP): LAP mediates the maturation of phagosomes independently of the ULK1 complex but requires the NOX2, Rubicon, PI3KC3 complex and ATG16L1 complex [89]. 2) Brucella abortus-containing vacuole formation: Brucella abortus subverts the ULK1 and PI3KC3 complexes but not ATG16L1 or LC3 to generate pathogen-containing vacuoles [90]. 3)*Toxoplasma gondii* vacuole formation: Recruitment of immunity-related GTPase (IRGs) and guanylate-binding proteins (GBPs) to parasitophorous vacuole during *Toxoplasma gondii* or norovirus infections requires ATG16L1 complex but not autophagosome formation or lysosomes [91, 92]. Other examples such as ATG5 prevents neutrophil-inflammation during *Mycobacterium tuberculosis* infection independently of other components in ATG16L1 complex [93]. ATG9L1 represses STING pathway independently of LC3 conjugation [94].

Autophagy in inflammation and cancer

While studies had focused on the cell-autonomous nature of autophagy, it emerges that the autophagy-mediated tumor suppression is executed through suppression of chronic tumor-promoting inflammation and promotion of anti-tumor immunity [81, 95]. Autophagy in pre-malignant cells restrains their ability to establish chronic inflammation, by contributing to the elimination of damaged mitochondria and redox-active protein aggregates, interactions with inflammatory signaling molecules to limit the release of ROS, mtDNA and micronuclei to quench pro-inflammatory cytokines. For example, recruitment of ATG16L1 complex by NLRX1 and Tu translation elongation factor, mitochondrial (TUFM) to mitochondria promotes mitophagy leading to the removal of mitochondrial MAVS and suppressed type I IFN signaling [96]. Beclin1 binding

to cGAS induces autophagy to neutralize cytosolic DNA and inhibits cGAS-mediated type I IFN signaling [97]. cGAS generates cyclic dinucleotides that activate ULK1 leading to an inhibitory phosphorylation of STING [98]. In adipose tissue, a unique role of TBK1 in mediating the bidirectional crosstalk between inflammatory signaling pathway and energy sensing. The high-fat diet-induced TBK1 expression to repress AMPK to inhibit respiration and increase energy storage. On the other hand, TBK1 phosphorylates and induces IKK kinase NIK degradation, thus attenuating NF-κB activity. Activation of AMPK promotes catabolic processes and increase TBK1 activity through ULK1. Adipocyte-specific deletion of TBK1 increases energy consumption and inflammation-induced glucose tolerance [99]. p62 deficiency impairs the lysosomal localization and activation of mTORC1 in response to amino acids and Tuberous sclerosis complex 1 (Tsc1) deficiency. p63-MEKK3 complex activates MKK3/6 and subsequent activation of p38δ, which in turn feedback phosphorylates p62 and recruits TRAF6 for mTORC1 K63 ubiquitination and activation and expression of Myc. P62 levels differ in cancer cells and tumor microenvironmental stroma counterpart. While p62 high in cancer cells, induces NRF2 and mTORC1 signaling to suppress tissue oxidative toxicity to promote cancer cell growth, p62 low in stromal fibroblasts exhibits increased production of IL-6 that promotes TGF-β synthesis and formation of cancer-associated fibroblasts (CAF) [100, 101].

Intact autophagic responses in pre-malignant cells provide safeguard to the genetic homeostasis of healthy tissues. Beclin1 promotes tumorigenesis as evident by the spontaneous tumor formation in the mice with single-copy loss of beclin1. The similar phenotype can also be observed in mice ablated with the Beclin1-interacting proteins, Ambra1[102] and Bif-1[103]. Yet, how tumor regulates autophagy and whether autophagy affects tumor growth is controversial in a context-dependent manner [104, 105]. Post-translational modifications of Beclin1 may have roles

in determining the inducible or inhibitory function in autophagy-dependent and autophagy-independent responses. Study of Beclin1 acetylation status controlled by p300 and SIRT1 at K430 and K437 fine-tunes the autophagy induction and xenograft tumor growth. Mutant with both K430 and K437 substituted to arginines enhances autophagosome maturation and tumor growth suppression, suggesting acetylation of Beclin1 suppresses its function in autophagy induction [106]. Akt-mediated phosphorylation of Beclin 1 enhanced its interactions with 14-3-3 and vimentin intermediate filament proteins, and vimentin depletion increased autophagy and inhibited Akt-driven transformation. Thus, Akt-mediated phosphorylation of Beclin1 functions in autophagy inhibition, and the formation of an autophagy-inhibitory Beclin 1/14-3-3/vimentin intermediate filament complex to promote cancer growth. Expression of a Beclin1 mutant resistant to Akt-mediated phosphorylation increased autophagy, reduced anchorage-independent growth, and inhibited Akt-driven tumorigenesis [107]. Similarly, EGFR mediates Beclin1 phosphorylation in autophagy inhibition and tumor chemoresistance [108]. USP10 mediates the deubiquitination of tumor suppressor p53, mutual stabilization between deubiquitinase (USP10 and USP13) and Beclin1 provides a mechanism for Beclin1 to control the levels of p53 [109]. Small molecular specific and potent of autophagy inhibitor (spautin-1) targets USP10 and USP13, leading to suppression of Beclin1 and p53. Autophagy is a pro-survival mechanism in cancer cells in response to stress and starvation, inhibition of autophagy by spautin-1 may sensitize tumor cells to apoptosis under therapeutic stress. The mutual exclusion was found between Beclin1 and anti-apoptotic protein Mcl-1 by competing for a common deubiquitinase USP9X in an autophagy-independent manner. In a model of melanoma, Beclin1 restrains tumorigenesis by promoting Mcl-1 degradation [110]. Oncogenic H-Ras induces the expression of BH3-only protein Noxa, which displaces the Mcl-1 from Beclin1 thereby stabilizes Beclin1. Ablation of Noxa or Beclin1 attenuated Ras-

induced cell death, suggesting a mechanism that mediates caspase-independent but autophagy-dependent cell death by Ras [111]. Thus, the impact of Beclin1 on malignant transformation is complex and may involve processes independent of autophagy and cell-type specific role of autophagy, such as that of microenvironmental autophagy [112].

CHAPTER II

ASSEMBLY OF THE WHIP-TRIM14-PPP6C MITOCHONDRIAL COMPLEX PROMOTES RIG-I-MEDIATED ANTIVIRAL SIGNALING*

Introduction

Retinoic acid-inducible gene-I (RIG-I), as a major cytosolic sensor of viral double-stranded RNAs (dsRNAs), initiates an anti-viral immune response. In uninfected cells, RIG-I is kept in an inactive state by 1) an auto-inhibitory closed configuration through the interaction of C-terminal repressor domain with N-terminal caspase activation and recruitment domains (CARDs) [3] and 2) the constitutive phosphorylation of its CARD by protein kinase C [7]. Binding of viral dsRNA releases the CARDs, resulting in a conformational change that permits removal of the phosphate groups at S8 and T170 of the RIG-I CARDs by phosphatase PP1 [8]. Subsequent binding of K63 polyubiquitin (polyUb) chains to RIG-I induces oligomerization and translocation to mitochondria for interaction with MAVS, resulting in recruitment of kinases TBK1 and IKK ε to activate IRF3 that leads to the production of type I interferons (IFN-I) [9, 11]. Given the importance of RIG-I pathway in the antiviral immune response, the mechanisms that regulate RIG-I activation and mitochondrial translocation remain a topic of intense research. For example, K63 ubiquitination of RIG-I on lysine (K) 172 by TRIM25 was shown to be necessary for RIG-I mitochondrial targeting by chaperone protein 14-3-3ε [113]. However, K172R mutant is unable to entirely block the RIG-I activation induced by Sendai virus [114], suggesting the possibility of an alternative

* This chapter is reprinted and reused from "Assembly of the WHIP-TRIM14-PPP6C Mitochondrial Complex Promotes RIG-I-Mediated Antiviral Signaling". Peng Tan, Lian He, Jun Cui, Chen Qian, Xin Cao, Meng Lin, Qingyuan Zhu, Yinyin Li, Changsheng Xing, Xiao Yu, Helen Y. Wang, Rong-Fu Wang, 2017. Molecular Cell. 68(2):293-307. Copyright 2017 by Elsevier.

"ubiquitin-message" initiating RIG-I activation and signaling transduction. Recent studies have highlighted the importance of mitochondria as a central signaling platform, which participates in a broad range of innate immune pathways. For example, the adaptor MAVS associates NLRP3 on the mitochondrial membrane for inflammasome activation [115]. Yet, the temporal and spatial organization of the protein complex that builds a mitochondrial antiviral signalosome for RIG-I signaling transduction is still poorly defined. The recent study of RIG-I phosphorylation revealed a negative feedback mechanism by death-associated protein kinase 1 (DAPK1) [116]. Besides PP1, any phosphatase involved in the feedback regulation of RIG-I dephosphorylation is still elusive.

WHIP functions to promote RAD15 stabilization on ssDNA to maintain genomic stability at stalled replication forks through its ATPase activity [117]. In addition, WHIP contains an ubiquitin-binding zinc-finger domain (UBD) shown to bind polyUb chains during DNA repair [118]. However, the cytosolic function of this protein and its involvement, if any, in RLR-mediated IFN-I activation is mostly unclear. Recent studies also have identified PPP6C as a phosphatase for Aurora A for mitosis regulation and a key driver for skin basal cell carcinoma [119, 120]. Yet, the function of PPP6C in regulating IFN-I production has not been studied. By coupling IFN-stimulated response element (ISRE) reporter luciferase assay-based shRNA screening of TRIM family genes with yeast-two hybrid screening, we uncovered a more complex model of RIG-I activation than previously appreciated in that a feedback regulation of RIG-I activation and mitochondrial translocation by a mitochondrial membrane-associated complex containing TRIM14, WHIP, and PPP6C.

Methods and Materials

Cells and viruses

Human embryonic kidney (HEK) 293T (referred to as 293T cells), THP-1, and Vero cells were maintained in Dulbecco's modified Eagle medium (DMEM, ThermoFisher) supplemented with 10% fetal calf serum (Sigma Aldrich), 100 μg/ml penicillin, 100 μg/ml streptomycin (Sigma Aldrich) and non-essential amino acids (ThermoFisher). For stable expression of FLAG-RIG-I in 293T cells, entry clone of RIG-I (pENTR221-RIG-I) was subcloned into PFUWIG-CMV-FLAG-IRES-GFP-B vector for lentivirus packaging and subsequent 293T cells transduction. Cells were maintained in a humidified incubator with 5% CO2 at 37°C. To detect TRIM14 mRNA expression in human PBMC, T cells or B cells, buffy coats from healthy blood donors (obtained by the Gulf Coast Regional Blood Center, Houston, TX) were used for isolation of PBMCs by density-gradient centrifugation with Lymphoprep (Nycomed Pharm). The isolation and handling of PBMCs were done in accordance with institutional guidelines and protocols approved by Houston Methodist Research Institute. Human T cells and B cells were isolated from PBMC using Dynabeads™ Untouched Human T cells and B cells kit (ThermoFisher). EMCV, VSV (American Type Culture Collection) were amplified in Vero and 293T cells, respectively, and stored at -80ºC until used.

Cloning and plasmids

Expression constructs TRIM14, RIG-I, MDA5, LGP2 and MAVS, WHIP, PPP6C, PPP6R1, PPP6R2, and PPP6R3 were either generated from Entry clone library or were cloned from cells by RT-PCR using the gateway cloning system (ThermoFisher). Final constructs contained an affinity tag (FLAG, HA, Myc, or GFP) and were transcribed under the control of the CMV promoter. Deletion or truncation of TRIM14 (NT, 1-265), TRIM14 (CT, 266-442), WHIP (UBD, 1-245), WHIP (AAA+ATPase containing domain, 246-665) were generated from entry

clone by PCR and subcloned into final constructs containing affinity tag. Point mutations, including FLAG-RIG-I (K99), FLAG-RIG-I (K164R), FLAG-RIG-I (K169), FLAG-RIG-I (K172R), FLAG-RIG-I (K788R), HA/Myc-WHIP (D37A), HA/Myc-WHIP (T294A) HA-PPP6C (R85A), HA-PPP6C (H114Y), HA-PPP6C (K132N), HA-PPP6C (P186S), HA-PPP6C (R264C) were generated by using the QuickChange Lightning Multi Site-Directed Mutagenesis Kit (Agilent) as previously described [121].

Immunofluorescence assay and confocal microscopy

The immunofluorescence assays and confocal microscopy were conducted as described previously [122]. WT, *WHIP* KO, *MAVS* KO, or *TRIM14* KO 293T cells grown on glass-bottom dish (MatTek) in complete medium were co-transfected with fluorescently tagged expression vectors for RIG-I (DsRed2, GFP, or mCherry), TRIM14 (mCherry, or GFP), WHIP (tagBFP, or GFP), PPP6C (mCherry or GFP) or affinity tagged expression vectors for HA-WHIP, HA-PPP6C, HA-TRIM14 for 24 h. Cells were either left untreated or treated with poly(I:C)-LMW for 6 h. Cells were then fixed in 4% paraformaldehyde solution in PBS at room temperature for 15 min and permeabilized at room temperature with 0.1% Triton X-100/PBS. Subsequently, cells transfected with HA-WHIP, HA-PPP6C or HA-TRIM14 were incubated with anti-HA antibody in PBS containing 2% BSA for 16 h at 4°C. Specific antibodies for detecting endogenous TRIM14, RIG-I, MAVS, WHIP, and PPP6C were used in 1:200 dilution. Cells were then washed three times with PBS and incubated with secondary fluorescent antibody for 1 h. The nucleus was then labeled with DAPI for 5 min in the dark and then followed by three washes in PBS. Mitochondria were labeled with Deep Red (abs/em ~644/665 nm) Mitotracker fluorescent dye. ER was labeled with mCherry-sec61β. Samples were then visualized using Nikon Eclipse Ti-E microscope. All

acquired images were analyzed and the correlation coefficient (*r*) of pixel intensity values was extracted by using the Nikon NIS-Elements AR package or the ImageJ (NIH) software.

Protein fractionation by size-exclusion column

Size-exclusion chromatography was conducted as previously described [121]. Briefly, WT, *MAVS* KO and *TRIM14* KO THP-1 cells (5×10^7) were mock treated or infected with VSV for 12 h. Cells were lysed with low salt lysis buffer (50 mM Tris, pH7.5; 150 mM NaCl; 1% Triton-X; 5 mM EDTA; 10% (v/v) glycerol with protease inhibitor cocktail [Roche]) and then were centrifuged at 20,000 rpm for 20 min at 4°C. 10-100 μM protein samples were loaded onto a size-exclusion column (Superose 6 10/300 GL) with the capacity to separate the large protein complexes. Samples were fractionated in a buffer consisting of 20 mM Tris−HCl pH 7.3, 150 mM NaCl, 2 mM dithiothreitol and 0.6% N-lauroylsarcosine at a flow rate of 0.5 ml min−1 and collected as 0.5 ml fractions after passage through the void volume. SDS-PAGE separated protein fractions and detected by immunoblot with antibodies against WHIP, TRIM14, and PPP6C.

Immunoprecipitation and immunoblot analysis

For immunoprecipitation experiments, whole cell extracts obtained 24 h post-transfection or via ligand stimulation were lysed in low salt lysis buffer (50 mM Tris, pH7.5; 150 mM NaCl; 1% Triton-X; 5 mM EDTA; 10% (v/v) glycerol with protease inhibitor cocktail [Roche]) or RIPA buffer (150 mM NaCl, 1.0% IGEPAL® CA-630, 0.5% sodium deoxycholate, 0.1% SDS, 50 mM Tris, pH 8.0 protease inhibitor cocktail [Roche]) and shook on ice for 15 min. Whole cell lysates were incubated for 4 h at 4°C with the indicated antibodies and protein A/G beads (Pierce), or NeutrAvidin-beads for biotin-poly(I:C)-LMW pull-down or with anti-FLAG or anti-HA agarose gels for FLAG-tagged protein pull-down (Sigma). After incubation, beads were washed 5 times with 1 ml low salt lysis buffer or RIPA buffer, boiled with 4x SDS loading buffer, and subjected

to SDS-PAGE (Bio-Rad). Proteins were transferred to nitrocellulose membranes (Bio-Rad). Membranes were blocked in 5% dry milk/TBST for 1 h and incubated with using anti-HA, anti-Myc, anti-FLAG, RIG-I, MAVS, p-IRF3, IRF3, TRIM14, WHIP, PPP6C, phosphor-RIG-I (pS8 or pT170), or β-actin. Immunoblots were developed using the Luminata™ Western HRP Chemiluminescence Substrates (Millipore) and ChemiDoc™ XRS+ System with Image Lab (Bio-rad).

Luciferase reporter assay

293T (2 x 10^5) cells were seeded into 24-well plates the day before transfection. Cells were co-transfected with the IFN-β or ISRE promoter luciferase reporter and Renilla luciferase internal control (pRL-TK) using Lipofectamine 2000 (Invitrogen). Scrambled (control) shRNA and shRNA plasmids for TRIM family proteins (ThermoScientific) were utilized for ISRE reporter luciferase assay screening. Cells were stimulated with 2 μg RIG-I or MDA5 ligand poly(I:C)-LMW or poly(I:C)-HMW 24 h post-transfection. Empty pcDNA-HA/FLAG/Myc vector was used to ensure equal amounts of DNA among the wells. Luciferase activity was determined using the Dual-Luciferase Assay (Promega) with the Luminoskan Ascent Luminometer (Thermo Scientific) as previously described [123]. Reporter gene activity was normalized to the internal control.

Cytokine-release assay

Human IFN-β was detected using an ELISA kit (PBL Biomedical Laboratories) as previously described [124]. Briefly, diluted supernatants and human IFN-β standards were applied to the pre-coated 96-well plate and incubated for 2 h at room temperature. The plate was then washed and incubated with biotin-conjugated detection antibody (1:1000) for 1 h at room temperature. Next, the plate was washed and incubated with HRP conjugate concentrate for 30 min. The plate was washed and incubated with the tetramethylbenzidine (TMB) substrate

solution (Sigma-Aldrich). The reaction was stopped with 2 M H_2SO_4. The absorbance of each well was recorded at 450 nm. The absorbance of the standard sample was used to construct the standard curve.

Quantitative RT-PCR analysis

Total RNA was isolated from cells or tissues, and the first-strand cDNA was generated from total RNA using oligo-dT primers and reverse transcriptase II (Invitrogen). Quantitative RT-PCR (qRT-PCR) was performed using specific primers and the ABI Prism 7000 analyzer (Applied Biosystems) with SYBR® GreenER™ qPCR SuperMix Universal (Thermofisher). Target gene expression values were normalized to *hGAPDH*.

Construction of sgRNA/Cas9 LentiCRISPR and viral transduction

We designed human *TRIM14*, *WHIP,* and *PPP6C* sgRNAs using an online CRISPR design tool (crispr.mit.edu) by inputting targeted exon sequence. Four *hTRIM14* sgRNAs were designed and cloned into the BsmB1 site of lentiCRISPR vector containing Cas9-P2A-puromycin and were verified by sequencing analysis. The sgRNA-containing plasmids were transfected into 293 cells with pCMV-VSV-G plasmids and pΔ8.9. After two days, the virus-containing medium was subjected to ultracentrifugation (20,000 x g at 4°C for 2 h) and frozen at -80°C. 293 or THP-1 cells were transduced with control sgRNA or *TRIM14*-, *WHIP*-, or *PPP6C*-sgRNA-containing lentiCRISPR viruses. Transduced cells were selected in the presence of puromycin (Invivogen) for 48 h and subjected to ligand stimulation or viral infection.

Proteomic Mapping of TRIM14 Vesicle-like Puncta in HEK293 Cells

In situ biotin labeling of proteins located <20 nM of the TRIM14–APEX2 fusion protein was performed as previously described (Jing et al., 2015). A detailed protocol can be found at

Nature Protocol Exchange (http://www.nature.com/protocolexchange/protocols/4109). Briefly, the full-length of TRIM14 was cloned using primers EGFP-TRIM14-APEX2 forward 50-CGGCTTAAGATGGCGGGCGCGGCGACCGGG-30 and EGFP-TRIM14-APEX2 reverse 50-GAAGATCTGCGGGGCAGCCGGGGGATGC TGAT-30 to replace Connexin43 in pcDNA3 Connexin43-GFP-APEX2 (Addgene# 49385). HEK293 cells transfected with EGFP-TRIM14-APEX2 were externally treated with 500 mM Biotin-Phenol for 30 min at 37 ℃ and then treated with 3 mM freshly prepared H_2O_2 for exactly 1 min at room temperature. After 1 min of labeling, cells were washed three times with quencher solution (10 mM sodium azide, 10 mM sodium ascorbate, and 5 mM Trolox). Cells were then either subjected to immunofluorescent staining (IF) with Streptavidin DyLight 594 or lysed with 1X RIPA buffer for immunoprecipitation and mass spectrometry analysis.

Yeast two-hybrid screening

Yeast two-hybrid screening was carried out with the Matchmaker GAL4 Two-hybrid System 3 using the AH109 yeast strain. To construct a bait plasmid, full-length TRIM14 was cloned in-frame into the GAL4 DNA-binding domain of pGBKT7 (pGBKT7-TRIM14-BD). A human universal Matchmaker cDNA library (pGADT7-AD Mate & Plate^{TM} library) was used to screen ~1×10^6 clones. Transformed and mated cells were grown on –Leu, –Trp medium. TRIM14 interaction with WHIP or PPP6C was verified on high stringency plates (–Leu, –Trp, –His, –Ade) and with a β-galactosidase filter assay and Aureobasidin A (AbA) resistance in serial dilution (10-fold each).

Surveyor nuclease assay for genome modification

293T cells were transduced with control or *TRIM14*-sgRNA, *WHIP*-sgRNA, *PPP6C*-sgRNA, *RIG-I*-sgRNA and *MAVS*-sgRNA LentiCRISPR contructs. The transduced cells

underwent puromycin selection for 2 days (2 μg/ml). Genomic DNA was extracted using the Quick-gDNA Kit (Zymol Research) according to the manufacturer's protocol. The genomic region flanking the two CRISPR target sites was PCR amplified for sequencing: h-TRIM14 sgRNA-3 forward 5'-GGACTACAGGTGCATGCC-3', h-TRIM14 sgRNA-3 reverse 5'-CATTGGCTCCATATTGGG-3'; h-TRIM14 sgRNA-4 forward 5'-GTATATGCAATCCTCCTC-3', h-TRIM14 sgRNA-4 reverse 5'-CGGCCATGGTGGACACGG-3'; h-WHIP sgRNA-1/2 forward 5'-CCGGGGCAAACGGCCACGAAC-3', h-WHIP sgRNA-1/2 reverse 5'-GGCGCGTCGTAGCTCTCGCGG-3'; h-PPP6C sgRNA-1/2 forward 5'-GCCGAGCCTTCTAAATAAAG-3', h-PPP6C sgRNA-1/2 reverse 5'-CCAGCAGGTTTCGCGGGGTG-3'; h-RIG-I sgRNA forward 5'-GCACTTTGTGCTCAGTCACTG-3'; h-RIG-I sgRNA reverse 5'-GGCTTCCTCGGTGCGGAGGG-3'; h-MAVS sgRNA forward 5'-GTAATCCCCAAACTTGGGAGG-3'; h-MAVS sgRNA reverse 5'-CTGAGGCAGGAGAATCACTTG-3'. The PCR products were purified using the Gel DNA Recovery Kit (Zymol Research) according to the manufacturer's instructions. Purified PCR products from control and test cells were mixed and subjected to a reannealing process to produce heteroduplex formation according to the SURVEYOR Mutation Detection Kit (Transgenomic) protocol. After reannealing, products were treated with SURVEYOR nuclease and enhancer S (Transgenomic). The digested products were then subjected to electrophoresis on a 2% agarose gel with SYBR gold stain.

Statistical analysis

Descriptive statistics, including means, standard deviations, medians, and ranges, were computed for each group and analyzed with the Student's t-test or, for multiple comparisons, with ANOVA. Data are presented as the mean ± standard error. All analyses were performed with GraphPad Prism 6 (GraphPad Software, La Jolla, CA). P-values < 0.05 were considered significant.

Results

TRIM14 positively regulates RIG-I-mediated IFN-I signaling

To systematically analyze human TRIM proteins for their regulatory roles in efficient initiation and signaling of innate immunity, we performed a functional screening using pooled shRNAs (3 shRNAs per gene) targeting 42 TRIM family proteins in 293T cells. Among them, we identified TRIM14 as a potent positive regulator of poly(I:C)-LMW induced ISRE-Luciferase (Luc) reporter activity and RIG-I-mediated IFN-I signaling (**Figure 4A**).

To further define the positive role of TRIM14, we determined the status of IRF3 phosphorylation (p-IRF3) in CRISPR/Cas9-mediated *TRIM14* depleted 293T following stimulation with RIG-I receptor ligands such as intracellular poly(I:C)-LMW or VSV at various time points. *TRIM14* KO 293T and THP-1 cell clones using TRIM14 sgRNA-4 were generated for subsequent experiments. Notably, the extent of p-IRF3 was markedly diminished in *TRIM14* KO 293T cells after poly(I:C)-LMW stimulation or VSV infection (**Figures 4B and 4C**). Consistently, TRIM14 deficiency dramatically increased GFP-positive VSV replication during 24 h infection (**Figures 4D and 4E**).

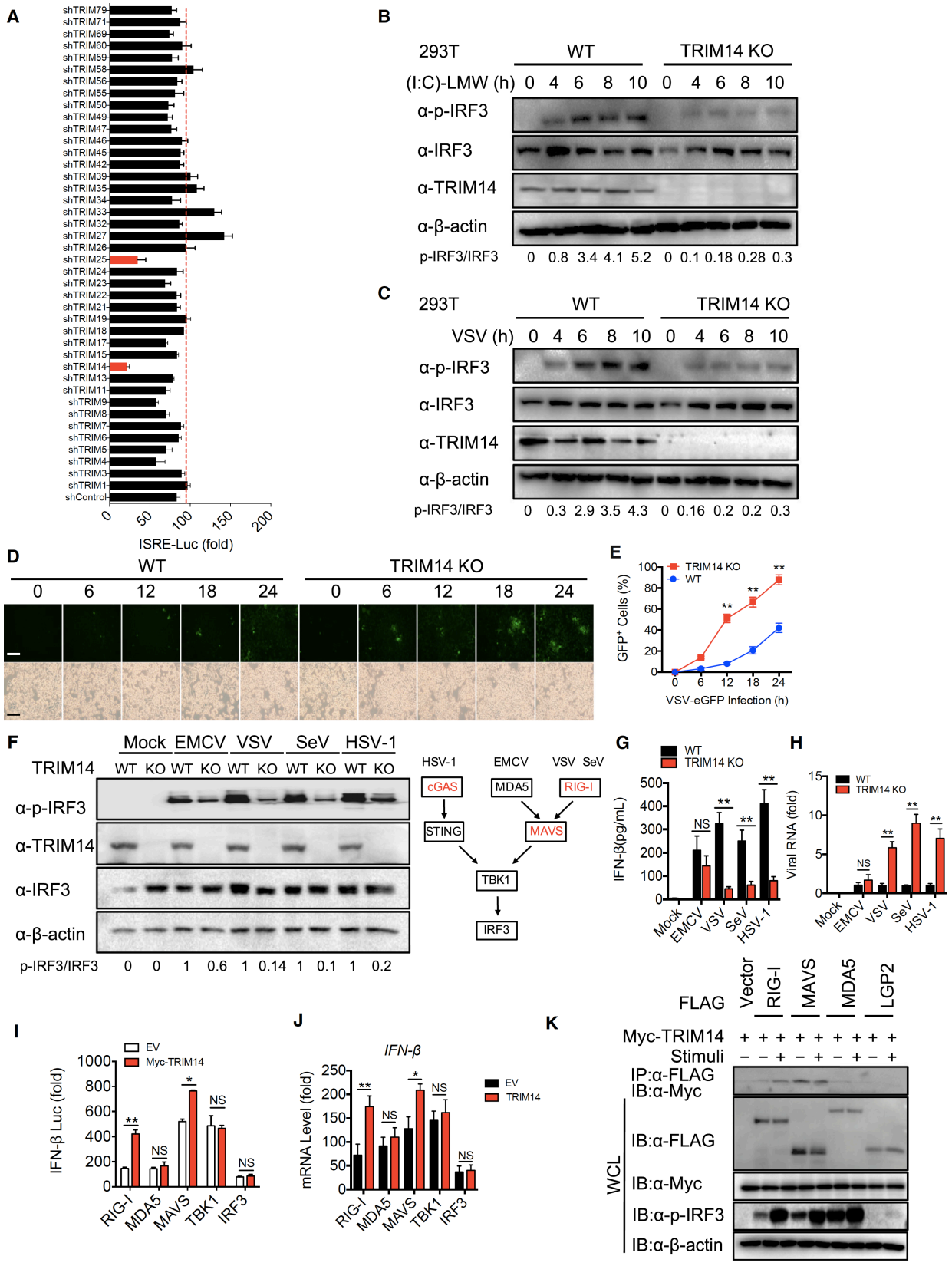
A
shTRIM79
shTRIM71
shTRIM69
shTRIM60
shTRIM59
shTRIM58
shTRIM56
shTRIM55
shTRIM50
shTRIM49
shTRIM47
shTRIM46
shTRIM45
shTRIM42
shTRIM39
shTRIM35
shTRIM34
shTRIM33
shTRIM32
shTRIM27
shTRIM26
shTRIM25
shTRIM24
shTRIM23
shTRIM22
shTRIM21
shTRIM19
shTRIM18
shTRIM17
shTRIM15
shTRIM14
shTRIM13
shTRIM11
shTRIM9
shTRIM8
shTRIM7
shTRIM6
shTRIM5
shTRIM4
shTRIM3
shTRIM1
shControl
0 50 100 150 200
ISRE-Luc (fold)
B
293T
WT
TRIM14 KO
(I:C)-LMW (h) 0 4 6 8 10 0 4 6 8 10
α-p-IRF3
α-IRF3
α-TRIM14
α-β-actin
p-IRF3/IRF3 0 0.8 3.4 4.1 5.2 0 0.1 0.18 0.28 0.3
C
293T
WT
TRIM14 KO
VSV (h) 0 4 6 8 10 0 4 6 8 10
α-p-IRF3
α-IRF3
α-TRIM14
α-β-actin
p-IRF3/IRF3 0 0.3 2.9 3.5 4.3 0 0.16 0.2 0.2 0.3
D
WT
TRIM14 KO
0 6 12 18 24 0 6 12 18 24
E
TRIM14 KO
WT
GFP+ Cells (%)
VSV-eGFP Infection (h)
F
Mock EMCV VSV SeV HSV-1
TRIM14 WT KO WT KO WT KO WT KO WT KO
α-p-IRF3
α-TRIM14
α-IRF3
α-β-actin
p-IRF3/IRF3 0 0 1 0.6 1 0.14 1 0.1 1 0.2
HSV-1
EMCV
VSV SeV
cGAS
MDA5
RIG-I
STING
MAVS
TBK1
IRF3
G
WT
TRIM14 KO
IFN-β(pg/mL)
Mock EMCV VSV SeV HSV-1
H
WT
TRIM14 KO
Viral RNA (fold)
Mock EMCV VSV SeV HSV-1
I
EV
Myc-TRIM14
IFN-β Luc (fold)
RIG-I MDA5 MAVS TBK1 IRF3
J
IFN-β
EV
TRIM14
mRNA Level (fold)
RIG-I MDA5 MAVS TBK1 IRF3
K
FLAG Vector RIG-I MAVS MDA5 LGP2
Myc-TRIM14 + + + + + + + + +
Stimuli − − + − + − + − +
IP:α-FLAG
IB:α-Myc
WCL
IB:α-FLAG
IB:α-Myc
IB:α-p-IRF3
IB:α-β-actin

Figure 4. TRIM14 positively regulates RIG-I signaling. (A) ISRE promoter luciferase assay of 293T cells transfected with control shRNA (shControl) or shRNAs (3 shRNAs per gene) targeting 42 TRIMs followed by stimulation with intracellular low-molecular-weight poly(I:C) ((I:C)-LMW) (5 μg/mL). Results are expressed relative to Renilla luciferase activity. Red dashed line indicates the average normal control shRNA activity. TRIM25 (positive control) and TRIM14 are highlighted in red. (B and C) IB analysis of WT and *TRIM14-deficient* (KO; TRIM14 sgRNA-4) 293T cells treated with poly(I:C)-LMW (B) or infected with VSV (C) for the indicated time points. (D and E) Fluorescence microscopy and phase-contrast of WT and *TRIM14 KO* 293T cells infected with VSV-eGFP (MOI=0.05) at the indicated time points (D). Images of living cells were captured to compare the degree of virus replication (GFP field, *top*) and virus cytopathic effect (bright field, *below*). Scale bars: 10 μm. Viral replication kinetics was indicated by the percentage of GFP^+ cells at the indicated time points (E). (F) IB analysis of WT and *TRIM14* KO (TRIM14 sgRNA-4) THP-1 cells infected with EMCV, VSV, SeV, or HSV-1 for 10 h. The diagram shows ligand-specific activation of antiviral IFN-I signaling pathways, including cGAS-STING by HSV-1, MDA5 by EMCV, and RIG-I by VSV and SeV (F, *right*). (G and H) ELISA of IFN-β production (G) and qPCR analysis of virus RNA (H) in WT and *TRIM14* KO THP-1 cells mock treated or infected with EMCV, VSV, SeV, or HSV-1 for 12 h. (I and J) IFN-β promoter luciferase assay (I) and IFN-β mRNA expression (J) in 293T cells co-expressing TRIM14 along with RIG-I, MDA5, MAVS, TBK1, or IRF3. (K) Co-IP and IB analysis of 293T cells co-transfected with Myc-TRIM14 and FLAG-RIG-I, MAVS, MDA5, or LGP2, followed by stimulation (VSV for RIG-I and MAVS; EMCV for MDA5 and LGP2) for 8 h. WCL, immunoblot analysis of whole-cell lysates without immunoprecipitation. Data in (A), (E), (G-J) are expressed as means ± SD of three independent experiments. *$p<0.05$, **$p<0.01$, NS: not significant, versus controls.

We next determined whether knockout of TRIM14 would inhibit IFN-I activation under physiological conditions. We treated WT and *TRIM14* KO THP-1 cells with various viruses targeting different DNA or RNA sensors, including VSV and Sendai virus (SeV) for RIG-I, EMCV for Melanoma Differentiation-Associated protein 5 (MDA5), and HSV-1 for Cyclic GMP-AMP synthase (cGAS) as shown in the diagram (**Figure 4F, *right***). We found that TRIM14 deficiency in THP-1 cells markedly dampened p-IRF3, IFN-β secretion, and increased virus replication after infection with either RNA viruses (VSV and SeV), or DNA virus (HSV-1) (**Figures 4F-H**). By contrast, EMCV-induced p-IRF3 was only slightly reduced, but no changes in IFN-β expression and viral replication, suggesting a dominant role of TRIM14 in the RIG-I pathway. Effect of TRIM14 on cGAS was similar to our recent report, showing that TRIM14 regulates cGAS stability [17]. As TRIM14 enhances activation of RIG-I signaling, we next sought to determine the

molecular mechanisms of how TRIM14 regulates RIG-I signaling. We found that TRIM14 significantly promoted RIG-I- and MAVS-, but not TBK1- or IRF3-, induced IFN-β signaling activation and IFN-β expression, suggesting TRIM14 promotes IFN-I signaling probably through targeting RIG-I and MAVS (**Figures 4I and 4J**). Indeed, co-IP experiments revealed that TRIM14 interacted with RIG-I after stimulation but could interact with MAVS even without stimulation (**Figure 4K**). There was no interaction of TRIM14 with MDA5 or laboratory of genetics and physiology-2 (LGP2) observed (**Figure 4K**), indicating that TRIM14 promotes RIG-I signaling by targeting RIG-I after stimulation.

Identification of a WHIP-TRIM14-PPP6C complex that positively regulates RIG-I signaling

Next, we sought out to identify additional TRIM14 interacting proteins that may participate in RIG-I signaling activation. Proteomic mapping methods engineered ascorbic acid peroxidase (APEX) proximity biotin-labelling followed by mass spectrometry and the yeast two-hybrid screening system were utilized. We identified Werner helicase-interacting protein 1 (WHIP) and protein phosphatase 6 catalytic subunit (PPP6C) as potential interactors of TRIM14 (**Figure 5A-E**). Of note, PPP6C was also one of our candidates that interacted with TRIM14 in a distinct screening system by using APEX2 biotin-labeling [125] mentioned in our previous study [17]. To demonstrate their interactions in physiological conditions, we performed immunoprecipitation in human monocyte THP-1 cells using a TRIM14 antibody and showed endogenous interactions among TRIM14, WHIP, and PPP6C, even without VSV infection (**Figures 5F**), suggesting pre-existence of this complex. Confocal imaging analysis further showed that TRIM14 colocalized with WHIP and PPP6C as a complex in the cytosol forming punctate structures before stimulation, in addition to the nuclear localization of WHIP as expected [126] (**Figure 5G**). To further support the assembly of a WHIP-TRIM14-PPP6C complex, we performed size-exclusion chromatography

co-elution experiments and showed that WHIP, TRIM14, and PPP6C were co-eluted in a complex with a high molecular mass of approximately 650 kDa (**Figure 5H, Mock**). Upon VSV infection, WHIP, TRIM14, and PPP6C were co-eluted in even higher molecular weight fractions (**Figure 5H, VSV vs. Mock**), suggesting that viral infection promotes the assembly of WHIP-TRIM14-PPP6C with additional molecules, such as RIG-I and/or MAVS. Indeed, we readily detected RIG-I in the same fractions containing WHIP-TRIM14-PPP6C complexes (**Figure 5H, VSV vs. Mock**). By contrast, *TRIM14* deficiency completely disrupted the entire complex, suggesting a crucial role of TRIM14 in the assembly of the WHIP-TRIM14-PPP6C complex (**Figure 5H, *TRIM14* KO vs. WT mock**).

To confirm the stimulatory roles of WHIP and PPP6C in IFN-I signaling, we generated *WHIP* KO and *PPP6C* KO cells by the CRISPR/Cas9 system. We showed a dramatic reduction in ISRE-Luciferase activity stimulated by poly(I:C)-LMW and VSV, as well as VSV-induced phosphorylation of IRF3 in *WHIP* KO and *PPP6C* KO 293T cells (**Figures 5I-K**). As a result, the IFN-β production was significantly decreased in *WHIP* KO and *PPP6C* KO THP-1 cells after VSV infection (**Figure 5L**). To further map the TRIM14 domains responsible for the interactions with WHIP and PPP6C, we performed immunoprecipitation using FLAG-tagged full-length (FL) and truncated TRIM14 (NT, 1-265 aa; CT, 266-442 aa) proteins to detect HA-WHIP and HA-PPP6C. We found that WHIP interacted with the N-terminal domain of TRIM14, whereas PPP6C associated with the C-terminal domain of TRIM14 and weakly interacted with the N-terminal domain of TRIM14 (**Figure 5M**). Thus, our data uncovered a previously unrecognized role of TRIM14 in the assembly of a positive regulatory signalosome, comprising WHIP and PPP6C in the modulation of RIG-I-mediated IFN-I signaling.

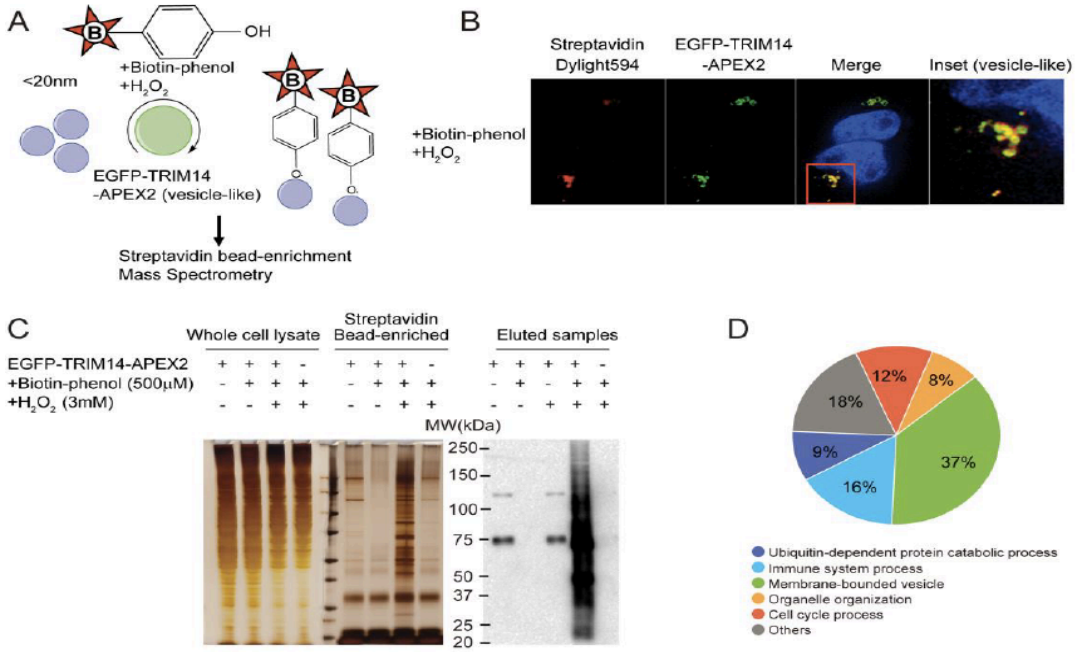

Figure 5. TRIM14 forms a complex with WHIP and PPP6C that promotes RIG-I signaling. (A) Schematic depiction of proteomic mapping of TRIM14 interacting candidates through APEX2-mediated biotin labeling. APEX2 fused to TRIM14 enables biotin labeling on proteins surrounded < 20 nm from TRIM14 in the presence of H2O2 and Biotin-phenol. Biotinylated proteins were then affinity-enriched with streptavidin beads. Eluted products were further analyzed by mass spectrometry. (B) Fluorescence imaging of co-localization of biotinylated candidates stained with a Dylight594-conjugated anti-Streptavidin antibody with EGFP-TRIM14-APEX2 forming vesicle-like structure in HEK293 cells as illustrated in panel (A). (C) Silver staining and immunoblotting of biotinylated binding candidates surrounding TRIM14. Shown on the SDS-PAGE were samples before (lanes 1-4) and after (lanes 5-8) streptavidin bead-enrichment, as well as the eluted samples immunoblotted by HRP-conjugated anti-streptavidin antibody (Streptavidin-HRP, lanes 9-13). (D) Classification of candidates emerged from proteomic mapping. (E) Yeast two-hybrid (Y2H) screening identified WHIP and PPP6C as interactors of TRIM14. (F) Co-IP and IB analysis of THP-1 cells infected with VSV for 8 h. (G) Confocal microscopy analysis of WHIP (blue), TRIM14 (green), and PPP6C (red) in 293T cells. Below is an enlargement of the area outlined on the top. Quantification of WHIP/TRIM14, WHIP/PPP6C, or TRIM14/PPP6C correlation (C, *right*). (H) Extracts of THP-1 cells mock treated or infected with VSV (MOI=1) for 12 h were fractionated on a size-exclusion column. The collected fractions (0.5 ml) were used for IB analysis with specific antibodies. The size was determined by the elution of calibration proteins with known molecular masses (kDa). (I and J) IB analysis of WT and *WHIP* KO (E) or *PPP6C* KO (F) THP-1 cells infected with VSV for 8 h. (K) ISRE promoter luciferase assay of *TRIM14*, *WHIP,* or *PPP6C* KO 293T cells stimulated with poly(I:C)-LMW or VSV. (L) ELISA of IFN-β production in WT, *TRIM14* KO, *WHIP* KO, or *PPP6C* KO THP-1 cells infected with VSV for 12 h. (M) Co-IP and IB analysis of 293T cells transfected with full length (FL), N-terminus, or C-terminus FLAG-TRIM14 together with HA-WHIP or PPP6C. Data in (K) and (L) are expressed as means ± SD of three independent experiments. *p<0.05, **p<0.01, versus controls.

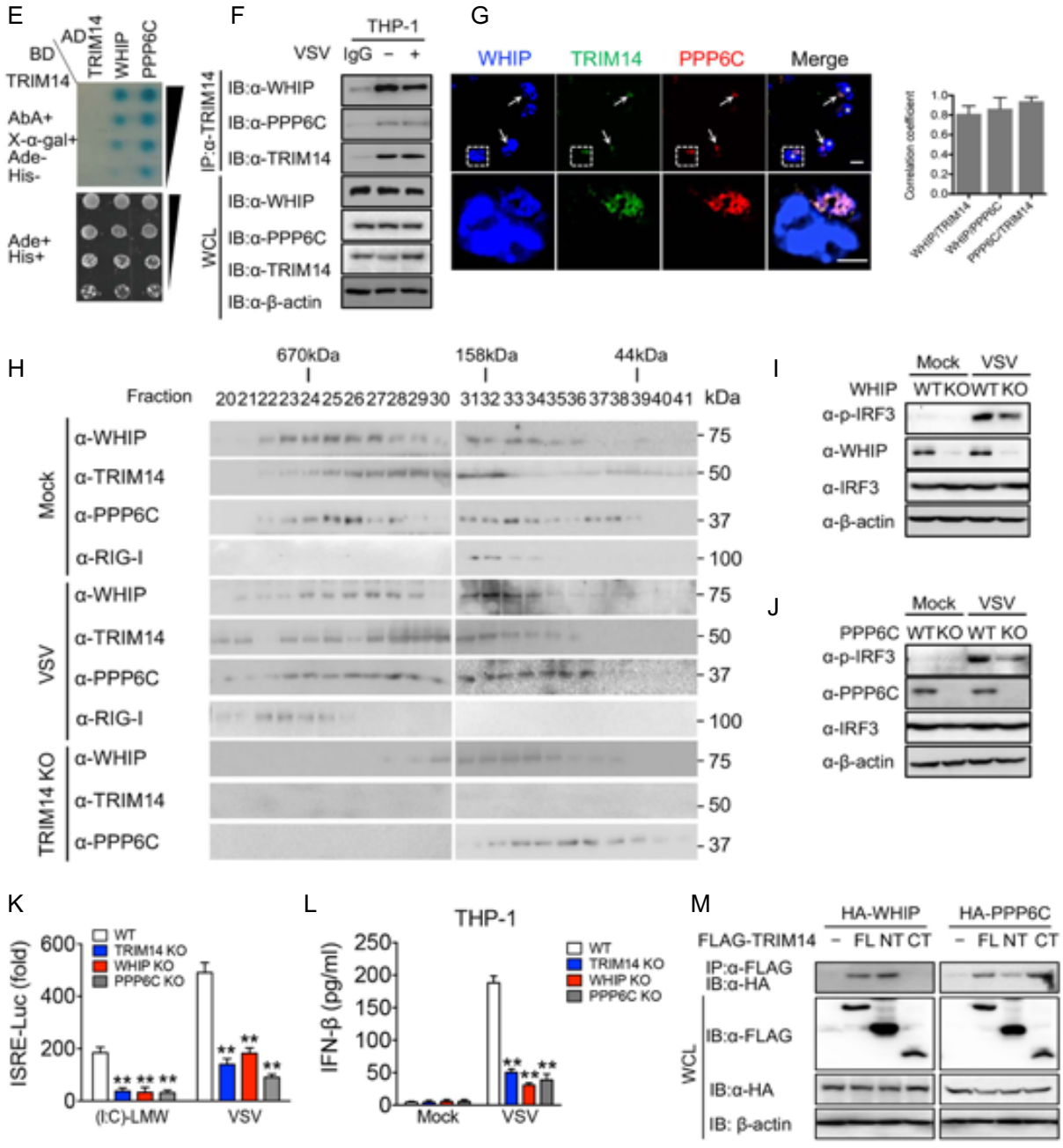

Figure 5. Continued.

WHIP bridges RIG-I with the WHIP-TRIM14-PPP6C complex after stimulation

Since we demonstrated that TRIM14 formed a complex with WHIP and PPP6C, we investigated how the WHIP-TRIM14-PPP6C complex interacts with RIG-I after stimulation. Co-IP experiments confirmed that WHIP and PPP6C could also interact with RIG-I only after VSV infection, while they interacted with MAVS before and after VSV infection (**Figures 6A**). By contrast, there were no interactions of WHIP and PPP6C with MDA5 or LPG2. Consistently, confocal microscopy analysis further showed the colocalization of TRIM14, WHIP, and PPP6C with RIG-I on mitochondria after poly(I:C)-LMW stimulation (**Figures 6B**). These results, along with data from Figures 1K and 2, further support our conclusion that the WHIP-TRIM14-PPP6C complex inducibly interacts with RIG-I, but constitutively interacted with MAVS.

To further validate the essential component of the TRIM14 complex that mediates the interaction with RIG-I after stimulation, we investigated the direct interaction of the WHIP-PPP6C-TRIM14 complex with RIG-I in the *WHIP*, *TRIM14*, and *PPP6C* KO 293T cells. We found that WHIP deficiency blocked the interactions of RIG-I with TRIM14 and PPP6C (**Figure 6C**). In addition, *TRIM14* KO reduced the interaction of RIG-I with WHIP and blocked the interaction of RIG-I with PPP6C (**Figure 6C**). By contrast, PPP6C deficiency did not affect the interactions of RIG-I with WHIP or TRIM14 (**Figure 6C**). These results suggest that WHIP is the most crucial factor that mediates the interaction of RIG-I with TRM14 and PPP6C, while PPP6C is not required for their interaction of RIG-I with WHIP and TRIM14. WHIP ablation in 293T cells substantially abolished the poly(I:C)-LMW induced association of RIG-I with TRIM14 punctate structures as well as RIG-I mitochondrial localization **(Figure 6D).** To determine the critical domains of WHIP that mediate interactions with RIG-I, TRIM14, and PPP6C after stimulation, we performed co-IP experiments and found that the N-terminal domain of WHIP

interacted with RIG-I, while the C-terminal domain is important for the interaction with PPP6C and TRIM14 (**Figure 6E**). These results suggest that WHIP plays a critical role in bridging the WHIP-TRIM14-PPP6C complex with RIG-I by interacting with RIG-I using its N-terminal domain after stimulation while keeping its interactions with TRIM14 and PPP6C through its C-terminal domain.

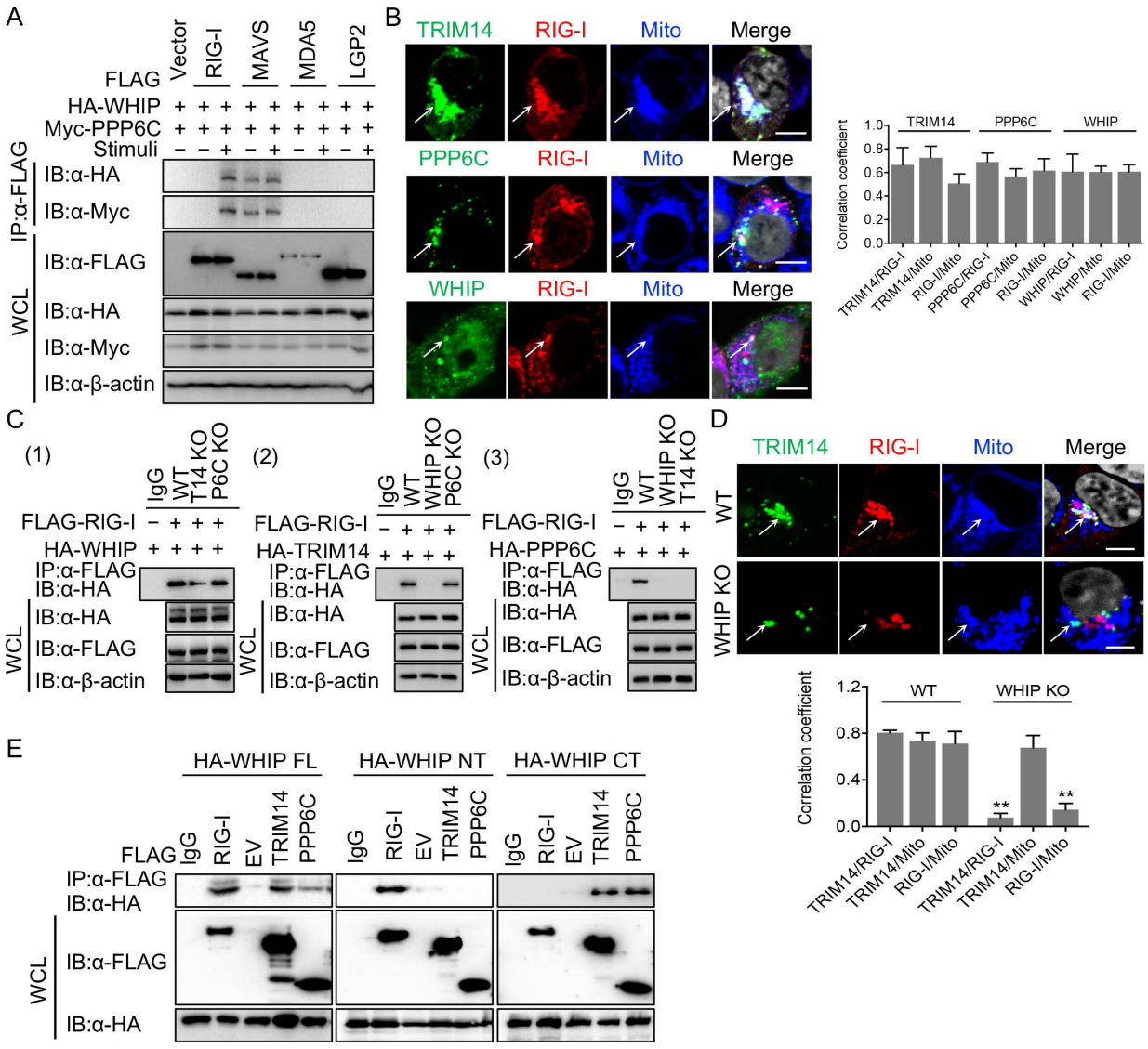

Figure 6. WHIP mediates RIG-I interaction with TRIM14 and PPP6C after stimulation. (A) Co-IP and IB analysis of 293T cells transfected with plasmids for WHIP and PPP6C together with FLAG-RIG-I, MAVS, MDA5, or LGP2, followed by stimulation (VSV for RIG-I and MAVS; EMCV for MDA5 and LGP2) for 8 h. (B) Confocal microscopy of 293T cells stimulated with poly(I:C)-LMW for 8 h. Mitochondria were stained using mitotracker. The white arrow indicates colocalization. Scale bar: 10 μm. Quantification of TRIM14/RIG-I/Mito, PPP6C/RIG-I/Mito, or WHIP/RIG-I/Mito correlation (B, *right*). (C) The interaction of WHIP-TRIM14-PPP6C mitochondrial complex components with RIG-I after poly(I:C)-LMW stimulation for 8 h. Interaction of FLAG-RIG-I with HA-WHIP in WT, *TRIM14* KO, or *PPP6C* KO 293T cells (C, *1*). Interaction of FLAG-RIG-I with HA-TRIM14 in WT, *WHIP* KO, or *PPP6C* KO 293T cells (C, *2*). Interaction of FLAG-RIG-I and HA-PPP6C in WT, *WHIP* KO, or *TRIM14* KO 293T cells (C, *3*). Control was IP with IgG. (D) Confocal analysis of WT and *WHIP* KO 293T cells stimulated with poly(I:C)-LMW for 6 h. Scale bar: 10 μm. Correlation coefficient analyses of TRIM14/RIG-I, TRIM14/Mito, or RIG-I/Mito (D, *below*). (E) Co-IP and IB analysis of 293T cells transfected with full length (FL), N-terminus (1-245 aa), or C-terminus (246-665 aa) HA-WHIP together with empty vector, FLAG-RIG-I, TRIM14, or PPP6C. Data in (B) and (D) are expressed as means ± SD of three independent experiments. *$p<0.05$, **$p<0.01$, versus controls.

WHIP is required for TRIM14-mediated enhancing effect on RIG-I Signaling and binds to polyUb chains on RIG-I lys164

To further define the detailed mechanisms and physiological function of WHIP, we used WT and *WHIP* KO 293T cells with or without ectopic expression of TRM14 followed by poly(I:C)-LMW stimulation or VSV infection. We found that ectopic expression TRIM14 enhanced ISRE-Luc activities after poly(I:C)-LMW stimulation or VSV infection in WT cells but failed to do so in *WHIP* KO 293T cells (**Figure 7A**). Similar results were obtained for IRF3 phosphorylation using WT and *WHIP* KO cells (**Figure 7B**). These data suggest that WHIP is absolutely required for TRIM14-mediated enhancing effects on RIG-I-mediated signaling.

A conserved UBD harbored in the N terminus of WHIP has been reported to be capable of binding to K63 polyUb chains [118]. We hypothesized that the viral dsRNA induced opening-conformation of RIG-I and subsequently the K63 ubiquitination of RIG-I might provide the access for WHIP to interact with RIG-I through its ubiquitin-binding domain [127, 128]. We, therefore, generated a D37A mutant of WHIP, whose ubiquitin-chain-binding ability was greatly impaired

[118] and used for co-IP experiments. Although WT WHIP bound to RIG-I, as we expected, we failed to detect the interaction of the WHIP D37A mutant with RIG-I after poly(I:C)-LMW stimulation (**Figure 7C**). Consistent with this observation, the WHIP D37A mutant diminished TRIM14-stimulated ISRE-Luc activity after poly(I:C)-LMW stimulation (**Figure 7D**). These results indicate that the UBD in WHIP is required for the interaction between WHIP and RIG-I and its subsequent function in IFN-I signaling.

We next tested whether the blockade of the K63 polyUb chains on RIG-I could impair the binding of WHIP to RIG-I. We generated RIG-I mutants K99R, K164R, K169R, K172R, and K788R (in which the Lys residue was substituted with Arg) to abolish the attachment of polyUb chains on RIG-I. We showed that K164R mutant inhibited WHIP- and TRIM14-stimulated ISRE-Luc activity triggered by poly(I:C)-LMW, compared to other known important lysine residues (**Figure 7E**), suggesting that WHIP binds to the polyUb chains of RIG-I 2CARD domain at the K164 site. Furthermore, we showed that WHIP colocalized with RIG-I-2CARD (**Figure 7F**). Consistently, we found that while WHIP could efficiently bind to WT and RIG-I K172R mutant after VSV infection, the interaction of WHIP with RIG-I K164R mutant was completely abolished (**Figure 7G**). Further experiments using a WHIP antibody showed that pull-down of ubiquitinated RIG-I after VSV infection contained RIG-I with a higher molecular weight, suggesting that WHIP binds to ubiquitinated RIG-I through polyUb chains (**Figure 7H**).

Since E3 ligase TRIM4 has been shown to be responsible for the K63 ubiquitination of RIG-I at the K164 site [50], we next tested whether depletion of TRIM4 could abolish the binding of WHIP to RIG-I. We generated TRIM4 depleted 293T cells by *TRIM4* shRNA and showed that *TRIM4* depletion markedly reduced the binding of WHIP to RIG-I, as well as the WHIP-stimulated ISRE-Luc activity after stimulation (**Figures 7I and 7J**). These data suggest that the binding of

WHIP to the K63 polyUb chains at the K164 site of RIG-I is a key event to mediate the WHIP-TRIM14-PPP6C complex-induced activation of RIG-I IFN signaling.

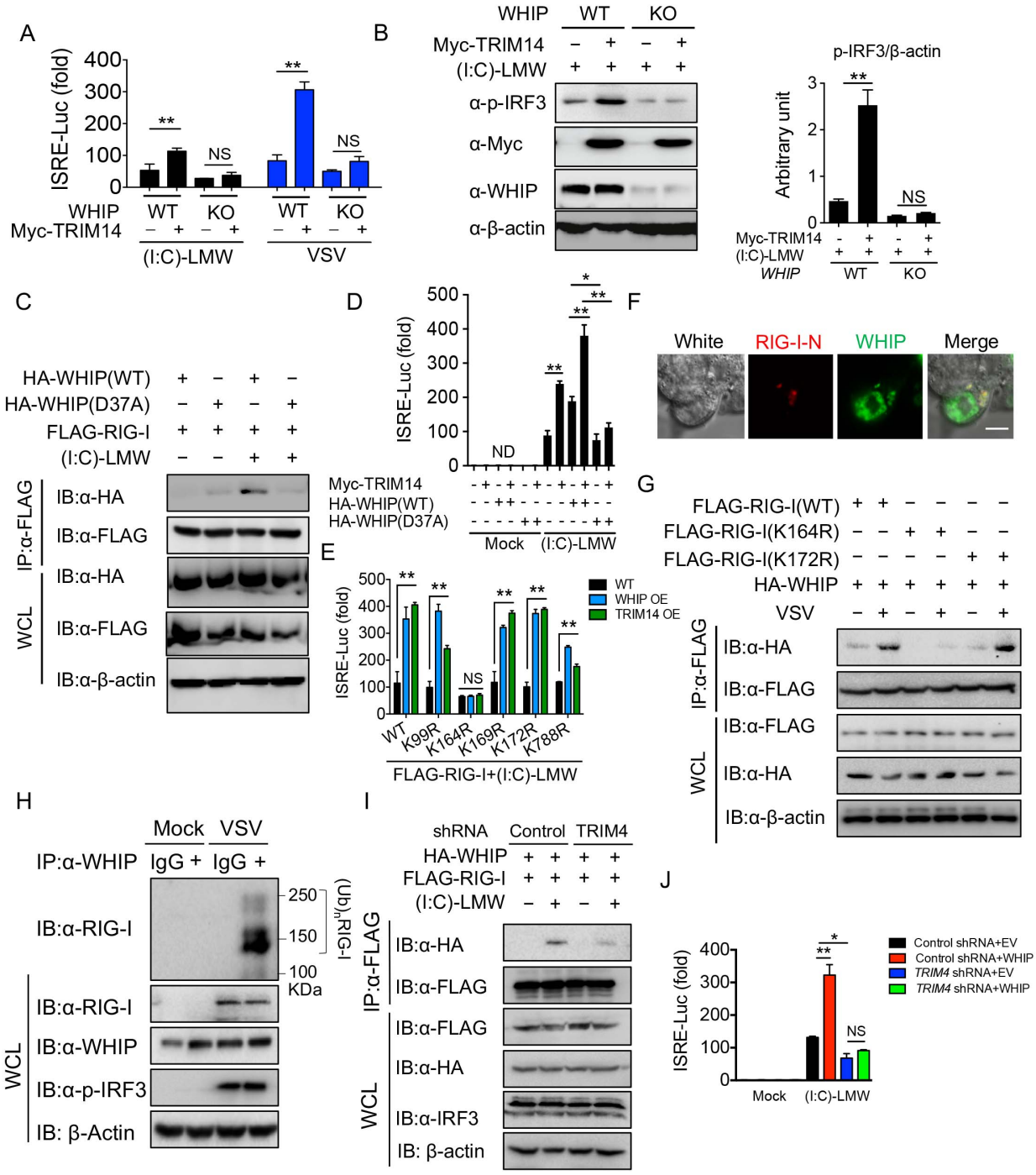

Figure 7. WHIP binds to polyUb chains on RIG-I lys164. (A) ISRE promoter luciferase activity of WT or *WHIP* KO 293T cells transfected with empty vector or Myc-TRIM14 followed by poly(I:C)-LMW (black bars) or VSV (blue bars) stimulation. (B) IB analysis of WT and *WHIP* KO 293T cells transfected with empty vector or Myc-TRIM14, followed by poly(I:C)-LMW stimulation. Quantitative comparison of the p-IRF3 level was analyzed by densitometric scanning of blots normalized to β-actin. (C) Co-IP and immunoblot analysis of 293T cells transfected with FLAG-RIG-I together with WT or D37A mutant HA-WHIP, followed by poly(I:C)-LMW stimulation. (D) ISRE reporter luciferase assay of WT and *WHIP* KO 293T cells reconstituted with empty vector alone, or Myc-TRIM14 alone or combined with HA-WHIP WT or HA-WHIP D37A, followed by poly(I:C)-LMW stimulation. ND, not detected. (E) ISRE reporter luciferase assay of 293T cells transfected with FLAG-RIG-I (WT, K99R, K164R, K169R, K172R, K788R) along with empty vector, HA-WHIP, or Myc-TRIM14, followed by poly(I:C)-LMW treatment. (F) Confocal microscopy 293T cells transfected with GFP-WHIP and mcherry-RIG-I-2CARD (RIG-I-N) without stimulation. White, white field. (G) Co-IP and IB analysis of 293T transfected with WT FLAG-RIG-I or various RIG-I mutants along with HA-WHIP followed by VSV infection. (H) Co-IP and IB analysis of 293T cells infected with VSV for 12 h. (I) Co-IP and IB analysis of WT or *TRIM4* depleted 293T cells were transfected with FLAG-RIG-I and HA-WHIP followed by poly(I:C)-LMW stimulation for 10 h. (J) ISRE reporter luciferase assay of WT or *TRIM4* depleted 293T cells transfected with empty vector or HA-WHIP, followed by poly(I:C)-LMW stimulation. Data in (A), (B), (D-E), and (J) are expressed as means ± SD of three independent experiments. *$p<0.05$, **$p<0.01$, NS: not significant, versus controls.

WHIP stabilizes RIG-I-dsRNA interaction and promotes RIG-I K63 ubiquitination

Studies of ATP-dependent viral RNA recognition by RLR and oligomerization of RLR on viral RNA reveal the essential role of the ATPase core domain harbored in RLR [129]. We asked whether the ATPase activity of WHIP is required for RIG-I signaling. We reasoned that ATPase activity of WHIP might act as a feedback to stabilize RIG-I-dsRNA interaction, promote RIG-I K63 ubiquitination, and enhance the WHIP-RIG-I interaction. To test our predictions, we generated a WHIP ATPase-dead mutant (T294A), in which Thr294, a conserved residue in the nucleotide binding motif, was substituted with Ala [130]. Ectopic expression of WT WHIP in *WHIP* KO 293T cells conferred ISRE-promoter activity in response to poly(I:C)-LMW stimulation, but the ISRE-Luc activity was markedly inhibited when WHIP-T294A or WHIP-D37A mutants were used (**Figure 8A**), suggesting that the ATPase activity of WHIP is required for regulating RIG-I-mediated signaling.

To determine the role of ATPase activity of WHIP in RIG-I-dsRNA interaction, we performed a pull-down experiment by incubating NeutrAvadin-beads, biotin-labeled poly(I:C)-LMW or biotin-only along with cell lysates of 293T cells co-transfected with FLAG-tagged RIG-I and increasing amounts of HA-WHIP WT or HA-WHIP T294A mutant. We found that addition of HA-WHIP-WT, but not the HA-WHIP T294A mutant, enhanced binding of FLAG-RIG-I to biotin-(I:C)-LMW (**Figure 8B**). We further showed that that deletion of WHIP potently inhibited K63 ubiquitination of RIG-I after VSV stimulation (**Figure 8C**). To compare the WHIP binding (UBD) and WHIP ATPase activity in RIG-I K63 ubiquitination, we reconstituted *WHIP* KO cells with WHIP WT, D37A, and T294A mutants followed by VSV infection and found that whereas WT WHIP restored the K63 ubiquitination, T294A and D37A failed to do so (**Figure 8D**). These results suggest that both ubiquitin-binding and the ATPase activity of WHIP are required for RIG-I K63 ubiquitination. Furthermore, we found that loss of ATPase activity (T294A) markedly reduced WHIP-RIG-I interaction, whereas loss of ubiquitin-binding ability (D37A) completely blocked WHIP-RIG-I interaction (**Figure 8E**), suggesting an essential role of ubiquitin-binding and a supportive role of ATPase activity in the WHIP-RIG-I interaction. Thus, our data demonstrate a role of ATPase activity of WHIP in the stabilization of RIG-I-dsRNA complex and RIG-I K63 poly-ubiquitination.

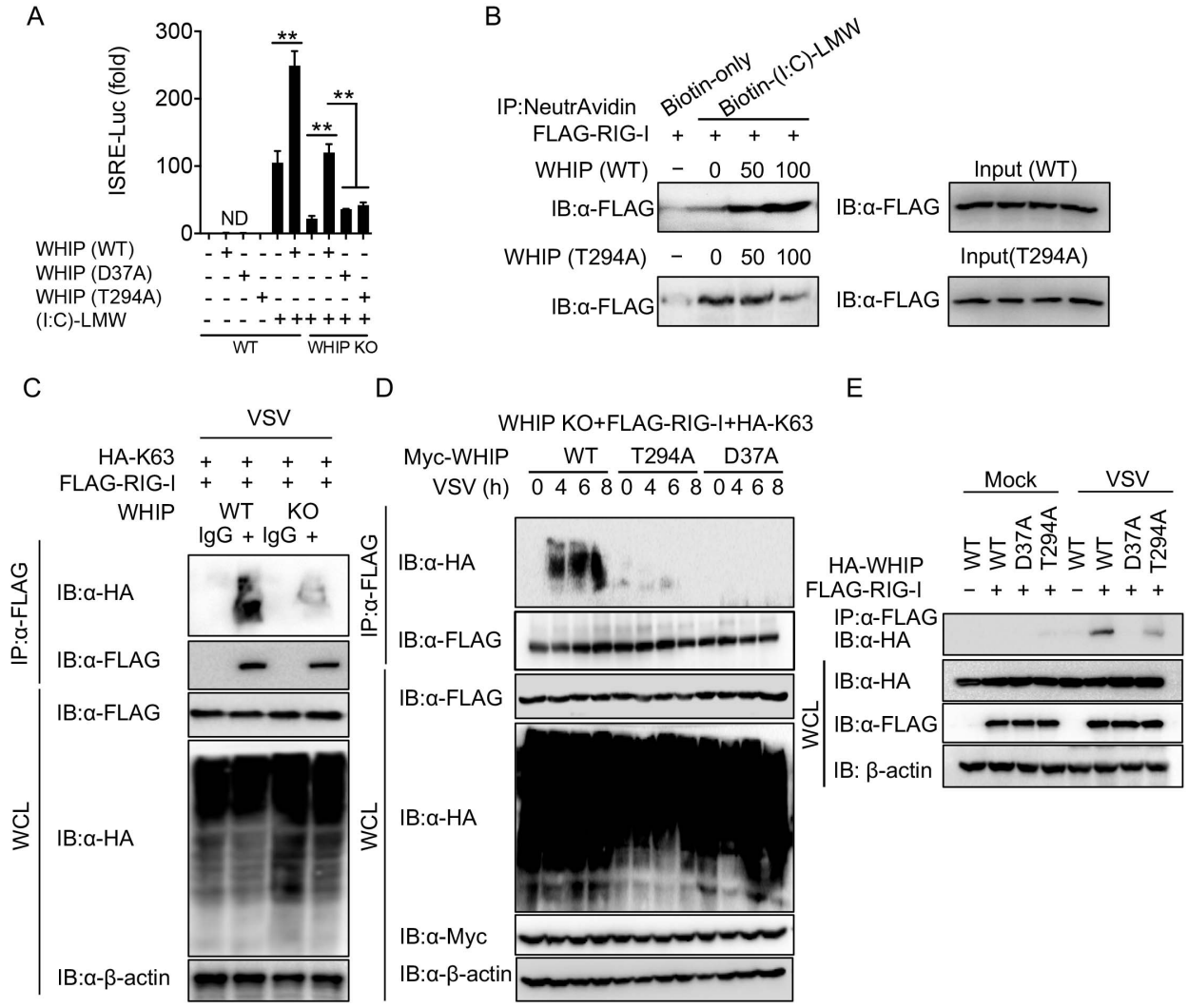

Figure 8. WHIP stabilizes RIG-I-dsRNA and promotes RIG-I K63 ubiquitination. (A) ISRE promoter luciferase assay of WT or *WHIP* KO 293T cells transfected with empty vector, HA-WHIP WT, HA-WHIP D37A or HA-WHIP T294A, followed by poly(I:C)-LMW stimulation. ND, not detected. (B) 293T transfected with FLAG-RIG-I along with the indicated amount (ng) of HA-WHIP (WT) or HA-WHIP (T294A) plasmids. Cell lysates were then incubated with biotin-only or biotinylated-poly(I:C)-LMW for 4 h. Pull-down experiments were performed with NeutrAvadin beads, followed by immunoblot analysis using anti-FLAG antibody. (C) Co-IP and IB analysis of WT or *WHIP* KO 293T cells transfected with FLAG-RIG-I and HA-K63 ubiquitin plasmids, followed by VSV infection for 10 h. (D) Co-IP and IB analysis of *WHIP* KO 293T cells transfected with FLAG-RIG-I and HA-K63 ubiquitin plasmids along with WT, D37A, or T294A WHIP followed by VSV infection for the indicated time points. (E) Co-IP and IB analysis of 293T cells transfected with WT, D37A, or T294A HA-WHIP along with FLAG-RIG-I, followed by VSV infection for 10 h. Data in (A) is expressed as means ± SD of three independent experiments (*p<0.05, **p<0.01, NS: not significant, versus controls).

PPP6C is responsible for RIG-I dephosphorylation

Next, we investigated the potential role of the PPP6C in IFN-I signaling. Since PPP6C is a phosphatase, we reasoned that PPP6C might be involved in the dephosphorylation of RIG-I, an essential step that triggers the RIG-I-mediated signaling activation. To test this hypothesis, we incubated FLAG-RIG-I overexpressed 293T cell lysate with an increasing amount of purified PPP6C recombinant protein and monitored the RIG-I phosphorylation with and without VSV infection. As expected, we observed a decrease of phosphorylated RIG-I after infection, and PPP6C treatment further abolished the phosphorylation of RIG-I on both the serine 8 (S8) and threonine 170 (T170) sites in a dose-dependent manner (**Figure 9A**). Consistently, when *PPP6C* KO 293T cells were infected with VSV, the RIG-I phosphorylation at both the S8 and T170 sites were dramatically increased, which was accompanied with diminished p-IRF3 activity (**Figure 9B**), and thus suggesting that PPP6C plays a positive regulator function in antiviral signaling through the dephosphorylation of RIG-I. Mutations in the PPP6C catalytic subunit have been reported as drivers for the development of melanoma by compromising the catalytic activity of PPP6C [131]. We generated the mutants R85A, K132N, P186S, R264C, and H114Y (with increased proteasome-mediated turnover) and tested their expressions and functions in the RIG-I activation. As expected, H114Y showed reduced expression compared to the other catalytic mutations (**Figure 9C**) due to its self-degrading effect [131]. Mutations in the catalytic subunit abolished the function of PPP6C as revealed by ISRE-Luc activity (**Figure 9D**). Moreover, the phosphatase catalytic subunit has been shown to form a complex with regulatory subunits to determine its substrate specificity or subcellular location such as PP1 and its regulatory subunit GADD34 [132]. We tested the potential functions of the PPP6 regulatory subunits in RIG-I dephosphorylation and RIG-I signaling, including PPP6R1, PPP6R2, and PPP6R3 [133]. We

found that only PPP6C, but not the regulatory subunits, could dephosphorylate RIG-I and promote poly(I:C)-LMW induced ISRE-Luc activity (**Figures 9E and 9F**). Since PPP6C functions in RIG-I dephosphorylation at S8 and T170 sites, we tested whether blocking the phosphorylation sites of RIG-I could abolish the function of PPP6C. By generating serine 8 to alanine (S8A) and threonine 170 to alanine (T170A) mutants, we showed that while RIG-I S8A and T170A still increased RIG-I signaling activation, as previously reported [7, 134], PPP6C no longer further enhanced the ISRE-Luc activity compared with RIG-I WT control (**Figure 9G**). These data suggest that PPP6C acts as a positive feedback regulator by dephosphorylating RIG-I. To test whether the effect of PPP6C on RIG-I relies on the assembly of the TRIM14-WHIP signalosome complex, we overexpressed PPP6C in WT, *TRIM14* KO, and *WHIP* KO 293T cells. PPP6C failed to stimulate ISRE-Luc activity when TRIM14 or WHIP was ablated (**Figure 9H**), indicating that the intact signalosome of TRIM14-WHIP-PPP6C is indispensable for PPP6C to perform its positive regulatory function.

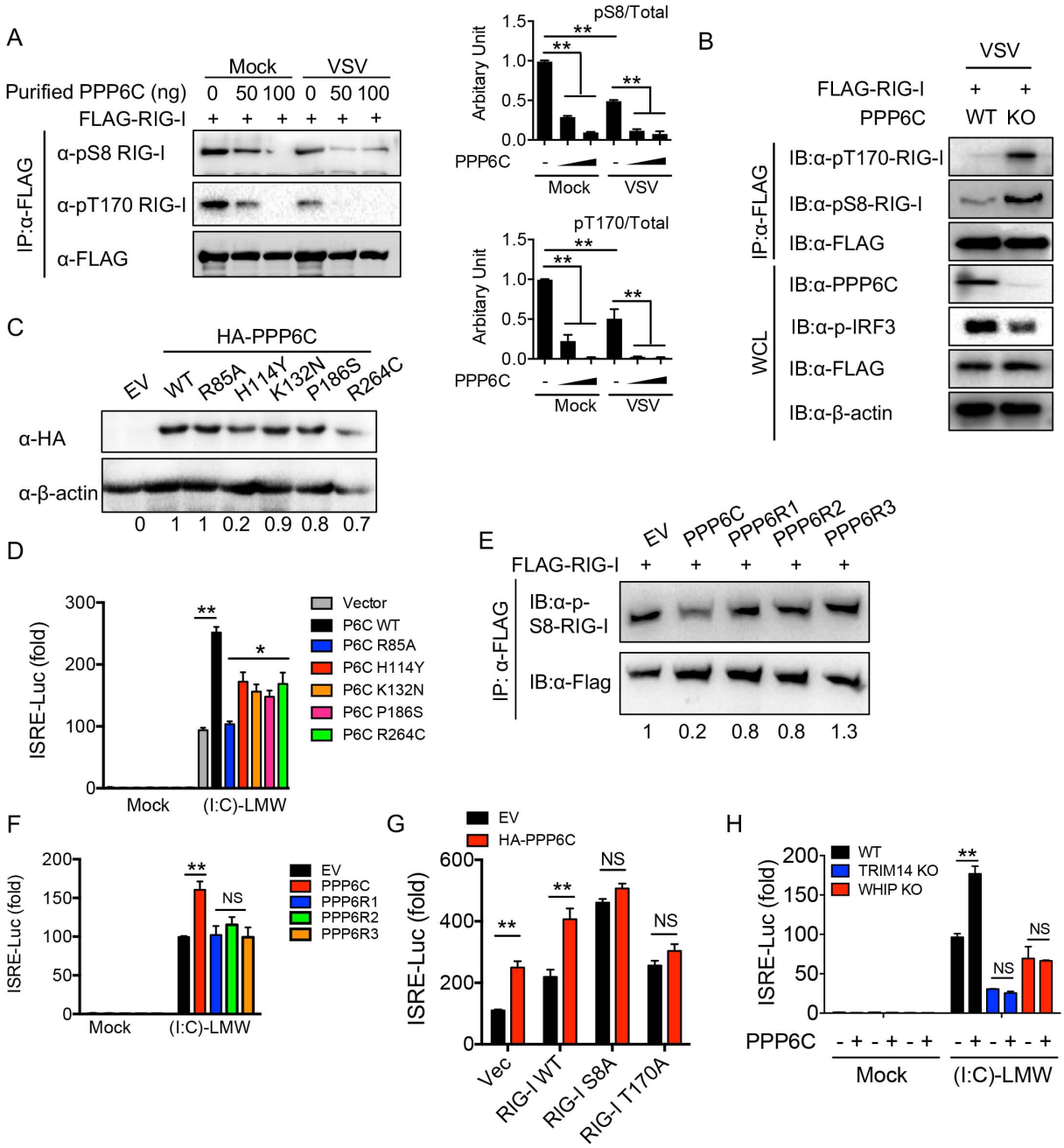
A
Mock
VSV
Purified PPP6C (ng) 0 50 100 0 50 100
FLAG-RIG-I + + + + + +
IP:α-FLAG
α-pS8 RIG-I
α-pT170 RIG-I
α-FLAG
pS8/Total
Arbitary Unit
PPP6C
Mock
VSV
pT170/Total
B
VSV
FLAG-RIG-I + +
PPP6C WT KO
IP:α-FLAG
IB:α-pT170-RIG-I
IB:α-pS8-RIG-I
IB:α-FLAG
WCL
IB:α-PPP6C
IB:α-p-IRF3
IB:α-FLAG
IB:α-β-actin
C
HA-PPP6C
EV WT R85A H114Y K132N P186S R264C
α-HA
α-β-actin
0 1 1 0.2 0.9 0.8 0.7
D
ISRE-Luc (fold)
Vector
P6C WT
P6C R85A
P6C H114Y
P6C K132N
P6C P186S
P6C R264C
Mock
(I:C)-LMW
E
EV PPP6C PPP6R1 PPP6R2 PPP6R3
FLAG-RIG-I + + + + +
IP: α-FLAG
IB:α-p-S8-RIG-I
IB:α-Flag
1 0.2 0.8 0.8 1.3
F
ISRE-Luc (fold)
EV
PPP6C
PPP6R1
PPP6R2
PPP6R3
NS
Mock
(I:C)-LMW
G
EV
HA-PPP6C
ISRE-Luc (fold)
NS
Vec
RIG-I WT
RIG-I S8A
RIG-I T170A
H
WT
TRIM14 KO
WHIP KO
ISRE-Luc (fold)
NS
PPP6C - + - + - + - + - + - +
Mock
(I:C)-LMW

Figure 9. PPP6C is essential for RIG-I dephosphorylation. (A) Cell lysates from mock treated or VSV infected 293T cells expressing FLAG-RIG-I were incubated with purified recombinant HA-tagged PPP6C protein (0, 50, 100 ng) for 2 h followed by co-IP with FLAG-beads. Elutes from beads were subjected to immunoblot analysis with the indicated antibodies. Quantitative comparison of p-S8-RIG-I and p-T170-RIG-I level were analyzed by densitometric scanning of blots and normalized to total FLAG-RIG-I (*right*). (B) Co-IP and IB analysis of WT or *PPP6C* KO 293T cells transfected with FLAG-RIG-I followed by VSV infection. (C and D) Immunoblot analysis (C) and ISRE reporter luciferase activity (D) 293T cells transfected with HA-PPP6C WT or mutants, followed by poly(I:C)-LMW stimulation. (E and F) Co-IP and IB analysis (E) and ISRE luciferase reporter activity (F) of 293T cells transfected with empty vector, PPP6C, PPP6R1, PPP6R2 or PPP6R3, followed by VSV infection. (G) ISRE luciferase reporter assay of 293T cells transfected with empty vector, FLAG-RIG-I WT, S8A, or T170A mutants along with empty vector or HA-PPP6C. (H) ISRE luciferase reporter assay of WT, *TRIM14* KO, or *WHIP* KO 293T cells transfected with empty vector or the HA-PPP6C, followed by poly(I:C)-LMW stimulation. Data in (A), (D) and (F-H) are expressed as means ± SD of three independent experiments. *$p<0.05$, **$p<0.01$, NS: not significant, versus controls.

TRIM14-MAVS interaction is essential for mitochondria-association of WHIP-TRIM14-PPP6C complex

Since we had investigated the interaction and molecular mechanisms of the WHIP-TRIM14-PPP6C complex and RIG-I in an inducible manner, we next examined the endogenous interactions between MAVS and the WHIP-TRIM14-PPP6C complex in THP-1 cells. We observed a stable association of MAVS with these proteins before and after VSV infection (**Figure 10A**), suggesting that the MAVS platform might be crucial for the cellular localization of the WHIP-TRIM14-PPP6C complex. Consistent with these results, we observed, by confocal microscopy analysis, the colocalization of WHIP, TRIM14, and PPP6C with MAVS (**Figure 10B**). To understand how the TRIM14 complex interacts with MAVS, we studied the interactions of each component in the TRIM14 complex with MAVS using various KO cell lines. We found that *TRIM14* KO abolished the interactions of MAVS with WHIP and PPP6C (**Figure 10C**), suggesting that TRIM14 is a key regulator of their interactions. Consistently, fluorescent confocal microscopy analysis revealed that co-localization of TRIM14, PPP6C, and WHIP with MAVS was

impaired in *TRIM14* KO cells, compared to WT (**Figures 10D**). We hypothesized that TRIM14-MAVS interaction might provide a mitochondrial docking platform for WHIP-TRIM14-PPP6C. To test this, we isolated mitochondrial and cytosol/nuclear fractions, and detected all three proteins in the isolated mitochondrial fraction, compared to the cytosol and nuclear-combined fraction (**Figure 10E**).

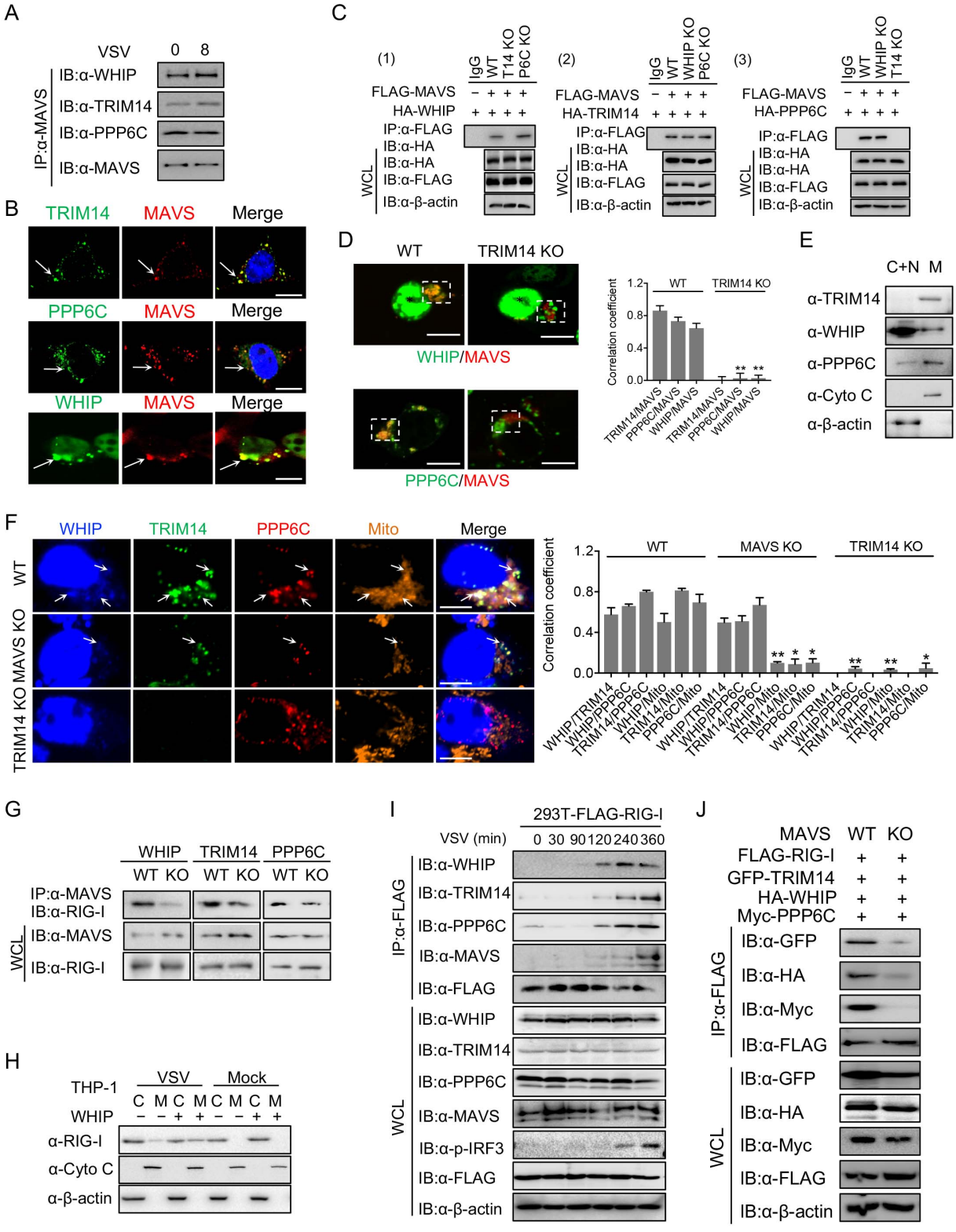
A
VSV 0 8
IP:α-MAVS
IB:α-WHIP
IB:α-TRIM14
IB:α-PPP6C
IB:α-MAVS
B
TRIM14 MAVS Merge
PPP6C MAVS Merge
WHIP MAVS Merge
C
(1)
IgG WT T14 KO P6C KO
FLAG-MAVS
HA-WHIP
IP:α-FLAG
WCL
IB:α-HA
IB:α-HA
IB:α-FLAG
IB:α-β-actin
(2)
IgG WT WHIP KO P6C KO
FLAG-MAVS
HA-TRIM14
IP:α-FLAG
IB:α-HA
IB:α-HA
IB:α-FLAG
IB:α-β-actin
(3)
IgG WT WHIP KO T14 KO
FLAG-MAVS
HA-PPP6C
IP:α-FLAG
IB:α-HA
IB:α-HA
IB:α-FLAG
IB:α-β-actin
D
WT TRIM14 KO
WHIP/MAVS
PPP6C/MAVS
Correlation coefficient
WT TRIM14 KO
TRIM14/MAVS
PPP6C/MAVS
WHIP/MAVS
E
C+N M
α-TRIM14
α-WHIP
α-PPP6C
α-Cyto C
α-β-actin
F
WHIP TRIM14 PPP6C Mito Merge
WT
MAVS KO
TRIM14 KO
Correlation coefficient
WT MAVS KO TRIM14 KO
WHIP/TRIM14
WHIP/PPP6C
TRIM14/PPP6C
WHIP/Mito
TRIM14/Mito
PPP6C/Mito
G
WHIP TRIM14 PPP6C
WT KO WT KO WT KO
IP:α-MAVS
IB:α-RIG-I
WCL
IB:α-MAVS
IB:α-RIG-I
H
THP-1
VSV Mock
C M C M C M C M
WHIP
α-RIG-I
α-Cyto C
α-β-actin
I
293T-FLAG-RIG-I
VSV (min)
0 30 90 120 240 360
IP:α-FLAG
IB:α-WHIP
IB:α-TRIM14
IB:α-PPP6C
IB:α-MAVS
IB:α-FLAG
WCL
IB:α-WHIP
IB:α-TRIM14
IB:α-PPP6C
IB:α-MAVS
IB:α-p-IRF3
IB:α-FLAG
IB:α-β-actin
J
MAVS WT KO
FLAG-RIG-I + +
GFP-TRIM14 + +
HA-WHIP + +
Myc-PPP6C + +
IP:α-FLAG
IB:α-GFP
IB:α-HA
IB:α-Myc
IB:α-FLAG
WCL
IB:α-GFP
IB:α-HA
IB:α-Myc
IB:α-FLAG
IB:α-β-actin

Figure 10. Mitochondrial WHIP-TRIM14-PPP6C complex bridges RIG-I and MAVS. (A) Co-IP and IB analysis of THP-1 cells infected with VSV for the indicated time points. (B) Confocal microscopy of 293T cells without stimulation. Scale bar: 10 μm. White arrows indicate colocalization. (C) The interactions of WHIP-TRIM14-PPP6C mitochondrial complex components with MAVS. Interaction of FLAG-MAVS with HA-WHIP in WT, *TRIM14* KO, or *PPP6C* KO 293T cells (C,1). Interaction of FLAG-MAVS with HA-TRIM14 in WT, *WHIP* KO or *PPP6C* KO 293T cells (C,*2*). Interaction of FLAG-MAVS and HA-PPP6C in WT, *WHIP* KO, or *TRIM14* KO 293T cells (C,*3*). IP with IgG was used as a control. (D) Confocal microscopy analysis of the colocalization of WHIP (green), TRIM14 (green), or PPP6C (green) with MAVS (red) in WT or *TRIM14* KO 293T cells. Scale bar: 10 μm. Colocalization was outlined by the box. Quantification of TRIM14/MAVS, PPP6C/MAVS, or WHIP/MAVS correlation in WT and *TRIM14* KO cells (D, *right*). (E) Cell fractions from THP-1 cells were isolated and subjected to immunoblot analysis with the indicated antibodies. Cytochrome C (Cyto C) marks mitochondria; β-actin was used as a cytosolic marker. C+N, cytosol and nucleus; M, mitochondria. (F) Confocal microscopy of WT, *MAVS* KO, or *TRIM14* KO 293T cells. White arrows indicate colocalization of WHIP, TRIM14, PPP6C with mitotracker. Scale bar: 10 μm. Quantification of WHIP/TRIM14, WHIP/PPP6C, TRIM14/PPP6C, WHIP/Mito, TRIM14/Mito, PPP6C/Mito correlation in WT, *MAVS* KO and *TRIM14* KO cells (F, *right*). (G) Co-IP and IB analysis of WT, *WHIP* KO, *TRIM14* KO, or *PPP6C* KO 293T cells infected with VSV for 8h. (H) IB analysis of RIG-I expression in cell fractions isolated from THP-1 cells with or without VSV infection for 8h. Lane 1-2, 5-6 empty vector; Lane 3-4, 7-8 overexpressing WHIP. Cytochrome C (Cyto C) marks mitochondria; β-actin was used as a cytosolic marker. C, cytosol; M, mitochondria. (I) Co-IP and IB analysis of 293T cells stably expressing FLAG-RIG-I infected with VSV for the indicated time points. (J) Co-IP and IB analysis of WT or *MAVS* KO 293T cells transfected with FLAG-RIG-I along with GFP-TRIM14, HA-WHIP, and Myc-PPP6C, followed by VSV infection for 8 h. Data in (D) and (F) are expressed as means ± SD of three independent experiments *$p<0.05$, **$p<0.01$, NS: not significant, versus controls.

Notably, TRIM14 was predominantly in the mitochondrial fraction, while WHIP and PPP6C were detected in the mitochondrial and cytosol/nuclear fractions. To demonstrate that the WHIP-TRIM14-PPP6C is indeed a mitochondrial complex associated with MAVS, we performed confocal imaging using WT and *MAVS* KO 293T cells. We found that *MAVS* deletion impaired the interaction of WHIP with TRIM14 and PPP6C and excluded the WHIP-TRIM14-PPP6C complex from mitochondria (**Figure 10F, *MAVS* KO vs. WT**), but did not affect WHIP-TRIM14 and TRIM14-PPP6C interactions. Notably, TRIM14 deletion impaired the colocalization of WHIP and PPP6C as well as the mitochondrial localization of WHIP and PPP6C (**Figure 10F, *TRIM14***

KO vs. WT). Together, our data suggest that TRIM14-MAVS interaction is critical for the WHIP-TRIM14-PPP6C complex docking on the mitochondria.

Next, we examined whether the WHIP-TRIM14-PPP6C complex was critical in mediating the RIG-I translocation to the MAVS platform on mitochondria. We first observed the reduction of RIG-I-MAVS interaction in *WHIP* KO or *TRIM14* KO 293T cells (**Figure 10G**). In addition, ligand-stimulated mitochondrial translocation of RIG-I was greatly enhanced by the overexpression of WHIP (**Figure 10H**), indicating that the WHIP-TRIM14-PPP6C complex is essential for RIG-I mitochondria translocation and interaction with MAVS. To examine the sequential events involving WHIP-TRIM14-PPP6C complex interaction with MAVS and RIG-I during viral infection, we treated FLAG-RIG-I stably expressed 293T cells with VSV at different time points, and found that RIG-I interaction with WHIP, TRIM14, PPP6C, and MAVS occurred at 120 min (**Figure 10I**). Moreover, the interaction of RIG-I with TRIM14, WHIP, or PPP6C was abolished in *MAVS* deficient 293T cells (**Figure 10J**), suggesting that the MAVS platform is important for the binding of this complex to RIG-I after viral infection. Our data suggest that MAVS provides an essential mitochondrial platform for the membrane association of WHIP-TRIM14-PPP6C complex, and for the modulation of RIG-I activation and translocation to promote antiviral IFN-I signaling.

Discussion

In this study, we uncovered how the assembly of a mitochondrial MAVS-associated WHIP-TRIM14-PPP6C complex interacts with RIG-I after viral infection and positively regulates RIG-I-mediated innate antiviral signaling. We examined the spatial organization of the WHIP-TRIM14-PPP6C complex and how it operates within the RIG-I pathway, between RIG-I and MAVS, to direct downstream signaling. Our results demonstrate that WHIP mediates the

interactions of RIG-I with TRIM14 and PPP6C, while TRIM14 acts as a co-factor of MAVS to provide a mitochondrial docking-platform for WHIP and PPP6C. 14-3-3ε has been proposed as an essential component of the RIG-I translocation complex at the early stage of RIG-I conformational change induced by dsRNA binding [113]. We report an independent mechanism in the regulation of RIG-I mitochondria translocation. Specifically, K63 polyUb chains at RIG-I K164 provide an essential "ubiquitin-message" for RIG-I cytoplasm-to-mitochondria translocation and RIG-I-MAVS interaction mediated by the ubiquitin-binding domain of WHIP [118]. Importantly, unraveling how the ubiquitin-message is recognized also provides a safety checkpoint, as aberrant ubiquitin-mediated signaling contributes to uncontrollable IFN-I signaling activation and tumor formation [135].

The conserved ATPase domain of RIG-I is important for ATP-driven viral RNA binding and the discrimination of self/non-self RNA [136-138]. ZAPS has been reported to stabilize the RIG-I-RNA complex through ATPase activity [139]. Here we propose that the WHIP ATPase domain promotes WHIP-RIG-I interaction and supports the formation of RIG-I-dsRNA complex. Mutational and ISRE-Luc activity analyses demonstrate that the WHIP T294A mutant, which had a loss of ATPase activity, failed to promote RIG-I-dsRNA interaction compared to WT WHIP, suggesting a physiological role for WHIP interacting with RIG-I. As shown by the reduction of K63 ubiquitination in *WHIP* KO cells, we propose that WHIP has a role in RIG-I ubiquitination: most likely occurring either through 1) the spatial occupation that inhibits the cleavage of K63 poly-ubiquitin chains by deubiquitinases, 2) stabilizing RIG-I/E3 ligase interaction, or 3) enhanced viral RNA-binding.

Serving as an auto-inhibitory mechanism, the N-terminus of RIG-I is highly phosphorylated by PKC [7]. RIG-I can be activated by PP1α or PP1γ through dephosphorylation

after RNA binding, which can be suppressed again through feedback-induced phosphorylation by DAPK1 [116]. Thus, the S8 and T170 phosphorylation status is regulated by dynamic regulatory mechanisms. In our study, we uncovered an additional phosphatase PPP6C, but not the regulatory subunit PPP6R, in the positive feedback regulation of RIG-I CARD dephosphorylation, whose function is independent of PP1. Moreover, we demonstrated that an intact WHIP-TRIM14-PPP6C signalosome was necessary for RIG-I dephosphorylation by PPP6C, because of deletion of either WHIP or TRIM14 impaired PPP6C-stimulated ISRE-Luc activity. Importantly, as a positive regulator in IFN-I signaling, PPP6C might provide a potentially important link between inflammation and the role of PPP6C in cancer progression and tumor immunity [64, 119, 120, 140].

Based on our findings, we propose a working model for the WHIP-TRIM14-PPP6C signalosome in mediating RIG-I activation and innate immune signaling transduction (**Figure 11**). The mitochondrial WHIP-TRIM14-PPP6C complex constitutively interacts with MAVS through the interaction between TRIM14 and MAVS and interacts with RIG-I in an inducible manner (i.e., only after poly(I:C) stimulation or VSV infection). Upon viral infection, WHIP protein (UBD in the N-terminus) interacts with RIG-I to stabilize RIG-I-dsRNA complex and promote RIG-I K63 ubiquitination through ATPase activity. WHIP promotes the translocation of RIG-I to MAVS mitochondrial platform. The PPP6C of the WHIP-TRIM14-PPP6C complex can dephosphorylate RIG-I to maintain the RIG-I activation. Thus, this signalosome plays critical roles in activating the RIG-I function and bridging RIG-MAVS interaction for IFN-I signaling and antiviral immunity. Targeting WHIP-TRIM14-PPP6C function may offer attractive therapeutic strategies to modulate immune signaling for the control of RNA virus infection.

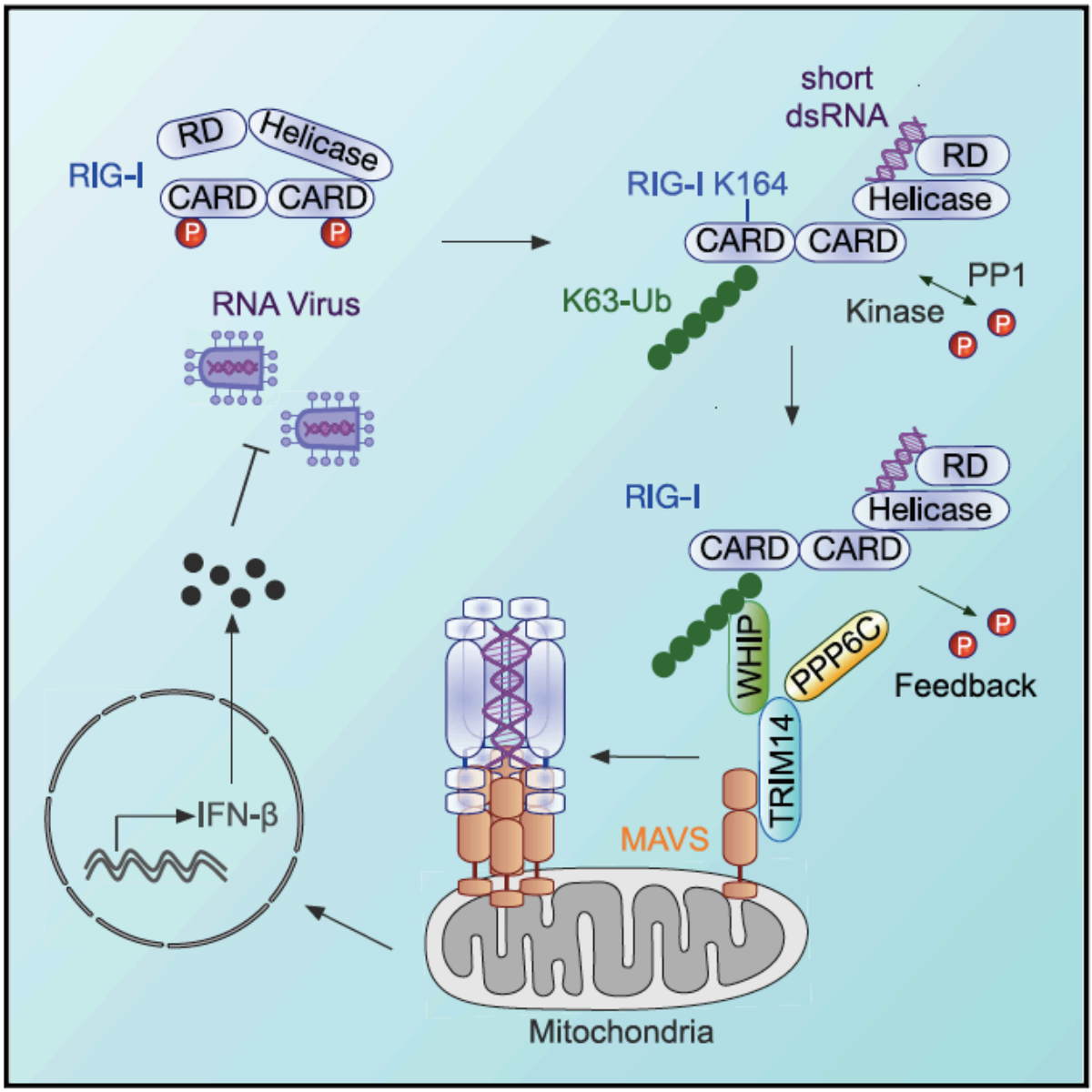

Figure 11. Working model for WHIP-TRIM14-PPP6C in RIG-I signaling. A proposed model illustrates how WHIP-TRIM14-PPP6C complex functions in RLR-mediated signaling. In uninfected cells (no stimulation), WHIP-TRIM14-PPP6C complex interacts with MAVS and docks on the mitochondrial membrane. Upon VSV or SeV infection, binding of dsRNA by RIG-I leads to conformational change and K63 poly-ubiquitination at the Lys164 site. WHIP UBD binds to K63 polyUb chains of RIG-I at the Lys164 site and bridges ubiquitinated RIG-I and TRIM14-MAVS complex. ATPase activity of WHIP stabilizes RIG-I-dsRNA interaction. Phosphatase activity of PPP6C further augments RIG-I activation.

CHAPTER III

MYELOID LOSS OF BECLIN1 ENABLES THE MALIGNANT TRANSFORMATION OF PD-L1^{+} PRECURSOR B CELLS

Introduction

Autophagy has been recognized as a key intracellular degradation and recycling machinery for maintaining cellular homeostasis, whose dysregulation may lead to cancer and other diseases [141]. Beclin-1 (Becn1) acts as the core component of the class III phosphatidylinositol 3-kinase Vps34 complex, which is critical for the initiation of autophagy and autophagosome formation [80]. Becn1 functions as a tumor suppressor to prevent tumor development, as monoallelic deletion of *Becn1* results in the spontaneous tumor formation including lymphoma [142, 143]. However, Becn1 haploinsufficiency also reduces spontaneous renal tumor formation in *Tsc2*$^{+/-}$ mice [144]. The critical role of Becn1 in tumorigenesis by autophagy-dependent or -independent mechanisms using cell-type specific deletion mouse model remains unclear.

Inflammation triggered by the activations of innate immune signaling, including NF-κB, type I interferon (IFN) and inflammasome, leading to the expression of pro-inflammatory cytokines, allowing tumor cells to evade immune surveillance [145, 146]. For example, macrophage-derived TNF-α induces expression of CSN5 to stabilize immune checkpoint molecule PD-L1 [78]. Cdk5 promotes IFN-γ-induced PD-L1 expression by suppressing PD-L1 transcriptional repressors interferon regulatory factors IRF2 and IRF2BP2 [69]. Autophagy-related genes have well-established functions in modulating cancer cell signaling in both autophagy-dependent and -independent manner [81, 101]. However, the non-cell-autonomous role of myeloid-specific Becn1 in the regulation of tumor inflammation remains largely unknown.

Intensive studies have been focused on the cause of B cell malignancies by aberrant precursor (pre)-B cell receptor (pre-BCR) and BCR signaling, chromosomal translocation and oncogenic mutations within cancer cells [147]. However, recent studies show that tumor cells rely on the interactions of myeloid cells (Gr-1^{+}CD11b^{+} neutrophils and F4/80^{+}CD11b^{+} macrophages) and tight-junction (TJ) molecules that constitute the tumor microenvironment [148, 149]. B-cell lymphomas can escape T-cell-mediated cellular cytotoxicity by exploiting the inhibitory PD-1/PD-L1 immune checkpoint [150]. Recruitment of these myeloid populations has been proposed as possible mechanisms for immune suppression in the tumor microenvironment [76, 79]. However, signaling pathways that regulate the properties of tumor-supportive myeloid cells and factors that drive the metastatic tumor progression through the expression of immune checkpoint molecules are still elusive.

In this study, we identify Becn1 as a negative regulator of p38 signaling in an autophagy-independent manner. Importantly, we showed a high incidence (~25%) of spontaneous pre-B cell lymphoma development in mice with myeloid-specific ablation of *Becn1*. Tumor-bearing mice exhibited loss of tight-junction molecules but an accumulation of neutrophils with B cell helper properties at the invasive edge of tumor cells through CXCR3/CXCL9 chemotaxis. Persistent activation of STAT3 and NF-kB p52 signaling and robust induction of MHC class I, PD-L1, and anti-apoptotic genes were evident in these high-metastatic tumors. Analysis of human pre-B acute lymphoblastic lymphoma/leukemia patient samples revealed the low expression of Becn1 in tumor-infiltrated neutrophils. Our findings identify a previously unrecognized role of Becn1 in immune checkpoint regulation of malignant pre-B cells.

Methods and Materials

Animals and in vivo procedures

Adult C57BL/6 (CD45.2) and Boy/J (CD45.1) mice were obtained from the Jackson Laboratory. *Becn1*^{flox} mice (Knockout Mouse Project Repository [KOMP]) were crossed with lysozyme-Cre (Lyz2-Cre) mice (Jackson Laboratory) to obtain *Becn1*$^{\Delta M}$ mice on the C57BL/6 background. Mouse genotyping primers to detect WT and flox/flox mutant were as follows: 1) Becn1-1R: 5'- GCGGATCCCTGAGTTCTAGACTAACC-3'; 2) Becn1-1F (ttR): CTCCCAATGCTGGGATTAAAGACG-3'; and 3) Becn1-2R (F): TTGTACCGTGATTTAGGGCGTTTGC-3'. *Becn1*$^{\Delta M}$ mice were bred with *Mapk14* ^{flox} mice (provided by Y. Wang, UCLA, and H. Jiang, Boehringer-Ingelheim) [151] or *Il6* $^{-/-}$ mice (Jackson laboratory) to generate *Becn1*$^{\Delta M}$:*Mapk14*$^{\Delta M}$ and *Becn1*$^{\Delta M}$:*Il6*$^{-/-}$ mice, respectively. To generate *Becn1* and *Map3k3* double knockout BM chimeric mice, deletion of *Map3k3* was achieved by the clustered regularly interspaced short palindromic repeats (CRISPR)-Cas9 system [152]. We used the following single-guide (sg) RNA sequences to target exon1 of *Map3k3*: 1) sg-Map3k3-Forward, 5′-CACCGACCGGGTTCGTCGGCTCATC-3′ and 2) sg-Map3k3-Reverse, 5′-AAACGATGAGCCGACGAACCCGGTC-3'. And non-targeting mouse sgRNA as control: 1) sg-Control-Forward, 5'-CACCGGCGAGGTATTCGGCTCCGCG-3' and 2) sg-Control-Reverse, 5'-AAACCGCGGAGCCGAATACCTCGCC-3'. Total BM was isolated from the femur and tibia of 6 to 10-week-old female C57BL/6 wild-type mice or *Becn1*$^{\Delta M}$ mice. BM was subjected to erythrocyte lysis (BD PharmLyse, BD Bioscience), followed by magnetic bead selection of cKit-positive cells using CD117 MicroBeads (Miltenyi Biotec). Prior to flow sorting using BD FACSAria II, CD117-selected cells were stained with APC-labeled cKit (eBioscience), PE-labeled Sca1 (BioLegend), PacificBlue-labeled Gr1, CD11b, B220(CD45R), Ter119, and CD3 (all from

eBiosciences). LSK cells were cultured in StemPro®-34 SFM complete medium (ThermoFisher) supplemented with 50 ng/ml murine Thpo and 50 ng murine Scf (both Life technologies) for 48 h and then transduced with concentrated lentiviral supernatant in presence of 2 μg/ml Polybrene. 24 h post-transduction cells were collected and intravenously injected into lethally irradiated (950 cGy) 6 to 10-week-old female C57BL/6 mice (Jackson Laboratory). Since the CRISPR-Cas9 genotyping data provided only a 'snapshot' of the polyclonal cell population genotype, the possibility that not all alleles had been targeted by this approach could not be ruled out. For BM chimeras, approximately 1.5 x 10^6 total BM cells from CD45.1$^+$ donors were mixed with 1.5 x 10^6 total BM cells from adult WT (CD45.2$^+$) or *Becn1*$^{\Delta M}$ (CD45.2$^+$) mice and then were transferred into adult WT CD45.1 mice that had been exposed to 950 cGy. Chimeras were analyzed at least 6 weeks after reconstitution. To study *in vivo* endotoxicity, mice received intraperitoneal (i.p.) injection of LPS (25–30 mg/kg), and blood samples were collected to assay plasma cytokine concentrations. Animal experiments were approved by the Institutional Animal Care and Use Committee of Houston Methodist Research Institute.

RNA-seq

Total RNA was used for mRNA isolation and cDNA library generation with miRNeasy micro Kit (Qiagen). On-column DNase digestion (DNase-Free DNase Set, Qiagen) was performed according to manufacturer protocols to prevent genomic DNA contamination. RNA and library preparation integrity were verified using a 2100 BioAnalyzer system (Agilent). Ribosomal RNA depletion was performed following the low input protocol by RiboMinus Eukaryote System v2 (ThermoFisher) with 500 ng total RNA input. Finally, libraries were prepared using the Ion Total RNA-Seq Kit v2 (ThermoFisher) with minor changes to the standard protocol. These included lower amplification cycles and the usage of entire fragmented RNA for cDNA synthesis. For the

sequencing reactions, an Ion Torrent Proton platform with V3 chemistry (Ion PI Template OT2 200 Kit v3, ThermoFisher) and PIV2 Chips (Ion PI™ Chip Kit v2, ThermoFisher) were used. The experiment was performed on two chips containing two biological replicates per condition (wt1/mt1 on chip A and wt2/mt2 on chip B) resulting in 163 million total reads and at least 40 million reads per library. Base-calling was performed on Ion Torrent suite software. Raw sequencing reads in FASTQ format were aligned to the UCSC mouse reference genome (mm10) using TOPHAT21 [153]. Differentially expressed genes were identified using DESeq2 version 1.62 [154]. Only genes with a minimum fold change of +/− 2, a maximum Benjamini-Hochberg corrected p-value of 0.05, and a minimum combined mean of 5 reads were classified as having significant differential expression. Gene set enrichment analysis (GSEA) software was used to perform GSEA against the GSEA database was used [155]. Data were also analyzed with Ingenuity Pathway Analysis (IPA) software (Ingenuity Systems, www.ingenuity.com).

Isolation of immune cells

BM cells were isolated from the tibia and femur and cultured in RPMI1640 medium with 10% FBS, 1% penicillin-streptomycin, 55 mM β-mercaptoethanol, and 10% L929 conditioned media containing macrophage-colony stimulating factor for 5 days for BM-derived macrophages (BMDMs), 20 ng/mL murine GM-CSF and 10 ng/ml IL-4 for 6–8 days for conventional DCs. Peritoneal macrophages were obtained by injecting mice Intraperitoneally (i.p.) with 4% (v/v) thioglycollate (Beckton Dickson) and peritoneal cavities were flushed after 3 days with RPMI 1640 media with 2% FBS. Mouse CD4 cells were isolated from SP or LN by using Dynabeads® untouched mouse CD4 cells kit (ThermoFisher). 10^8 cells/mL of splenocytes and LN cells were blocked with heat inactivated FBS and antibody mix against CD8, B220, CD11b, Ter-119 and CD16/32. After 20 min incubation at 4°C, cells were washed with isolation buffer (PBS (Ca^{2+} and

Mg^{2+} free) supplemented with 0.1% BSA and 2 mM EDTA) and incubated with pre-washed mouse depletion dynabeads for 15min at room temperature (RT). Resuspended beads-bound cells by gently pipetting were placed in the magnet for 2min. Untouched $CD4^+$ T cells in the supernatant were then collected. Similarly, total B cells were isolated from tumor, LN, SP or BM by using mouse CD45R (B220) microbeads (Mitenyi Biotec) or PE-positive selection beads with PE-B220 antibody. Peripheral neutrophils were obtained from the peritoneal cavity by i.p. injection of mice with 2 ml 4% (v/v) thioglycollate for 4 h followed by collection of peritoneal exudates with RPMI 1640 media with 2% FBS. Cells were stained with anti-Gr-1-PE (eBioscience) and purified with PE-positive selection magnetic beads (Stem Cell Technologies), or using EasySep Mouse Neutrophil Enrichment Kit (Stem Cell Technologies) to remove non-neutrophil populations. Tissue infiltrated neutrophils were purified from intraparenchymal pulmonary or LN cell suspensions using similar isolation method as peritoneal neutrophils. Briefly, for lung neutrophil isolation, the chest of the mouse was opened, and the lung vascular bed was flushed with 2–3 ml of pre-chilled PBS injected into the right ventricle. Lungs were excised to avoid the paratracheal LNs and thymus and washed twice in RPMI 1640 media supplemented with penicillin/streptomycin. The excised lungs were minced finely, and the tissue pieces were placed in RPMI 1640 medium containing 2% FBS, 20 U/ml collagenase, and 1 g/ml DNase. Following incubation for 60 min at 37°C, any remaining intact tissue was disrupted by passage through a 21-gauge needle. Tissue fragments and the majority of dead cells were removed by rapid filtration through a glass-wool column, and cells were collected by centrifugation. Cells were subjected to the enrichment using anti-Gr-1-PE and PE-positive selection or EasySep Mouse Neutrophil Enrichment Kit.

Immunoprecipitation and immunoblot analyses

For immunoprecipitation, whole-cell lysates were incubated overnight with indicated antibodies plus protein A and G beads (Pierce). For immunoprecipitation with anti-FLAG, anti-FLAG agarose gels were used. Beads were then washed five times with low-salt lysis buffer (50mM HEPES,15mM NaCl, 1mM EDTA, 1.5mM MgCl2, 10% Glycerol, 1% Triton X-100), and immunoprecipitates were eluted with 4 x SDS loading buffer. Immunoblotting was performed by resolving protein lysates on SDS-PAGE gels, followed by a transfer to nitrocellulose membranes (Bio-Rad), and further incubating membranes with indicated antibodies overnight. For all blots, EMD Millipore Luminata Western HRP Chemiluminescence Substrate was used for protein detection.

Flow cytometry

Cell surface staining, intracellular cytokine staining, flow cytometry, and cell sorting were performed as described previously [124]. Single-cell suspensions were obtained from tissues and stained for 30 min with indicated antibodies. Flow cytometric analysis was performed with BD LSRII Flow Cytometer (Becton Dickson), and data were analyzed by BD FACSDiva software.

Cytokine release assay

Cell supernatants or sera were collected at indicated time points after stimulation with LPS with or without ATP. Cytokine concentrations were measured by ELISA with anti-mouse TNF-α, IL-6, IL-1β, IL-17A, IL-17F, IL-21, IL-22, and BAFF antibodies. ELISAs were performed according to the manufacturer's instructions. In brief, 96-well plate was pre-coated with the capture antibody (1:500 in coating buffer) at 4°C overnight. On the next day, the plate was washed with PBS/0.1%Tween 20 and blocked with 1%BSA/PBS diluent buffer for 2 h at RT. Diluted supernatants and cytokine standards were then applied to the plate and incubated for 2 h at RT.

The plate was then washed and incubated with biotin-conjugated detection antibody (1:1000 in 1%BSA/PBS diluent buffer) for 1 h at RT. The plate was then washed and incubated with poly-HRP streptavidin (1:5000 in diluent buffer, Thermo Scientific) for 30 min. The plate was washed again and finally incubated with the tetramethylbenzidine substrate solution (Sigma-Aldrich). The reaction was stopped using 2 M H_2SO_4. Absorbance of each well was recorded by Synergy™ 2 plate reader (Biotek) at 450nm. The absorbance of the standard sample was used to construct the standard curve.

Hematological and histological analysis

Complete peripheral blood counts were performed with an automated hematology analyzer (Hemavet 850; Drew Scientific). For whole BM sections, specimens were decalcified in (8%) hydrochloric acid/ (8%) formic acid working solution overnight, followed by neutralization by ammonia solution for 30 min and embedded in paraffin. Embedded BM blocks were sliced and stained with H&E for conventional morphological assessment. For cytocentrifugation preparations, BM cells were subjected to red blood lysis in ACK buffer (0.15 mM NH_4Cl, 1 mM $KHCO_3$, and 0.1 mM Na_2EDTA). Between 2 - 5 × 10^5 cells were suspended in 100 µl PBS, loaded onto disposable Cytofunnel chambers, and centrifuged for 4 min at 400 RPM using a CytoSpin III cytocentrifuge (Shandon). For May-Grünwald Giemsa stain, cytocentrifuged samples were stained in May-Grünwald solution (MG500; Sigma-Aldrich) for 2 min and in Giemsa (GS500, 5% solution in water; Sigma-Aldrich) for 12 min, followed by two washes in distilled water for 30 s. Thereafter, samples were cytocentrifuged, counterstained with May-Grünwald solution for 10 s and washed in water. Slides were coverslipped using Permount and analyzed by brightfield microscopy. IHC staining was performed using the streptavidin-biotin-peroxidase complex method using Vectastain Elite ABC kit and DAB peroxidase (HRP) substrate kit. Negative control

staining was performed using mouse, rabbit, or rat immune sera instead of the primary antibodies. Sections of human B cell lymphoblastic leukemia/lymphoma tissues were obtained from Dr. James You (UT MD Anderson Cancer Center, Houston, TX), including 10 pre-B ALL in LN or BM and 6 reactive LN or BM controls. Immunofluorescence assays and confocal microscopy were conducted using fluorescent secondary antibodies. Samples were visualized using Nikon Eclipse Ti-E microscope. All acquired images were analyzed using the Nikon NIS-Elements AR package or the ImageJ (NIH) software.

In vivo cell depletion

Monocyte and macrophage depletion was performed by i.v. injection of 250 µl clodronate-containing liposomes (Encapsula NanoSciences) on day -1 relative to LPS treatment. Control liposomes were used as PBS control. Neutrophil/granulocyte depletion was induced with combined 0.5 mg of anti-Gr1 mAb clone 1A8 (BioXcell) and 0.1 mg of RB6-8C5 [156] or with PBS controls i.p. injection into mice on days -3, -2, and -1 relative to LPS treatment.

Real-time RT-PCR analysis

Total RNA was isolated from cells using RNeasy RNA isolation kit (QIAGEN) and reverse transcribed using SuperScript III Reverse Transcriptase (Invitrogen) as per manufacturer's directions. Quantitative PCR was conducted on the ABI Prism 7000 analyzer (Applied Biosystems) using SYBR GreenER qPCR Super Mix Universal (Invitrogen). mRNA levels were normalized to Gapdh and relative levels were determined using ΔΔct method.

GEP of human lymphomas

Gene expression analysis was performed on datasets from Gene Expression Omnibus (GEO, https://www.ncbi.nlm.nih.gov/geo/) including GSE12195, GSE26673, GSE16455,

GSE12195, GSE16455, GSE7440, GSE11877. Specifically, we included the following cancer types: 16 BL, 18 CLL, 38 FL, 75 DLBCL, 22 MCL, 4 MZL, 306 B-ALL, and 5 naïve cell samples. Data was processed by Affymetrix Expression Console. Statistical differences among multiple groups were analyzed with one-way analysis of variance (ANOVA) test. Significant differences were determined when P value is less than 0.05.

The DAVID/EASE software was used to establish whether specific cell functions and biologic processes, defined according to gene ontology [157], were significantly represented among the deregulated genes [158].

Results

Myeloid Becn1 ablation induces splenomegaly and lymphadenopathy with neutrophilia

To investigate the role of Becn1 in myeloid lineage development and innate immune response, we crossed *Becn1$^{f/f}$* mice with mice expressing the lysozyme promoter-driven *Cre* recombinase gene (*Lyz2-Cre*), designated as *Becn1$^{\Delta M}$ mice*. Conditional Becn1 deletions in F4/80^{+}CD11b^{+} peritoneal macrophages (pMAC) and Gr-1^{+}CD11b^{+} neutrophils were verified by polymerase chain reaction (PCR) and immunoblot analyses compared to CD11c^{+} conventional dendritic cells (cDCs), CD4^{+} T cells, and CD19^{+} B cells (**Figure 12A**). Notably, *Becn1$^{\Delta M}$* mice developed splenomegaly and profound enlargement of inguinal, axillary and mesenteric lymph nodes (LNs) (**Figures 12B and 12C**). Histological analysis of spleen sections revealed a marked effacement of the splenic architecture with loss of marginal zone barriers and a concomitant loss of the clear-cut delimitation between the lymphoid and myeloid parenchyma (**Figure 12D**).

Loss of myeloid-specific Becn1 markedly increased the number of Gr-1^{+}CD11b^{+} neutrophils in the bone marrow (BM) and spleen (SP). However, the percentage of F4/80^{+}CD11b^{+} macrophage did not change (**Figures 12E and 12F**). In addition, we found a significant increase

of total spleen B220$^+$ B cells (**Figure 12G**). Together, our results suggest that neutrophilia in *Becn1*$^{\Delta M}$ mice is driven by factors intrinsic to hematopoietic cells, causing accelerated proliferation and/or enhanced survival of neutrophil progenitors or mature neutrophils.

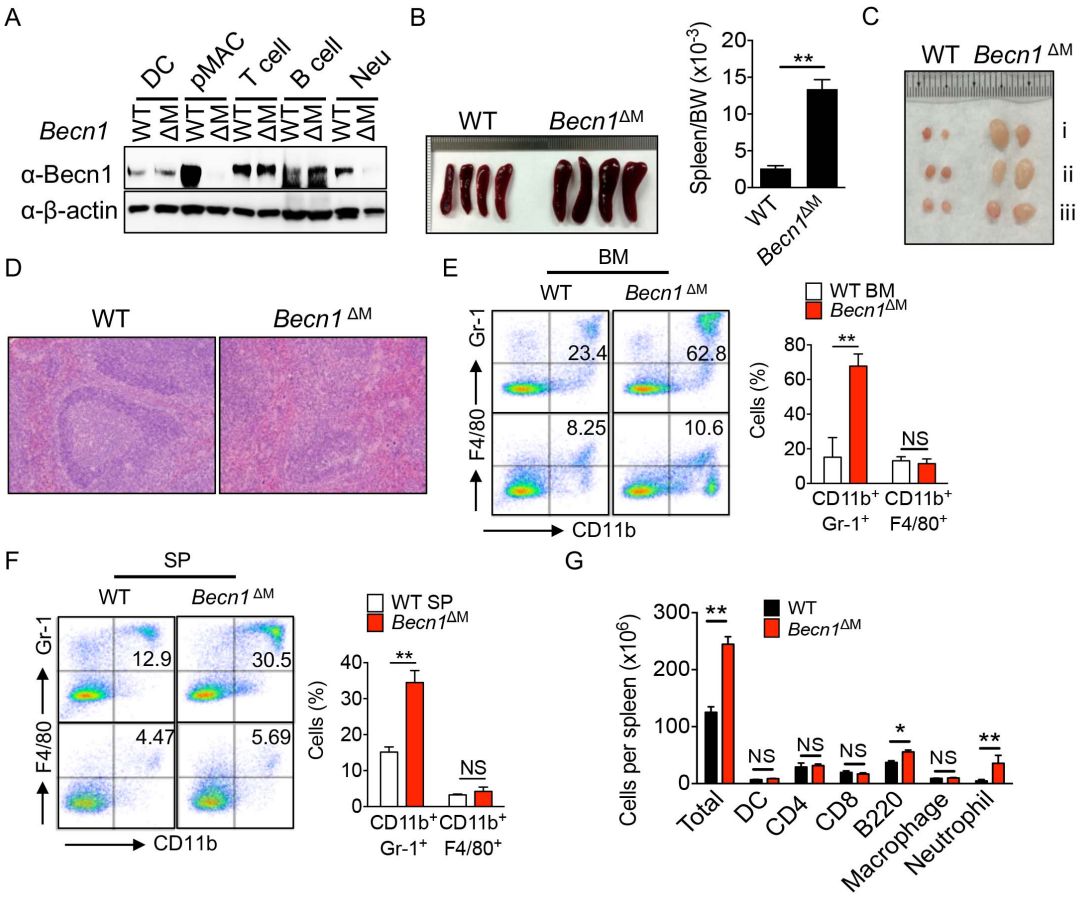

Figure 12. Characterization and phenotypic analysis of *Becn1*$^{\Delta M}$ mice. (A) Immunoblot analysis of Becn1 protein expression with anti-Becn1 in dendritic cells (DC), peritoneal macrophages (pMAC), T cells, B cells, and neutrophils (Neu). (B and C) Spleen size comparison between WT and *Becn1*$^{\Delta M}$ mice (B, left) and spleen/ body weight ratio (B, right) and lymphadenopathy in *Becn1*$^{\Delta M}$ mice compared with WT control (C), Inguinal(i), axillary(ii), and mesenteric(iii) lymph nodes were examined. (D) H&E (hematoxylin & eosin) staining of spleen sections from WT and *Becn1*$^{\Delta M/\Delta M}$ mice. (E and F) Flow cytometric and statistical analysis of Gr-1$^+$CD11b$^+$ neutrophils and F4/80$^+$CD11b$^+$ macrophage in bone marrow (E) and spleen (F) of WT and *Becn1*$^{\Delta M}$ mice. BM, bone marrow; SP, spleen. (G) A total number of splenic CD45$^+$CD11c$^+$ DCs, CD4$^+$ T cells, CD8$^+$ T cells, B220$^+$ B cells, CD11b$^+$F4/80$^+$ macrophages, CD11b$^+$Gr-1$^+$ neutrophils obtained from the fraction of each population on the basis of the expression of surface marker multiplied by the total number of spleen cells. Data shown are plotted as the mean ± s.d. and are representative of three independent experiments. *P <0.05, **P <0.01, NS (not significant) vs. corresponding control.

Neutrophil Becn1 negatively regulates p38 activation and IL-17-related cytokine

We next examined TLR-mediated innate immune signaling responses between WT and Becn 1-deficient cells and found the increased p38 MAPK activity and slightly reduced IKK activation after LPS (a TLR4 ligand) stimulation in neutrophils but not macrophages (**Figures 13A and 13B**). Becn1-deficient neutrophils produced a higher amount of TNF-α and IL-1β, whereas pMAC produced higher amounts of TNFα and IL-6 (**Figure 13C**). Consistently, we observed an increase in basal expression of pro-IL-1β in Becn1-deficient neutrophils (**Figure 13D**). To further define the physiological function of Becn1, we show that *Becn1*$^{\Delta M}$ mice died after LPS-induced endotoxin shock (30 mg/kg) within 12 h, compared to WT mice that survived for up to 40 h (**Figure 13E**). Consistent with this observation, *Becn1*$^{\Delta M}$ mice had markedly elevated serum concentrations of pro-inflammatory cytokines such as TNF-α, IL-6, and IL-1β after LPS treatment (**Figure 13F**). We found that macrophage depletion did not show a difference in survival after LPS-induced septic shock. However, there was significantly prolonged survival in mice depleted of neutrophils (**Figure 13G**), indicating that neutrophils play a dominant role in LPS-induced septic shock. These results suggest that Becn1 deletion in myeloid cells enhances the sensitivity and severity of LPS-induced septic shock and is associated with increased serum concentrations of pro-inflammatory cytokines. To determine the role of Becn1 in the regulation of neutrophil-mediated innate immune signaling and gene expression, we performed the RNA-seq analysis of freshly isolated neutrophils followed by 4h LPS treatment. Interestingly, we observed marked upregulation of genes involved in pathways related to inflammation, rheumatoid arthritis and inflammatory bowel disease (**Figures 13H**). These included genes encoding the IL-17 and related cytokines, chemokine receptor and neutrophil-chemotaxis, cell metabolism, and neutrophil-mediated immunity. Consistently, we found elevated serum levels of IL-17A, IL-17F, IL-21 and

IL-22 in *Becn1*$^{\Delta M}$ mice (**Figure 13I**). We next isolated Becn1-deficient neutrophils and peritoneal macrophages and treated them with LPS and found significantly higher levels of IL-17A in Becn1-deficient neutrophils, compared with WT controls or macrophages (**Figure 13J**). Next, we examined the mRNA expression of key lineage transcription factors such as *Rorc, Ahr, Irf4, and Stat3* that drive IL-17 family cytokine production [159]. *Rorc* was found to be dramatically upregulated, but the other transcription factors such as Ahr, IRF4, and Stat3 in Becn1-deficient neutrophils remained unchanged (**Figure 13K**). RORγt inhibitor GSK805 [160, 161] also suppressed the transcription of IL-17 cytokine in Becn1-deficient neutrophils (**Figure 13L**). Together, our results suggest that Becn1 deletion promotes neutrophils to produce IL-17 and related cytokines.

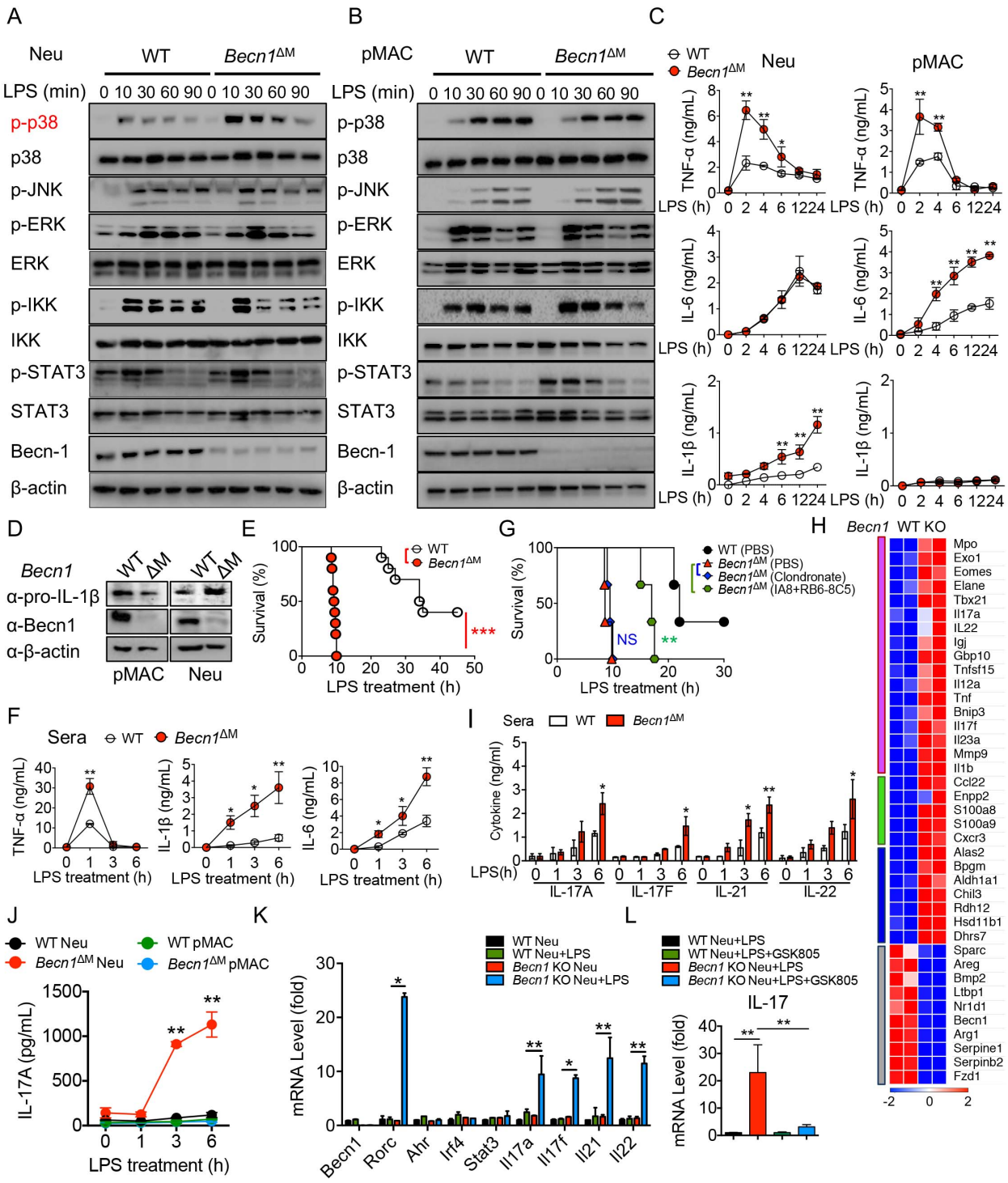
A
Neu
WT
Becn1ΔM
LPS (min) 0 10 30 60 90 0 10 30 60 90
p-p38
p38
p-JNK
p-ERK
ERK
p-IKK
IKK
p-STAT3
STAT3
Becn-1
β-actin
B
pMAC
C
WT
Becn1ΔM
Neu
pMAC
TNF-α (ng/mL)
IL-6 (ng/mL)
IL-1β (ng/mL)
LPS (h) 0 2 4 6 1224
D
Becn1
α-pro-IL-1β
α-Becn1
α-β-actin
pMAC
Neu
E
Survival (%)
LPS treatment (h)
***
G
WT (PBS)
Becn1ΔM (PBS)
Becn1ΔM (Clondronate)
Becn1ΔM (IA8+RB6-8C5)
NS
**
H
Becn1 WT KO
Mpo
Exo1
Eomes
Elane
Tbx21
Il17a
IL22
Igj
Gbp10
Tnfsf15
Il12a
Tnf
Bnip3
Il17f
Il23a
Mmp9
Il1b
Ccl22
Enpp2
S100a8
S100a9
Cxcr3
Alas2
Bpgm
Aldh1a1
Chil3
Rdh12
Hsd11b1
Dhrs7
Sparc
Areg
Bmp2
Ltbp1
Nr1d1
Becn1
Arg1
Serpine1
Serpinb2
Fzd1
-2 0 2
F
Sera
WT
Becn1ΔM
TNF-α (ng/mL)
IL-1β (ng/mL)
IL-6 (ng/mL)
LPS treatment (h)
I
Sera
WT
Becn1ΔM
Cytokine (ng/ml)
LPS(h) 0 1 3 6
IL-17A
IL-17F
IL-21
IL-22
J
WT Neu
Becn1ΔM Neu
WT pMAC
Becn1ΔM pMAC
IL-17A (pg/mL)
LPS treatment (h)
K
WT Neu
WT Neu+LPS
Becn1 KO Neu
Becn1 KO Neu+LPS
mRNA Level (fold)
Becn1
Rorc
Ahr
Irf4
Stat3
Il17a
Il17f
Il21
Il22
L
WT Neu+LPS
WT Neu+LPS+GSK805
Becn1 KO Neu+LPS
Becn1 KO Neu+LPS+GSK805
IL-17
mRNA Level (fold)

Figure 13. Cell type-specific regulation of Becn1 in pro-inflammatory pathways. (A and B) WT or Becn1-deficient Neu (A) or pMAC (B) were treated with LPS for the indicated time points, followed by immunoblot analysis of phosphorylated IKK (p-IKK), p-p38, p-JNK, p-ERK, p-STAT3, IKK, p38, ERK, JNK, and STAT3 with cell lysates. (C) ELISA measurement of TNF-α, IL-6 and IL-1β production by Neu and pMAC after 100 ng/mL LPS treatment for indicated time points. (D) Immunoblot analysis of basal intracellular pro-IL-1β in pMAC and Neu. (E) Survival of WT and *Becn1*$^{\Delta M}$ mice (n = 10 per group) after high-dose LPS (30 mg/kg) challenge. (F) Plasma concentrations of TNF-α, IL-6, and IL-1β in mice at indicated time points after LPS treatment. (G) Survival of WT and *Becn1*$^{\Delta M}$ mice (n = 3 per group) treated with PBS- or clodronate-containing liposomes to deplete macrophages or treated with the anti-Ly6G antibody (1A8 and RB6-8C3) to deplete neutrophils followed by treatment with high-dose LPS (30 mg/kg i.p.). (H) Heatmap representation of genes significantly induced (top) or downregulated (bottom) in neutrophils isolated from *Becn1*$^{\Delta M}$ mice compared to WT controls, including neutrophil-mediated immunity and IL17 related cytokines (purple), chemokine receptor and neutrophil-chemotaxis (green), cell metabolism (blue). (I) ELISA measurement of serum IL-17A, IL-17F, IL-21, and IL-22 production in WT and *Becn1*$^{\Delta M}$ mice after treatment with LPS (30 mg/kg i.p.). (J) ELISA measurement of IL-17A production in WT or Becn1-deficient Neu or pMAC after100 ng/mL LPS treatment for indicated time points. (K) Quantitative RT-PCR of *Becn1, Rorc, Ahr, Irf4, Stat3, Il17a, Il17f, Il21* and *Il22* mRNA in Neu isolated from WT and *Becn1*$^{\Delta M}$ mice. (L) Quantitative RT-PCR of *Il17a* mRNA level in Neu isolated from WT and *Becn1*$^{\Delta M}$ mice treated with LPS for 6 h along with DMSO or 0.5 μM GSK805. Data shown are plotted as the mean ± s.d. and are representative of three independent experiments. **P* <0.05, ***P* <0.01, NS (not significant) vs. corresponding control.

Autophagy-independent degradation of MEKK3 by Becn1 is cell-type specific

NF-κB and MAPK pathways through MAP3Ks (TAK1, ASK1, MEKK3) activation triggers downstream signaling of IKK complex, Erk1/2, p38, and JNK [34]. We tested whether Becn1 interacted with key signaling molecules in 293T cells, and found that Becn1 strongly interacted with MEKK3 and MKK3, and weakly with IKKβ and NEMO (**Figures 14A and 14B**). Importantly, increased amounts of Becn1 markedly reduced MEKK3 protein in 293T cells (**Figure 14C**). Consistently, we found that endogenous MEKK3 was increased in Becn1-deficient neutrophils, but not macrophages, with increased p38 phosphorylation (**Figures 14D and 14E**). These results suggest that Becn1 regulates MEKK3 stability and MEKK3-p38 signaling in the neutrophils.

To understand how Becn 1 regulates MEKK3 for degradation, we showed that proteasome inhibitor MG132, but not autophagy inhibitors 3-Methyladenine (3-MA) or chloroquine (CQ), blocked Becn1-mediated MEKK3 degradation (**Figure 14G**), suggesting that Becn1 degrades MEKK3 through a proteasome-dependent manner. Protein ubiquitination has emerged as an important mechanism to target a protein for proteasomal degradation [162]. By analyzing the conjugation of various ubiquitin moieties, we found that Becn1 mediated MEKK3 degradation mainly through K48 ubiquitination (**Figures 14H and 14I**). To identify key lysine residues in MEKK3 required for K48 ubiquitination, we substituted a series of lysine residues with arginine and found that lysine 299 (K299) residue is essential in Becn1-mediated MEKK3 ubiquitination and proteasome degradation (**Figures 14J and 14K**). These results suggest that Becn1 targets MEKK3 for ubiquitination-dependent proteasomal degradation through K299 residue in MEKK3.

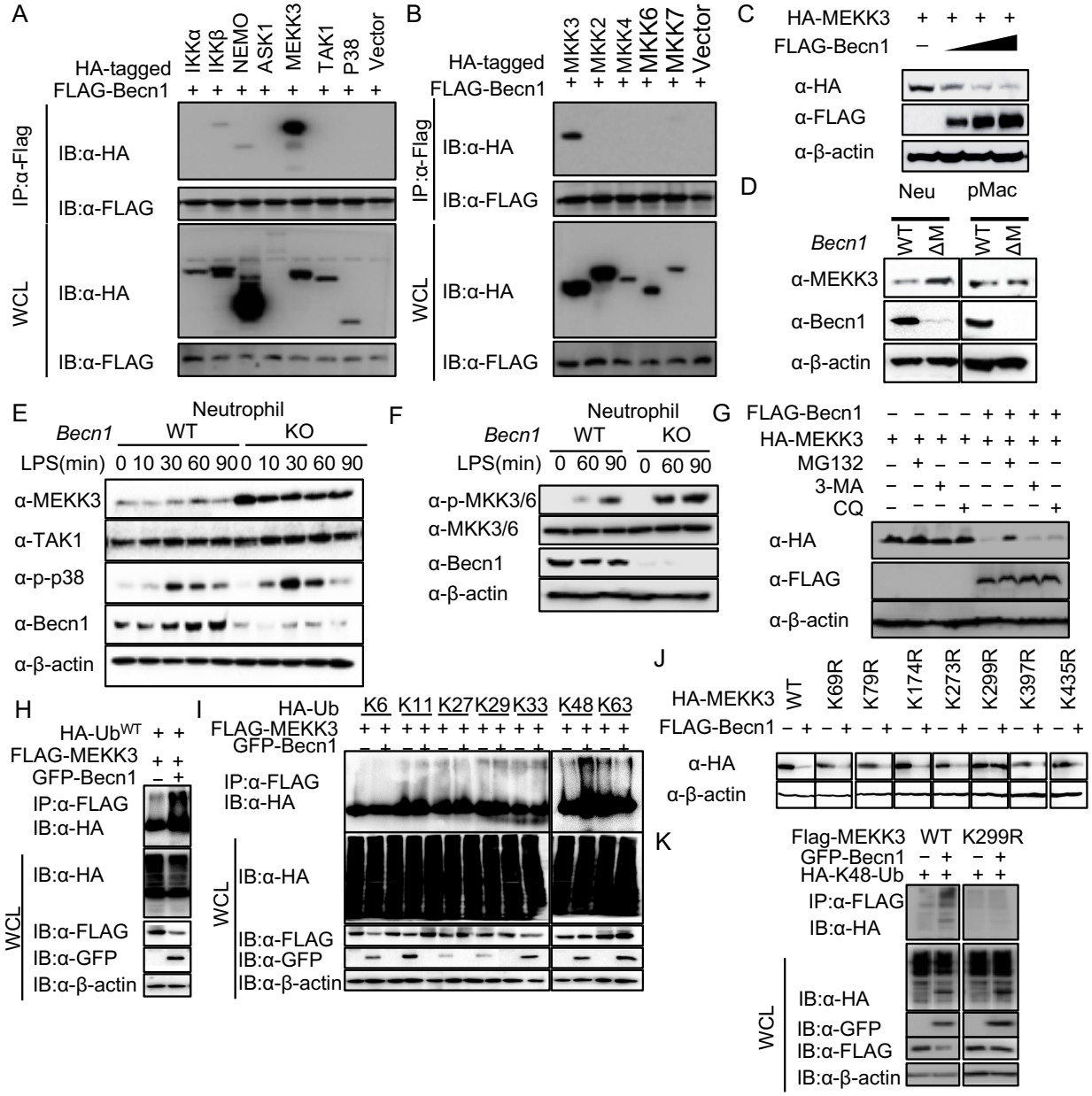
A
HA-tagged
FLAG-Becn1
IKKα
IKKβ
NEMO
ASK1
MEKK3
TAK1
P38
Vector
IP:α-Flag
IB:α-HA
IB:α-FLAG
WCL
B
HA-tagged
FLAG-Becn1
+ MKK3
+ MKK2
+ MKK4
+ MKK6
+ MKK7
+ Vector
C
HA-MEKK3
FLAG-Becn1
α-HA
α-FLAG
α-β-actin
D
Neu
pMac
Becn1
WT
ΔM
α-MEKK3
α-Becn1
α-β-actin
E
Neutrophil
Becn1
WT
KO
LPS(min) 0 10 30 60 90 0 10 30 60 90
α-MEKK3
α-TAK1
α-p-p38
α-Becn1
α-β-actin
F
Neutrophil
Becn1
WT
KO
LPS(min) 0 60 90 0 60 90
α-p-MKK3/6
α-MKK3/6
α-Becn1
α-β-actin
G
FLAG-Becn1
HA-MEKK3
MG132
3-MA
CQ
α-HA
α-FLAG
α-β-actin
H
HA-Ub^WT
FLAG-MEKK3
GFP-Becn1
IP:α-FLAG
IB:α-HA
WCL
IB:α-FLAG
IB:α-GFP
IB:α-β-actin
I
HA-Ub
K6 K11 K27 K29 K33 K48 K63
FLAG-MEKK3
GFP-Becn1
IP:α-FLAG
IB:α-HA
WCL
IB:α-FLAG
IB:α-GFP
IB:α-β-actin
J
HA-MEKK3
WT K69R K79R K174R K273R K299R K397R K435R
FLAG-Becn1
α-HA
α-β-actin
K
Flag-MEKK3 WT K299R
GFP-Becn1
HA-K48-Ub
IP:α-FLAG
IB:α-HA
WCL
IB:α-HA
IB:α-GFP
IB:α-FLAG
IB:α-β-actin

Figure 14. Becn1 ablation suppresses proteasomal degradation of neutrophil MEKK3. (A and B) Screening of Becn1 binding proteins involved in NF-κB and MAPK pathways by immunoprecipitation followed by immunoblot analysis in human embryonic kidney (HEK) 293T cells. WCL, whole cell lysate.(C) 293T cells transfected with 100 ng HA-MEKK3 along with increased amount (0, 100, 250, and 500 ng) of FLAG-Becn1. Cell lysates were subjected to immunoblot analysis. (D) MEKK3 protein expression in Becn1-deficient Neu and pMAC compared to WT controls were analyzed by immunoblotting with anti-MEKK3 and anti-Becn1 antibodies. (E) WT or Becn1-deficient neutrophils were treated with LPS for the indicated time points, followed by immunoblot analysis of MEKK3, TAK1, p-p38, and Becn1 with cell lysates. (F) WT or Becn1-deficient neutrophils were treated with LPS for the indicated time points, followed by immunoblot analysis of p-MKK3/6, MKK3/6 p-p38, and Becn1 with cell lysates. (G) Immunoblot analysis of 293T cells transfected with HA-MEKK3 along with empty vector or FLAG-Becn1 left untreated or treated with proteasome inhibitor MG132 (1 μM) or autophagy inhibitors 3-MA (5 mM) or chloroquine (CQ, 10 μM).(H) 293T cells transfected with FLAG-MEKK3, GFP-Becn1 and HA-Ubiquitin (WT) (Ub^{WT}) expression vectors were lysed and immunoprecipitated with FLAG-beads followed by Immunoblot analysis with indicated antibodies. (I) 293T cells transfected with FLAG-MEKK3, GFP-Becn1 and HA-Ubiquitin mutants (K6, K11, K27, K29, K33, K48, and K63) expression vectors were lysed and immunoprecipitated with FLAG-beads followed by Immunoblot analysis with indicated antibodies. (J) Immunoblot analysis of 293T cells transfected with WT or different mutants of HA-MEKK3 (K69R, K79R, K174R, K273R, K299R, K397R, K435R) along with empty vector or FLAG-Becn1. (K) 293T cells transfected with FLAG-MEKK3 WT or FLAG-MEKK3 K299R mutant along with GFP-Becn1 and HA-Ubiquitin K48 expression vectors were lysed and immunoprecipitated with FLAG-beads followed by Immunoblot analysis with indicated antibodies.

Genetic ablation of p38 or MEKK3 rescues $Becn1^{\Delta M}$ mice phenotypes

To test whether specific deletion of p38 (encoded by *Mapk14*) or MEKK3 (encoded by *Map3k3*) could rescue the phenotypes and survival in response to LPS-induced septic shock of $Becn1^{\Delta M}$ mice, we generated *Mapk14* $^{f/f}$ x *Becn1* $^{f/f}$ x *Lyz2-Cre* double KO ($Becn1^{\Delta M}$ $Mapk14^{\Delta M}$) mice. Gross phenotypic analysis revealed that the spleen size of $Becn1^{\Delta M}$ $Mapk14^{\Delta M}$ mice was reduced to a size comparable to WT spleen (**Figure 15A**). In agreement with these observations, the extent of $CD11b^{+}Gr\text{-}1^{+}$ cells (5.26% in BM, 2.77 in SP) of $Becn1^{\Delta M}$ mice was reduced to a level similar to WT mice (2.32% in BM, 1.17% in SP) in $Becn1^{\Delta M}Mapk14^{\Delta M}$ mice (**Figure 15B**). The serum levels of pro-inflammatory cytokines TNF-α and IL-1β in $Becn1^{\Delta M}$ $Mapk14^{\Delta M}$ mice were reduced to the levels similar to WT control, even though IL-6 production remained at a higher

level in both *Becn1*$^{\Delta M}$ *Mapk14*$^{\Delta M}$ mice and *Becn1*$^{\Delta M}$mice (**Figure 15C**). Importantly, p38 ablation markedly reduced IL-17A production and *Rorc* mRNA level in *Becn1*$^{\Delta M}$ *Mapk14*$^{\Delta M}$ mice (**Figures 15C and 15D**), suggesting that p38 activation in Becn1-deficient neutrophils might control RORγt transcription. Importantly, p38 ablation in *Becn1*$^{\Delta M}$ prolonged the survival to the level similar to WT mice in response to LPS-induced septic shock, but *Becn1*$^{\Delta M}$ *IL-6*$^{-/-}$ double knockout mice failed to do so (**Figures 15E**).

Since mouse *Becn1* and *Map3k3* are localized on the same chromosome (mm11, NC_000077.6), it is difficult to generate *Becn1*$^{\Delta M}$*Map3k3*$^{\Delta M}$ double KO mice. For this reason, we used CRISPR-Cas9 genome editing approach [152, 163] to generate *Becn1*$^{\Delta M}$*Map3k3* ^{cas9} bone marrow chimera by deleting *Map3k3* in bone marrow hematopoietic stem cells (HSC) isolated from WT control or *Becn1*$^{\Delta M}$ mice using *Map3k3*-specific single guide RNA (sgRNA) or control sgRNA. Deletion of *Map3k3* in bone marrow chimera was observed by immunoblot analysis of peripheral blood cell lysates from *Becn1*$^{\Delta M}$*Map3k3*^{cas9} mice, compared to *Becn1*$^{\Delta M}$ and WT bone marrow chimera with control sgRNA (**Figure 15F**). The LPS-induced phosphorylation of P38 in neutrophils isolated from *Becn1*$^{\Delta M}$*Map3k3*^{cas9} mice was significantly reduced (**Figure 15G**), and *Becn1*$^{\Delta M}$ *Map3k3*^{cas9} mice were more resistant to LPS when compared to the *Becn1*$^{\Delta M}$ group (**Figure 15H**). These results indicate that p38 or MEKK3 ablation in neutrophils restores inflammatory cytokine (TNF-α, IL-1β, and IL-17) production and reduces the hypersensitivity to LPS-induced septic shock seen in *Becn1*$^{\Delta M}$ mice.

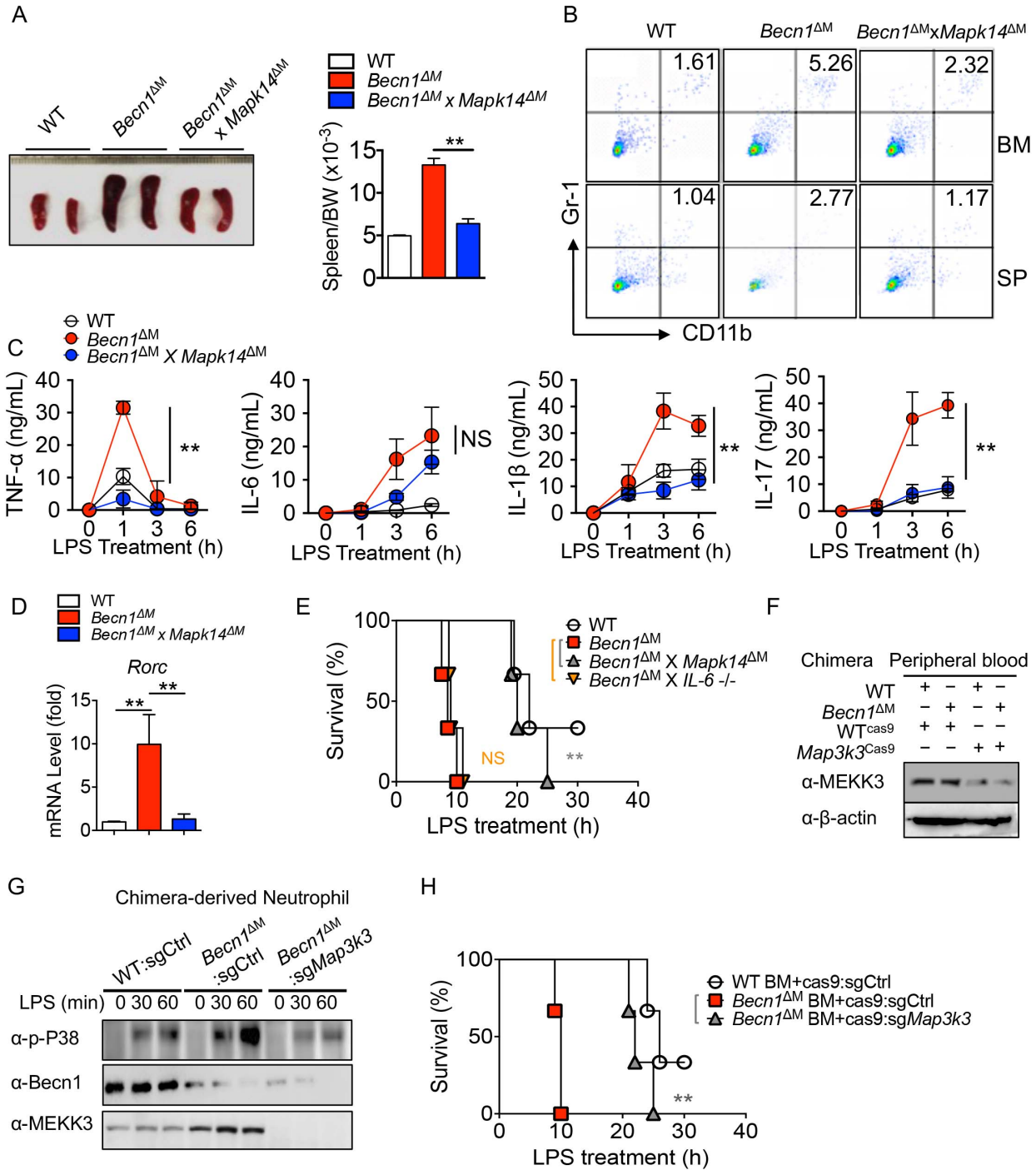
A
WT
Becn1ΔM
Becn1ΔM x Mapk14ΔM
Spleen/BW (x10-3)
B
WT
Becn1ΔM
Becn1ΔMxMapk14ΔM
1.61
5.26
2.32
1.04
2.77
1.17
BM
SP
Gr-1
CD11b
C
Becn1ΔM X Mapk14ΔM
TNF-α (ng/mL)
IL-6 (ng/mL)
IL-1β (ng/mL)
IL-17 (ng/mL)
LPS Treatment (h)
NS
D
Rorc
mRNA Level (fold)
E
Survival (%)
Becn1ΔM X Mapk14ΔM
Becn1ΔM X IL-6 -/-
LPS treatment (h)
F
Chimera
Peripheral blood
WT
Becn1ΔM
WTcas9
Map3k3Cas9
α-MEKK3
α-β-actin
G
Chimera-derived Neutrophil
WT:sgCtrl
Becn1ΔM :sgCtrl
Becn1ΔM :sgMap3k3
LPS (min)
0 30 60
α-p-P38
α-Becn1
α-MEKK3
H
WT BM+cas9:sgCtrl
Becn1ΔM BM+cas9:sgCtrl
Becn1ΔM BM+cas9:sgMap3k3

Figure 15. p38 or MEKK3 ablation rescues *Becn1*$^{\Delta M}$ mice phenotype to WT. (A) Spleen size (left) and spleen : body weight ratio(right) isolated from WT, *Becn1*$^{\Delta M}$ and *Becn1*$^{\Delta M}$ x *Mapk14* $^{\Delta M}$ mice. (B) Gr-1^{+}CD11b^{+} neutrophils in WT, *Becn1*$^{\Delta M}$ and *Becn1*$^{\Delta M}$ x *Mapk14* $^{\Delta M}$ mice were analyzed by flow cytometry. (C) TNF-α, IL-6, IL-1β, and IL-17A production in serum from WT, *Becn1*$^{\Delta M}$, and *Becn1*$^{\Delta M}$ x *Mapk14* $^{\Delta M}$ mice after high dose treatment of LPS (30mg/kg i.p.) were analyzed by ELISA. (D) Neutrophils isolated from WT, *Becn1*$^{\Delta M}$ and *Becn1*$^{\Delta M}$ x *Mapk14* $^{\Delta M}$ mice were treated with LPS for 6h. mRNA level of *Rorc* was determined by quantitative RT-PCR. (E) Survival of WT, *Becn1*$^{\Delta M}$, *Becn1*$^{\Delta M}$ x *Mapk14* $^{\Delta M}$ and *Becn1*$^{\Delta M}$ x *IL-6*$^{-/-}$ mice after high dose treatment of LPS (30mg/kg i.p.). (F) Peripheral blood from WT, *Becn1*$^{\Delta M}$, and *Becn1*$^{\Delta M}$ x *Map3k3* ^{cas9} mice was RBC lysed and followed by immunoblot analysis of MEKK3 expression. (G) Neutrophils isolated from WT, *Becn1*$^{\Delta M}$ and *Becn1*$^{\Delta M}$ x *Map3k3* ^{cas9} mice were treated with LPS for the indicated time points, followed by immunoblot analysis of p-p38 and Becn1 with cell lysates. (H) Survival of WT, *Becn1*$^{\Delta M}$, and *Becn1*$^{\Delta M}$ x *Map3k3* ^{cas9} mice after high dose treatment of LPS (30mg/kg i.p.).Data shown are plotted as the mean ± s.d. and are representative of three independent experiments. $^{**}P$ <0.01, NS (not significant) vs. corresponding control.

Spontaneous development of metastatic Pre-B Cells lymphoma in Becn1$^{\Delta M}$ *mice*

We unexpectedly found exacerbated lymphoproliferation in the cervical lymph nodes in 20-40% of *Becn1*$^{\Delta M}$ mice (**Figures 16A and 16B**). Importantly, we showed positive PAX5 and B220 staining, but negative for monocyte (Mac-3), macrophages (Mac-1), neutrophils (Ly6G), or T cells (CD3) (**Figures 16C and 16D**). Of note, lung infiltrated tumor cells contained mostly PAX5^{+} B220^{+} cells, but also PAX5^{+}B220$^{lo/-}$ populations, suggesting the heterogeneity of tumor (**Figure 16D**). Different from B cell lymphoma in Becn1$^{+/-}$ mice that express BCL6 [143], we found that the lung infiltrated B220^{+} tumor cells were BCL6 negative (**Figure 16E**).

Using CFSE (carboxyfluorescein succinimidyl ester) labeling, we showed that B cells isolated from *Becn1*$^{\Delta M}$ tumor-bearing mice more rapidly proliferated than WT B cells after treatment with LPS and IL-4 (**Figure 16F**). Malignant B cells from *Becn1*$^{\Delta M}$ tumor-bearing mice also displayed a unique phenotype of increased expressions of B cell surface markers, including CD16/32 [FcYRIII/FcYRIIa], activation marker CD80, CD86, and MHC class I (**Figure 16G**). Importantly, we found that elevated percentages of pre-B cells expressing low/intermediate B220 (16.8% in tumor vs. 0.8% in WT LN) and TdT, likely were cells egressed from BM (**Figure 16H-**

J). Sphingosine-1-phosphate receptor (S1P1R) or CXCR4 controls B cell bone marrow egression or retention [164, 165]. We sorted B cells from both WT and *Becn1*$^{\Delta M}$ mice and found a marked reduction of CXCR4 expression but not S1P1R on B cells from *Becn1*$^{\Delta M}$ mice (**Figure 16L**), which might contribute to the pre-B cell BM egression.

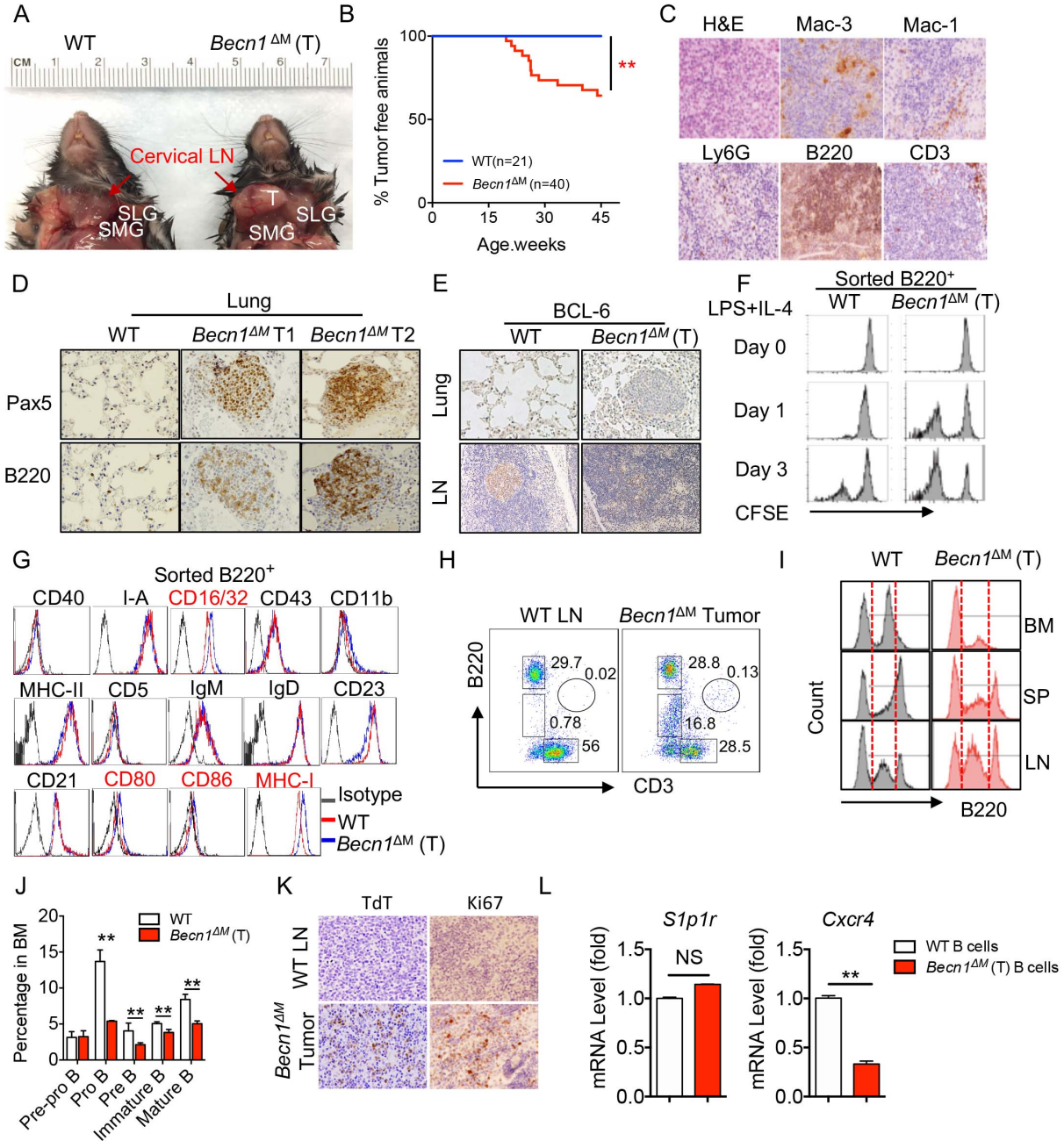

Figure 16. MHC-I^{hi}B220^{lo} B cell lymphoma develops in *Becn1*$^{\Delta M}$ mice. (A) Tumor formation in cervical lymph node (indicated by red arrows) in *Becn1*$^{\Delta M}$ mice compared to WT mice. T, tumor; SLG, sublingual gland; SMG, submandibular gland. (B) Kaplan-Meier curves for tumor-free animals were calculated based on the tumor latency of the control (n=21, blue) and *Becn1*$^{\Delta M}$ mice (n=40, red). (C) Representative immunohistochemical staining of paraffin-embedded tumor sections from *Becn1*$^{\Delta M}$ tumor-bearing mice (n=40) stained with H&E and anti-Mac-3 (monocyte), anti-Mac-1 (macrophage), anti-Ly6G (neutrophils), anti-B220 (B cells) and anti-CD3 (T cells). (D) Immunohistochemical staining of paraffin-embedded tumor-infiltrated lung sections from WT and *Becn1*$^{\Delta M}$ tumor-bearing mice stained with anti-Pax5 and anti-B220 B cell markers. (E) Immunohistochemical staining of paraffin-embedded tumor-infiltrated lung sections from WT and *Becn1*$^{\Delta M}$ tumor-bearing mice stained with anti-BCL6 (lymph nodes as a positive control). (F) Flow cytometric analysis of CFSE-labeled (APC-CFSE) B cells directly sorted from WT and *Becn1*$^{\Delta M}$ tumor-bearing mice by PE-positive selection stained with PE-anti-B220 antibody treated with LPS and IL-4 for indicated time points. (G) Flow cytometric analysis of surface markers of B cells isolated from WT and *Becn1*$^{\Delta M}$ tumor-bearing mice. Significant right-shift markers were indicated in red. (H) Flow cytometric analysis of B220 (B cells), CD3 (T cells) and B220^{+}CD3^{+} (circled) populations in WT control and tumor from *Becn1*$^{\Delta M}$ tumor-bearing mice. (I) Flow cytometric analysis of B220^{+} B cells population in bone marrow (BM), spleen (SP) and lymph node (LN) of WT and *Becn1*$^{\Delta M}$ tumor-bearing mice. (J) Flow cytometric and statistical analysis of pre-pro B (B220^{+}CD43^{+}), pro B (B220^{+}CD43^{lo}), pre-B (B220^{+}CD43^{-}), immature B (B220^{+}CD43^{-}IgM^{+}IgD^{-}) and mature B (B220^{+}CD43^{-}IgM^{+}IgD^{+}) populations in the bone marrow-derived from WT and *Becn1*$^{\Delta M}$ tumor-bearing mice. (K) Immunohistochemical staining of tumor sections with TdT and Ki67 antibodies compared to WT controls. (L) Flow cytometric and statistical analysis of marginal zone (MZ) B (CD93^{-}CD21^{hi}CD23^{lo}), splenic FO B (CD93^{-}CD21^{lo}CD23^{hi}) and B1 B (B220^{+}CD5^{+}) populations in the spleen-derived from WT and *Becn1*$^{\Delta M}$ tumor-bearing mice. (M) Quantitative RT-PCR of *S1p1r* and *Cxcr4* mRNA in B220^{+} cells directly sorted from WT (n=5 per group) and *Becn1*$^{\Delta M}$ tumor-bearing mice (n=9 per group) by PE-positive selection stained with PE-anti-B220 antibody. Data shown are plotted as the mean ± s.d. and are representative of three independent experiments. $^{**}P$ <0.01, NS (not significant) vs. corresponding control.

Accumulating Becn1-deficient neutrophils interact with B cells

We consistently observed the colocalization of B cells with a large number of neutrophils in the tumor site, lungs, and intestinal Peyer's patches (**Figures 17A-D**). To determine the gene expression profiling of the tumor and a potential role of neutrophils in the tumor development, we extracted total RNA from cervical lymph node tumors for RNA-seq. Significantly increased genes in *Becn1*$^{\Delta M}$ mice included inflammatory and B cell-stimulating molecules (Nos2, Ptgs2, Il21, Il1b, Il12, Tnfsf13b, Tnfsf18, Nlrp3), chemoattractants (Cxcl9, Cxcr3), neutrophil marker (Ly6g), key

mediators of apoptotic cell removal (**Figures 17E and 17F**). In addition, key transcriptional factors Ebf1 and Pax5 shown to be essential for the expansion of B-cell progenitors and acute lymphoid leukemia transformation were found to be upregulated [166] (**Figure 17F**). Notably, downregulated cell junction molecules related to leukocyte transendothelial migration (Cdh1, Cldn, Tjp1) (**Figure 17E**) might permit noncanonical interactions between B cells and activated myeloid cells.

Neutrophils have been shown to acquire a B-cell helper phenotype to promote B cell expansion and malignant progression through 1) contact-independent cytokine secretion such as Tnfsf13b and IL-21; 2) contact-dependent mechanisms such as CD40 and neutrophil extracellular traps (NETs) [167-170]. Except for MCL-1 and BCL-2, significant upregulation of B-cell helper signature genes was observed in *Becn1*-deficient neutrophils from tumor-bearing mice (**Figure 17G-I**). Auto-activation of p38 was observed in tumor-derived neutrophils, which might contribute to IL-21 production (**Figures 13 and 17I**). Stained *Becn1*-deficient neutrophils derived from tumor-bearing mice with SYTOX impermeable DNA dye revealed increased projection of NETs (**Figure 17J**). Thus, the recruitment of neutrophils by B cells through Cxcl9/Cxcr3 chemotaxis (**Figures 17E, 17K and 17L**) might provide extensive survival signals and inflammatory environment, leading to B cell malignant transformation.

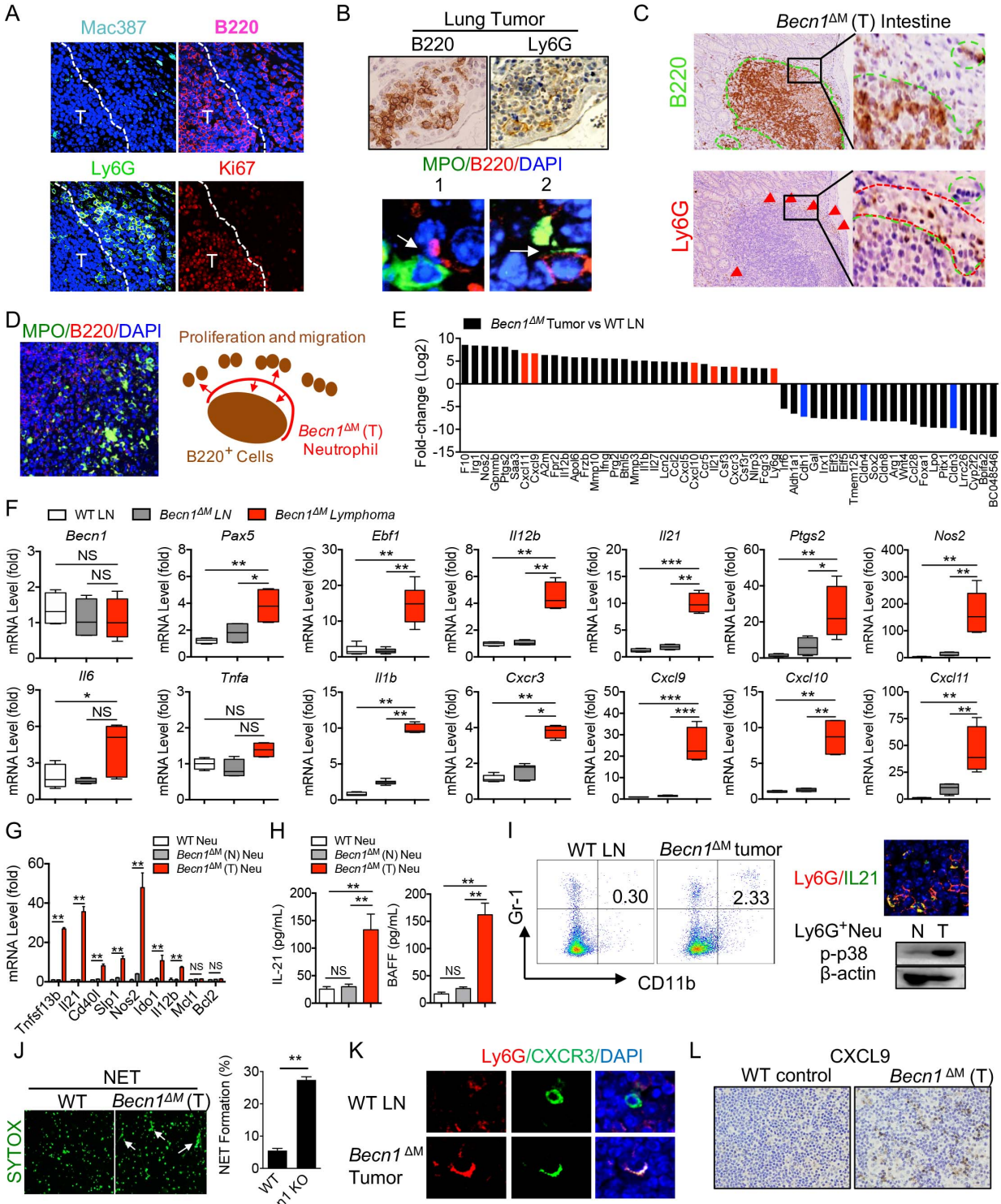
A
Mac387
B220
Ly6G
Ki67
T
B
Lung Tumor
B220
Ly6G
MPO/B220/DAPI
1
2
C
Becn1ΔM (T) Intestine
B220
Ly6G
D
MPO/B220/DAPI
Proliferation and migration
Becn1ΔM (T)
Neutrophil
B220+ Cells
E
Becn1ΔM Tumor vs WT LN
Fold-change (Log2)
F
WT LN
Becn1ΔM LN
Becn1ΔM Lymphoma
Becn1
Pax5
Ebf1
Il12b
Il21
Ptgs2
Nos2
Il6
Tnfa
Il1b
Cxcr3
Cxcl9
Cxcl10
Cxcl11
mRNA Level (fold)
NS
G
WT Neu
Becn1ΔM (N) Neu
Becn1ΔM (T) Neu
mRNA Level (fold)
Tnfsf13b
Il21
Cd40l
Slp1
Nos2
Ido1
Il12b
Mcl1
Bcl2
H
WT Neu
Becn1ΔM (N) Neu
Becn1ΔM (T) Neu
IL-21 (pg/mL)
BAFF (pg/mL)
I
WT LN
Becn1ΔM tumor
0.30
2.33
Gr-1
CD11b
Ly6G/IL21
Ly6G+Neu
N T
p-p38
β-actin
J
NET
WT
Becn1ΔM (T)
SYTOX
NET Formation (%)
WT
Becn1 KO
K
Ly6G/CXCR3/DAPI
WT LN
Becn1 ΔM
Tumor
L
CXCL9
WT control
Becn1 ΔM (T)

Figure 17. Becn1 ablation induces B cell helper function of neutrophils. (A) Immunofluorescence of tumor section with anti-mac387 (macrophages, cyan), anti-B220 (B cells, pink), anti-Ly6G (neutrophils, green), DAPI (nucleus, blue) and anti-Ki67 (proliferation marker, red). White line circled area indicates B cell tumor. Original magnification, x40. (B) Immunohistochemical staining (B, upper) and two representative immunofluorescent confocal images (B, bottom) of paraffin-embedded tumor-infiltrated lung sections from *Becn1*$^{\Delta M}$ tumor-bearing mice stained with anti-B220 and anti-LY6G (B, upper) or and with anti-MPO (green) and anti-B220 (red) antibodies ((B, bottom) showing the interaction of B cells and neutrophils. DAPI, DNA-intercalating dye indicates nucleus (blue). (C) Immunohistochemical staining of paraffin-embedded intestinal Peyer's patch sections from *Becn1*$^{\Delta M}$ tumor-bearing mice stained with anti-B220 (C, upper) and anti-Ly6G (C, lower). (D) Representative immunofluorescent staining of tumor section with indicated antibodies (D, left) and cartoon illustrates neutrophils surround at the edge of B cell zone likely to support B cell proliferation and migration (D, bottom cartoon). (E) Log2 ratio of mRNA variations in the tumor from *Becn1*$^{\Delta M}$ mice compared to WT controls by RNA-seq.(F) Quantitative RT-PCR for analysis of the mRNA levels of the indicated genes in WT lymph nodes, *Becn1*$^{\Delta M}$ lymph nodes (no tumor), and *Becn1*$^{\Delta M}$ lymphomas (n=4 per group).(G) Quantitative RT-PCR of B cell helper neutrophils markers: BAFF (Tnfsf13b), Il21, Cd40l, Slp1, Nos2, Ido1, Mcl-1, and Bcl-2. (H) BAFF (encoded by Tnfsf13b) and IL-21 production by neutrophils directly isolated from WT and *Becn1*$^{\Delta M}$ tumor-bearing mice were analyzed by ELISA after in vitro culture for 12h.(I) Flow cytometric analysis and Immunofluorescent staining showed accumulation of Gr-1^{+}CD11b^{+} neutrophils in the tumor (I, left) expressing IL-21 (I, upper right). Immunoblot analysis showed p38 MAPK auto-activation in neutrophils from *Becn1*$^{\Delta M}$ tumor-bearing mice (I, lower right). (J) Fluorescent microscopy (*left*) and statistical (*right*) analysis of NETs formation in WT and Becn1-deficient neutrophils by using SYTOX impermeable nuclear dye (green). White arrows (Original magnification, x40) indicate NETs. (K) Immunofluorescence of tumor section with anti-Ly6G (red), CXCR3 (green), and DAPI (blue) from *Becn1*$^{\Delta M}$ tumor-bearing mice compared to WT controls showing colocalization of Ly6G and CXCR3 in tumor but not WT control LN.(L) Immunohistochemical staining of tumor sections *Becn1*$^{\Delta M}$ tumor-bearing mice with anti-CXCL9 antibody compared to WT control LN. Data shown are plotted as the mean ± s.d. and are representative of three independent experiments. **P* <0.05, ***P* <0.01, ****P* <0.001, NS (not significant) vs. corresponding control.

Neutrophil loss of Becn1 transforms pre-B cells through prosurvival pathways correlating with human pre-B ALL

To determine how the neutrophil loss of Becn1 contributes to the malignancy of B cells, RNA-seq was performed using freshly isolated total B cells from WT and *Becn1*$^{\Delta M}$ tumor-bearing mice. Significant upregulation of genes included: 1) STAT target genes such as *Cxcl9*, *Socs1*, *Socs3, Irf1* and *Cd274 (PD-L1)*; 2) precursor B (pre-B) cell markers such as IL2ra and Ly6a [171]; 3) B cell activation markers such as IL10 and Saa3; 4) MHC class I related molecules such as Nlrc5 and Psmb9; and 5) the innate immunity gene Mb21d1 (cGAS) (**Figures 18A and 18B**).

We next sought to examine whether tumor cells had altered oncogenic signalings [147, 172]. The tumor cells and control cells were sorted by B220^{+} selection followed by immediately lysed or anti-CD40 agonist stimulation. We observed increased activation of ERK and JNK, elevated activation of signaling downstream of IL-21 (STAT1, STAT3, STAT5) and BAFF (non-canonical NF-κB p52), as well as upregulated STAT5-target (anti-apoptotic gene MCL-1) [173] (**Figures 18C and 18D**). Moreover, we compared signaling activations in B cells from WT, tumor-free *Becn1*$^{\Delta M}$ (NT), and B220^{hi} vs. B220^{lo} cells from tumor-bearing *Becn1*$^{\Delta M}$ mice. We found B220^{lo} cells showed a higher level of phosphorylated STAT1/3/5 and PD-L1 than B220^{hi} cells (**Figures 18D and 18E**). By co-culturing neutrophils or macrophages from tumor-bearing *Becn1*$^{\Delta M}$ mice with normal WT B cells, we confirmed the induction of p-STAT3 and PD-L1 in B cells by neutrophil-derived IL-21 (**Figure 18F**) and could be abolished by either IL-21 antibody blockade and p38 ablation (**Figures 18G-I**). In **Figures 13 and 15**, we showed p38 signaling regulated neutrophil inflammation in *Becn1*$^{\Delta M}$ mice in response to TLR ligand stimulation, which was auto-activated in tumor-derived neutrophil (**Figure 17I**). We next examined if ablation of p38 reduce

the risk of B cell lymphoma in *Becn1*$^{\Delta M}$ mice. Indeed, myeloid loss of p38 suppressed tumor formation in *Becn1*$^{\Delta M}$ mice (**Figure 18J**).

To investigate whether Becn1 in human neutrophils play a role in human B-cell lymphoid malignancies, we first analyzed Becn1 expression in a series of human B-cell non-Hodgkin lymphomas (B-NHL) and pre- B cell acute lymphoblastic leukemia/lymphoma (ALL) by human gene expression profiling (GEP). Becn1 expression varied among the different B-cell lymphoid malignancies, with significantly lowest in pre-B ALL and highest in MCL and CLL (**Figure 18K**). We further detected Becn1 expression in neutrophils in 8 human pre-B ALL patients, and we found low Becn1 expression in neutrophils compared to reactive lymph node controls (**Figures 18L and 18M**). Notably, in recurrent pre-B ALL patient, Becn1 low neutrophils had the NET-like structure (**Figure 18L**). Consistent with the upregulation of PD-L1 in B cells in *Becn1*$^{\Delta M}$ mice, we found upregulation of PD-L1 in pre-B ALL patient BM and LN samples especially in recurrent pre-B ALL samples (**Figure 18N**). These data suggest defective Becn1 in neutrophils might have a direct link to the PD-L1 levels and recurrence in human pre-B ALL. To apply our findings and to examine the tumor immunity in mouse model of melanoma, we injected intravenously the B16 melanoma cells. In *Becn1*$^{\Delta M}$ mice, we observed dramatic increase in melanoma cell metastasis in the liver but slightly increase in the lung (**Figure 18O**). Interestingly, we found infiltrations of neutrophils with NET structure and PAX5 positive B cells in metastases accompany by reduced number of T cells (**Figures 18P**). Thus, our results suggest that the accumulation of neutrophils and PD-L1^{+} B cells in liver might establish niches for melanoma metastasis and potentially suppress anti-tumor immunity through immune checkpoint inhibition.

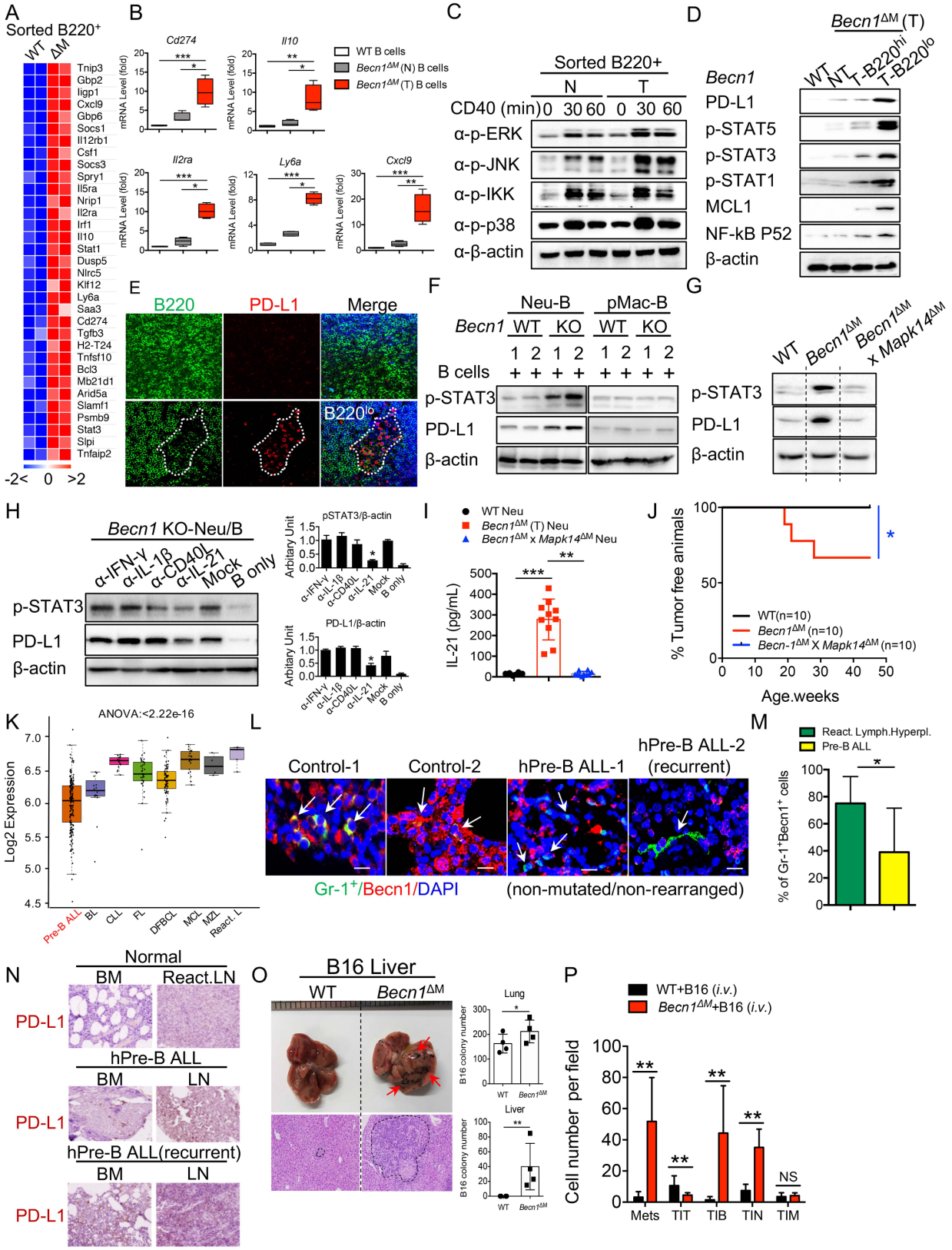
A
Sorted B220+
WT
ΔM
Tnip3
Gbp2
Iigp1
Cxcl9
Gbp6
Socs1
Il12rb1
Csf1
Socs3
Spry1
Il5ra
Nrip1
Il2ra
Irf1
Il10
Stat1
Dusp5
Nlrc5
Klf12
Ly6a
Saa3
Cd274
Tgfb3
H2-T24
Tnfsf10
Bcl3
Mb21d1
Arid5a
Slamf1
Psmb9
Stat3
Slpi
Tnfaip2
-2< 0 >2
B
Cd274
Il10
Il2ra
Ly6a
Cxcl9
mRNA Level (fold)
WT B cells
Becn1ΔM (N) B cells
Becn1ΔM (T) B cells
C
Sorted B220+
N
T
CD40 (min) 0 30 60 0 30 60
α-p-ERK
α-p-JNK
α-p-IKK
α-p-p38
α-β-actin
D
Becn1ΔM (T)
WT
NT
T-B220hi
T-B220lo
Becn1
PD-L1
p-STAT5
p-STAT3
p-STAT1
MCL1
NF-kB P52
β-actin
E
B220
PD-L1
Merge
B220lo
F
Neu-B
pMac-B
Becn1 WT KO WT KO
1 2 1 2 1 2 1 2
B cells + + + + + + + +
p-STAT3
PD-L1
β-actin
G
WT
Becn1ΔM
Becn1ΔM x Mapk14ΔM
p-STAT3
PD-L1
β-actin
H
Becn1 KO-Neu/B
α-IFN-γ
α-IL-1β
α-CD40L
α-IL-21
Mock
B only
p-STAT3
PD-L1
β-actin
pSTAT3/β-actin
PD-L1/β-actin
Arbitary Unit
I
WT Neu
Becn1ΔM (T) Neu
Becn1ΔM x Mapk14ΔM Neu
IL-21 (pg/mL)
J
% Tumor free animals
WT(n=10)
Becn1ΔM (n=10)
Becn-1ΔM X Mapk14ΔM (n=10)
Age.weeks
K
ANOVA:<2.22e-16
Log2 Expression
Pre-B ALL
BL
CLL
FL
DFBCL
MCL
MZL
React. L
L
Control-1
Control-2
hPre-B ALL-1
hPre-B ALL-2 (recurrent)
Gr-1+/Becn1/DAPI
(non-mutated/non-rearranged)
M
React. Lymph.Hyperpl.
Pre-B ALL
% of Gr-1+Becn1+ cells
N
Normal
BM
React.LN
PD-L1
hPre-B ALL
BM
LN
PD-L1
hPre-B ALL(recurrent)
BM
LN
PD-L1
O
B16 Liver
WT
Becn1ΔM
Lung
Liver
B16 colony number
P
WT+B16 (i.v.)
Becn1ΔM+B16 (i.v.)
Cell number per field
Mets
TIT
TIB
TIN
TIM
NS

Figure 18. Neutrophil inflammation favors the malignancy of PD-L1$^+$ pre-B cells. (A) Heatmap representation of genes significantly upregulated in B cells isolated from *Becn1*$^{\Delta M}$ tumor-bearing mice compared to WT controls by RNA-seq. (B) Quantitative RT-PCR for analysis of the mRNA levels of the indicated genes in B cells from WT, *Becn1*$^{\Delta M}$ (N, no tumor), and *Becn1*$^{\Delta M}$ (T, tumor-bearing) mice (n=4 per group). (C) Immunoblot analysis of phosphorylation of ERK, JNK, IKK and p38 in total B220$^+$ cells isolated from WT control and from *Becn1*$^{\Delta M}$ tumor-bearing mice stimulated with anti-CD40 agonist for indicated time points. (D) Immunoblot analysis of PD-L1, p-STAT1, p-STAT3, p-STAT5, MCL-1 and p52 in B cells isolated from WT control, *Becn1*$^{\Delta M}$ mice without palpable tumor (NT) and *Becn1*$^{\Delta M}$ tumor-bearing mice (T-B220^{hi} vs. T-B220^{lo} cells). (E) Immunofluorescent staining of tumor sections with PD-L1 (red) and B220 (green) antibodies compared to WT controls, showing upregulation of PD-L1 in B220^{lo} cells (dark green) compared to B220^{hi} cells (bright green). (F) Neu or pMAC isolated from WT or *Becn1*$^{\Delta M}$ tumor-bearing mice were co-cultured with WT B cells. After co-culture for 24h, B cells were purified and lysed for immunoblot analysis with indicated antibody. Two representative samples were shown. (G) B cells isolated from WT, *Becn1*$^{\Delta M}$ tumor-bearing mice, and *Becn1*$^{\Delta M}$ x *Mapk14* $^{\Delta M}$ mice were purified and lysed for immunoblot analysis with indicated antibody. (H) Neutrophils isolated from WT or *Becn1*$^{\Delta M}$ tumor-bearing mice were co-cultured with WT B cells (Neu/B co-culture) together with Mock antibody treatment, anti-IFN-γ, anti-IL-1β, anti-CD40L, anti-IL-21, or B cells without neutrophils (B only). After co-culture for 24h, B cells were purified and lysed for immunoblot analysis with indicated antibody. Quantitative comparisons of pSTAT3 and PD-L1 level were analyzed by densitometric scanning of blots and normalized to β-actin (right). (I) ELISA assay of the IL-21 production in neutrophils from WT, *Becn1*$^{\Delta M}$ tumor-bearing mice, and *Becn1*$^{\Delta M}$ x *Mapk14* $^{\Delta M}$ mice. n=10. (J) Kaplan-Meier curves for tumor-free animals were calculated based on the tumor latency of the WT (n=10, black), *Becn1*$^{\Delta M}$ mice (n=10, red) and *Becn1*$^{\Delta M}$ x *Mapk14* $^{\Delta M}$ (n=10, blue) mice. (K) Human Becn1 gene expression profile (GEP) in patients with pre- B cell acute lymphoblastic leukemia (pre-B ALL, without mutations or gene rearrangements) or various non-Hodgkin's B cell (NHB) lymphoma compared to reactive lymph node controls. The boxes show the median±1 quartile, with whiskers extending to the most extreme data point within 1.5 interquartile range from the box boundaries. (L) Becn1 expression analysis by IF staining in human neutrophils in human normal reactive lymph node controls and pre-B-ALL patient samples including patient with recurrence of pre-B-ALL (no genomic mutation or gene rearrangement). (M) Quantification of Gr-1$^+$ Becn1-expressign cells in reactive lymphoid hyperplasia and pre-B ALL patient samples (n=6). (N) Immunoblot analysis of PD-L1 expression in pre-ALL patient BM and LN samples compared to normal controls. (O) Liver metastasis of melanoma in WT and *Becn1*$^{\Delta M}$ mice *i.v.* injected with 2x10^5 cells per mouse of B16 cells. (P) Cell number counting per tumor-field and statistical analysis of B16 liver metastases, infiltrated CD3$^+$ T cells (TIT), PAX5$^+$ B cells (TIB), Gr1$^+$ Neutrophils (TIN), and F4/80$^+$ (TIM) in B16 melanoma-bearing WT and *Becn1*$^{\Delta M}$ mice (n=10).

Discussion

Despite numerous *in vitro* studies emphasizing a role for autophagy in macrophages during *Mycobacterium tuberculosis* infection or LC3-associated phagocytosis [89, 174], little is known about the function of Becn1 in neutrophils in inflammation and cancer *in vivo*. We have demonstrated that deletion of Becn1 in the myeloid lineage leads to neutrophilia, which causes splenomegaly and lymphadenopathy in mice. We uncovered a cell-type specific mechanism of Becn1 in the negative regulation of neutrophil p38 signaling in response to LPS. Depletion of neutrophils but not macrophages rescued the sensitivity of *Becn1*$^{\Delta M}$ mice to LPS endotoxin shock, suggesting an excessive LPS-induced neutrophil inflammation. Our cytokine profiling and RNA-seq results further revealed the enhanced productions of TNF-α, IL-1β, ROS, IL-17-related cytokine, and chemokine-receptor Cxcr3 by neutrophils in *Becn1*$^{\Delta M}$ mice. p38 MAPK signaling is critical for the transcription and production of inflammatory cytokines [175-177]. Consistent with the cell depletion results, we have provided compelling genetic evidence that p38 (encoded by *Mapk14*) ablation in myeloid cells rescues the observed phenotypes and the production of inflammatory cytokines in *Becn1*$^{\Delta M}$ mice. Although we have found an elevated production of IL-6 by macrophages, IL-6 ablation failed to rescue the survival of *Becn1*$^{\Delta M}$ mice to LPS.

It is known that MAP3Ks (TAK1, ASK1, MEKK3) activation triggers downstream signaling of IKK complex, Erk1/2, p38, and JNK [34]. We show that Becn1 interacts with MEKK3 and MKK3 and promotes MEKK3 K48 ubiquitination at lysine 299 and subsequently proteasomal degradation independent of autophagy. Due to the low protein level of MEKK3 observed in neutrophils, stabilization of MEKK3 upon Becn1 deletion leads to aberrant activation of MEKK3-MKK3-p38 signaling axis in neutrophils. Further ablation of MEKK3 has significantly prolonged the survival of *Becn1*$^{\Delta M}$ mice to LPS.

Heterozygous deletion of Becn1 in mice increases the incidence of spontaneous tumors including diffused large cell b-cell lymphoma (DLBCL) [142, 143], suggesting that Becn1 is a haploinsufficent tumor suppressor. However, it is unclear whether the tumor formation is contributed by intrinsic factors or transformed by oncogenic inflammation induced by non-transformed immune cells in the tumor microenvironment. In *Becn1*$^{\Delta M}$ mice, we unexpectedly found immature Pax5^{+}TdT^{+}B220$^{lo\text{-}int}$ pre-B cell infiltrating into major organ tissues and high risk of pre-B cell lymphoma formation at the early age of 15-25 weeks. Becn1-deleted neutrophils, but not macrophages, were constantly found to colocalize and interact with B cells in secondary lymphoid tissues and other infiltrated organ tissues. Stromal cells, Bruton's tyrosine kinase, S1P/S1P receptor, CXCL12/CXCR4 signaling cascades, and α4β1-VCAM-1-mediated adhesion regulate B cell migration from bone marrow [170, 178-181]. Downregulation CXCR4 and cell-cell adhesion molecules such as claudins in the tumor may favor the B cell migration and neutrophil-B cell interaction.

Recent studies identify a unique population of IL-21 secreting neutrophils termed B cell helper neutrophils to sustain B cell survival, expansion and malignant transformation [167, 168, 170]. However, mechanisms underlying the differentiation and transition of neutrophils to gain "B cell helper" function is unknown. Notably, neutrophils isolated from *Becn1*$^{\Delta M}$ tumor-bearing mice were p38 auto-activated and showed upregulated "B helper" signatures including IL-21, BAFF, CD40L, and production of NET. These factors have been shown to activate multiple oncogenic signaling, including STAT and non-canonical NF-kB known to be crucial in initiating oncogene transcription and establishing the tumor pre-metastatic niche [148, 172, 182-184]. Intriguingly, our RNA-seq and qPCR results confirmed the expression of pre-B cell marker Il2ra and Ly6a, PD-L1, and Irf1, an essential transcription factor mediated STAT signaling and the expression of both

PD-L1 and MHC-I molecules [69, 185, 186]. Strikingly, when comparing $B220^{lo}$ with $B220^{hi}$ cell populations, we observed specifically in $B220^{lo}$ cells the persistent activation of STAT1, STAT3, STAT5, and non-canonical NF-κB p52, followed by upregulation of their downstream targets MCL-1, chemokine Cxcl9, and checkpoint inhibitor PD-L1. Importantly, we have further unraveled a positive feedback recruitment of neutrophils by pre-B cells through the Cxcl9-Cxcr3 chemotaxis to promote malignant transformation of pre-B cells (**Figure 19**).

Based on our findings in mice, we also found downregulation of Becn1 in pre-B ALL patients without gene mutations and gene rearrangements. Becn1 low expression in neutrophils correlates with PD-L1 levels and cancer recurrence in patients with pre-B ALL, which recapitulated the malignant pre-B cells identified in *Becn1*$^{\Delta M}$ mice. PD-L1 is one of the most essential checkpoint inhibitory mechanisms utilized by tumor cells or other immune suppressor cells to suppress T cell function for immune evasion [67-69, 187]. Recent studies of the PD-L1-expressing IgA^+ B cells have been shown to suppress $CD8^+$ T cells killing of liver tumor in mouse model of inflammation-induced liver cancer [71]. By utilizing a mouse model of B16 metastatic melanoma, we found dramatic increase of liver metastasis of B16 melanoma cells, accompanied with the enrichment of tumor-associated neutrophils and B cells. Together these data demonstrate a tumor suppressor role of myeloid Becn1 in pre-B tumor progression and provide evidence to support possible roles of tumor-associated neutrophils and B cells in melanoma metastasis. Neutrophil Becn1 inhibition might sensitive the metastatic and/or recurrent pre-B ALL to PD-L1 antibody blockade therapy.

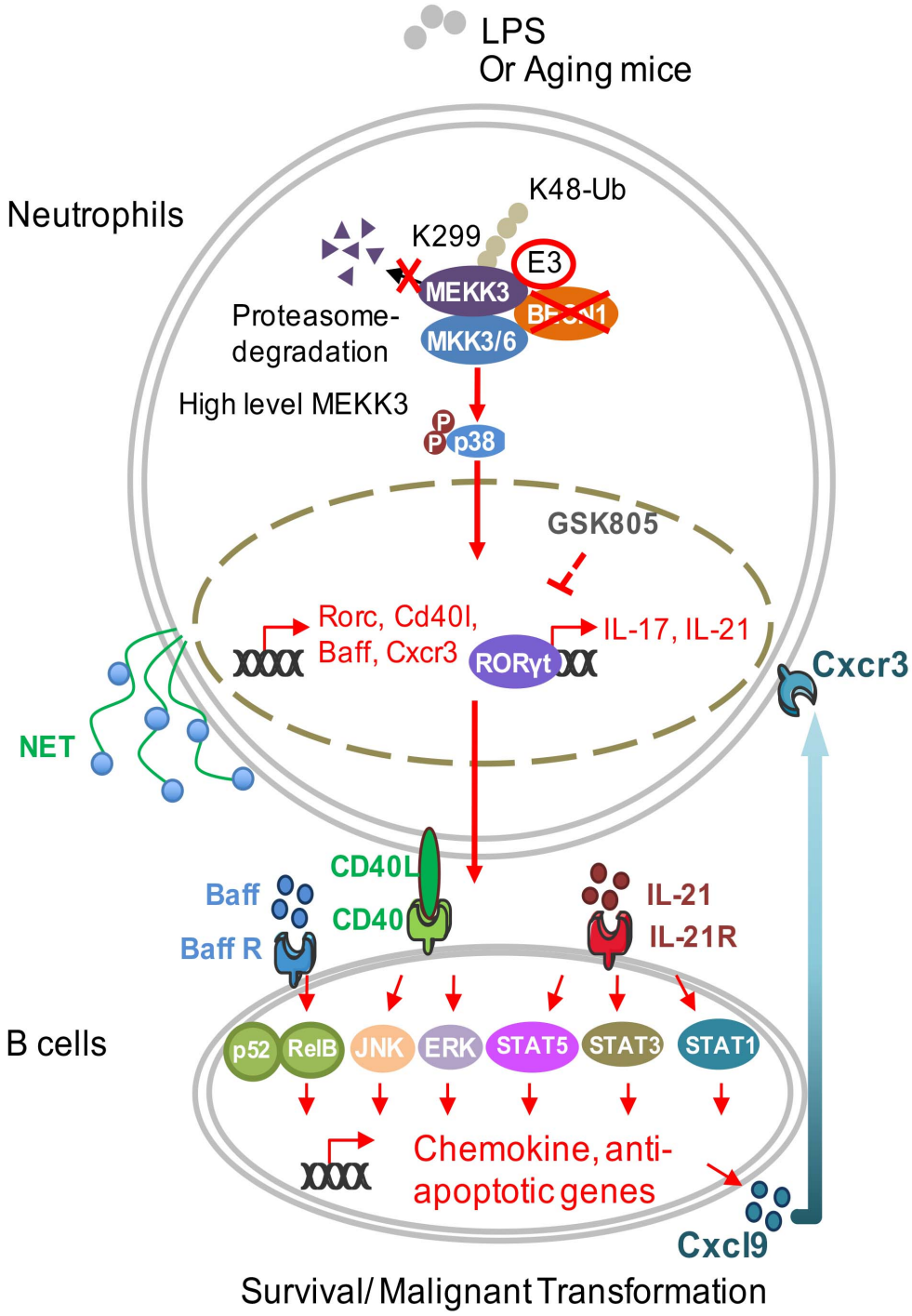

Figure 19. Schematic diagram illustrates neutrophil Becn1 in pre-B cell malignancy. Cartoon indicates Becn1-deficient neutrophils gain the B cell helper function: enhanced expression of CD40L, secretion of pro-survival factors IL-21, BAFF, and NET. The interaction of Becn1-deficient neutrophils and B cells through CXCL9-CXCR3 chemotaxis, leading to the activations of STAT1/3/5, ERK, JNK, and non-canonical NF-κB pathways and malignancy of pre-B cells.

CHAPTER IV

CONCLUSIONS

Mankind has evolved to combat viruses by developing a robust and tightly controlled viral sensing system. By coupling APEX-proteomic mapping and yeast-two hybrid screening, we identified a previously unrecognized mitochondrial WHIP-TRIM14-PPP6C signalosome. WHIP is the key mediator coupling the RIG-I sensor to the mitochondrial TRIM14 signalosome allowing RIG-I translocation to mitochondria where RIG-I and MAVS interact. PPP6C, on the other hand, maintains the dephosphorylation status of RIG-I leading to optimal activation of the antiviral type I IFN response. PPP6C is one of the hotspot mutations in melanoma. Our study of PPP6C in the regulation of IFN signaling might provide immunotherapeutic insight into the treatment of melanoma patients. In this study, we reveal a dual role of TRIM14 in mediating both viral DNA and RNA sensing pathways through distinct mechanisms as in our previously reported that TRIM14 stabilizes cGAS through recruitment of USP14 for K48 deubiquitination. Our study also raises a possibility that viruses such as West Nile virus, dengue virus, or influenza virus manipulate the TRIM14 signalosome to benefit their replication as viral evasion strategy. The WHIP-TRIM14-PPP6C might also be a potential therapeutic target for efficacious antiviral drug development.

Most of the studies of Becn-1 so far are done in heterozygous mice due to embryonic lethality of Becn-1 general knockout in mice. For this particular shortcoming, the specific roles of Becn-1 in terminally differentiated cells and the underlying mechanisms that contribute to the tumorigenesis or tumor-suppression are not well defined. Our characterization of myeloid beclin1 in genetic mouse model gains an overall picture of how innate immune system interplays with

adaptive immunity. Combining a new myeloid-specific deletion of Becn-1 mouse model and next-generation sequencing, we understand how the status of Becn-1 in innate immune cells contributes to tumorigenesis and provide a clear explanation on the intense discussion of the contradicted role of autophagy proteins in cancer progression. Our study suggests a correlation between low expression of myeloid Beclin1 and the risk of human pre-B ALL, hinting the use of pharmacological inhibitors of autophagy in the treatment of cancer especially those targeting Beclin1 might have a potential risk of causing chronic inflammation and lymphoid malignant transformation. On the other hand, upregulation of PD-L1 expression on B cells resulting from myeloid Beclin1 ablation might inhibit the cytotoxic function of antitumor $CD8^+$ T cells in tumor microenvironment through checkpoint inhibition. In such case, PD-L1 antibody blockade might induce tumor regression. Our study provides a mechanism for better therapeutic drug development that not only cures cancer but also prevents the cause of chronic inflammation that may potentially fuel the cancer recurrence in patients exposed to long-term treatment. The study of tumor microenvironmental Beclin1 such that in MDSCs also contributes to the mechanism of how tumor cells escape from checkpoint blockade immunotherapy, which is critical for enhancing the efficacy of combination immunotherapy.

REFERENCES

1. Thaiss, C.A., et al., *Integration of Innate Immune Signaling.* Trends Immunol, 2016. **37**(2): p. 84-101.

2. Zevini, A., D. Olagnier, and J. Hiscott, *Crosstalk between Cytoplasmic RIG-I and STING Sensing Pathways.* Trends Immunol, 2017. **38**(3): p. 194-205.

3. Chan, Y.K. and M.U. Gack, *Viral evasion of intracellular DNA and RNA sensing.* Nat Rev Microbiol, 2016. **14**(6): p. 360-73.

4. Schreiber, R.D., L.J. Old, and M.J. Smyth, *Cancer immunoediting: integrating immunity's roles in cancer suppression and promotion.* Science, 2011. **331**(6024): p. 1565-70.

5. Bruns, A.M. and C.M. Horvath, *LGP2 synergy with MDA5 in RLR-mediated RNA recognition and antiviral signaling.* Cytokine, 2015. **74**(2): p. 198-206.

6. Kato, H., et al., *Length-dependent recognition of double-stranded ribonucleic acids by retinoic acid-inducible gene-I and melanoma differentiation-associated gene 5.* J Exp Med, 2008. **205**(7): p. 1601-10.

7. Maharaj, N.P., et al., *Conventional protein kinase C-alpha (PKC-alpha) and PKC-beta negatively regulate RIG-I antiviral signal transduction.* J Virol, 2012. **86**(3): p. 1358-71.

8. Wies, E., et al., *Dephosphorylation of the RNA sensors RIG-I and MDA5 by the phosphatase PP1 is essential for innate immune signaling.* Immunity, 2013. **38**(3): p. 437-49.

9. Jiang, X., et al., *Ubiquitin-induced oligomerization of the RNA sensors RIG-I and MDA5 activates antiviral innate immune response.* Immunity, 2012. **36**(6): p. 959-73.

10. Okamoto, M., et al., *Regulation of RIG-I Activation by K63-Linked Polyubiquitination.* Front Immunol, 2017. **8**: p. 1942.

11. Liu, S., et al., *Phosphorylation of innate immune adaptor proteins MAVS, STING, and TRIF induces IRF3 activation.* Science, 2015. **347**(6227): p. aaa2630.

12. Schneider, W.M., M.D. Chevillotte, and C.M. Rice, *Interferon-stimulated genes: a complex web of host defenses.* Annu Rev Immunol, 2014. **32**: p. 513-45.

13. Tsuchida, T., et al., *The ubiquitin ligase TRIM56 regulates innate immune responses to intracellular double-stranded DNA.* Immunity, 2010. **33**(5): p. 765-76.

14. Chen, Q., L. Sun, and Z.J. Chen, *Regulation and function of the cGAS-STING pathway of cytosolic DNA sensing.* Nat Immunol, 2016. **17**(10): p. 1142-9.

15. Wang, Y., et al., *Inflammasome Activation Triggers Caspase-1-Mediated Cleavage of cGAS to Regulate Responses to DNA Virus Infection.* Immunity, 2017. **46**(3): p. 393-404.

16. Hu, M.M., et al., *Sumoylation Promotes the Stability of the DNA Sensor cGAS and the Adaptor STING to Regulate the Kinetics of Response to DNA Virus.* Immunity, 2016. **45**(3): p. 555-569.

17. Chen, M., et al., *TRIM14 Inhibits cGAS Degradation Mediated by Selective Autophagy Receptor p62 to Promote Innate Immune Responses.* Mol Cell, 2016. **64**(1): p. 105-119.

18. Shi, H., et al., *NLRP3 activation and mitosis are mutually exclusive events coordinated by NEK7, a new inflammasome component.* Nat Immunol, 2016. **17**(3): p. 250-8.

19. He, Y., et al., *NEK7 is an essential mediator of NLRP3 activation downstream of potassium efflux.* Nature, 2016. **530**(7590): p. 354-7.

20. Yu, J., et al., *Inflammasome activation leads to Caspase-1-dependent mitochondrial damage and block of mitophagy.* Proc Natl Acad Sci U S A, 2014. **111**(43): p. 15514-9.

21. Zhong, Z., et al., *NF-kappaB Restricts Inflammasome Activation via Elimination of Damaged Mitochondria.* Cell, 2016. **164**(5): p. 896-910.

22. Marchi, S., S. Patergnani, and P. Pinton, *The endoplasmic reticulum-mitochondria connection: one touch, multiple functions.* Biochim Biophys Acta, 2014. **1837**(4): p. 461-9.

23. Seth, R.B., et al., *Identification and characterization of MAVS, a mitochondrial antiviral signaling protein that activates NF-kappaB and IRF 3.* Cell, 2005. **122**(5): p. 669-82.

24. Odendall, C., et al., *Diverse intracellular pathogens activate type III interferon expression from peroxisomes.* Nat Immunol, 2014. **15**(8): p. 717-26.

25. Li, X.D., et al., *Mitochondrial antiviral signaling protein (MAVS) monitors commensal bacteria and induces an immune response that prevents experimental colitis.* Proc Natl Acad Sci U S A, 2011. **108**(42): p. 17390-5.

26. West, A.P., G.S. Shadel, and S. Ghosh, *Mitochondria in innate immune responses.* Nat Rev Immunol, 2011. **11**(6): p. 389-402.

27. Castanier, C., et al., *Mitochondrial dynamics regulate the RIG-I-like receptor antiviral pathway.* EMBO Rep, 2010. **11**(2): p. 133-8.

28. Subramanian, N., et al., *The adaptor MAVS promotes NLRP3 mitochondrial localization and inflammasome activation.* Cell, 2013. **153**(2): p. 348-61.

29. Wang, X., et al., *RNA viruses promote activation of the NLRP3 inflammasome through a RIP1-RIP3-DRP1 signaling pathway.* Nat Immunol, 2014. **15**(12): p. 1126-33.

30. Thimmulappa, R.K., et al., *Nrf2 is a critical regulator of the innate immune response and survival during experimental sepsis.* J Clin Invest, 2006. **116**(4): p. 984-95.

31. Todoric, J., et al., *Stress-Activated NRF2-MDM2 Cascade Controls Neoplastic Progression in Pancreas.* Cancer Cell, 2017. **32**(6): p. 824-839 e8.

32. Umemura, A., et al., *p62, Upregulated during Preneoplasia, Induces Hepatocellular Carcinogenesis by Maintaining Survival of Stressed HCC-Initiating Cells.* Cancer Cell, 2016. **29**(6): p. 935-948.

33. Kayagaki, N., et al., *Noncanonical inflammasome activation by intracellular LPS independent of TLR4.* Science, 2013. **341**(6151): p. 1246-9.

34. Arthur, J.S. and S.C. Ley, *Mitogen-activated protein kinases in innate immunity.* Nat Rev Immunol, 2013. **13**(9): p. 679-92.

35. Ajibade, A.A., H.Y. Wang, and R.F. Wang, *Cell type-specific function of TAK1 in innate immune signaling.* Trends Immunol, 2013. **34**(7): p. 307-16.

36. Salmon, H., et al., *Expansion and Activation of CD103(+) Dendritic Cell Progenitors at the Tumor Site Enhances Tumor Responses to Therapeutic PD-L1 and BRAF Inhibition.* Immunity, 2016. **44**(4): p. 924-38.

37. Spranger, S., et al., *Tumor-Residing Batf3 Dendritic Cells Are Required for Effector T Cell Trafficking and Adoptive T Cell Therapy.* Cancer Cell, 2017. **31**(5): p. 711-723 e4.

38. Mackenzie, K.J., et al., *cGAS surveillance of micronuclei links genome instability to innate immunity.* Nature, 2017. **548**(7668): p. 461-465.

39. Harding, S.M., et al., *Mitotic progression following DNA damage enables pattern recognition within micronuclei.* Nature, 2017. **548**(7668): p. 466-470.

40. Xiao, Y., et al., *The kinase TBK1 functions in dendritic cells to regulate T cell homeostasis, autoimmunity, and antitumor immunity.* J Exp Med, 2017. **214**(5): p. 1493-1507.

41. Desch, A.N., et al., *Dendritic cell subsets require cis-activation for cytotoxic CD8 T-cell induction.* Nat Commun, 2014. **5**: p. 4674.

42. Takeda, Y., et al., *A TLR3-Specific Adjuvant Relieves Innate Resistance to PD-L1 Blockade without Cytokine Toxicity in Tumor Vaccine Immunotherapy.* Cell Rep, 2017. **19**(9): p. 1874-1887.

43. Chiba, S., et al., *Tumor-infiltrating DCs suppress nucleic acid-mediated innate immune responses through interactions between the receptor TIM-3 and the alarmin HMGB1.* Nat Immunol, 2012. **13**(9): p. 832-42.

44. Scaffidi, P., T. Misteli, and M.E. Bianchi, *Release of chromatin protein HMGB1 by necrotic cells triggers inflammation.* Nature, 2002. **418**(6894): p. 191-5.

45. Hatakeyama, S., *TRIM Family Proteins: Roles in Autophagy, Immunity, and Carcinogenesis.* Trends Biochem Sci, 2017. **42**(4): p. 297-311.

46. Shi, M., et al., *TRIM30 alpha negatively regulates TLR-mediated NF-kappa B activation by targeting TAB2 and TAB3 for degradation.* Nat Immunol, 2008. **9**(4): p. 369-77.

47. Seo, G.J., et al., *TRIM56-mediated monoubiquitination of cGAS for cytosolic DNA sensing.* Nat Commun, 2018. **9**(1): p. 613.

48. Gack, M.U., et al., *TRIM25 RING-finger E3 ubiquitin ligase is essential for RIG-I-mediated antiviral activity.* Nature, 2007. **446**(7138): p. 916-920.

49. Peisley, A., et al., *Structural basis for ubiquitin-mediated antiviral signal activation by RIG-I.* Nature, 2014. **509**(7498): p. 110-4.

50. Yan, J., et al., *TRIM4 modulates type I interferon induction and cellular antiviral response by targeting RIG-I for K63-linked ubiquitination.* J Mol Cell Biol, 2014. **6**(2): p. 154-63.

51. McEwan, W.A., et al., *Intracellular antibody-bound pathogens stimulate immune signaling via the Fc receptor TRIM21.* Nat Immunol, 2013. **14**(4): p. 327-36.

52. Clift, D., et al., *A Method for the Acute and Rapid Degradation of Endogenous Proteins.* Cell, 2017. **171**(7): p. 1692-1706 e18.

53. Grumati, P. and I. Dikic, *Ubiquitin signaling and autophagy.* J Biol Chem, 2017.

54. Mandell, M.A., et al., *TRIM proteins regulate autophagy and can target autophagic substrates by direct recognition.* Dev Cell, 2014. **30**(4): p. 394-409.

55. Sang, Y., et al., *TRIM59 promotes gliomagenesis by inhibiting TC45 dephosphorylation of STAT3.* Cancer Res, 2018.

56. Zhou, Z., et al., *TRIM59 is up-regulated in gastric tumors, promoting ubiquitination and degradation of p53.* Gastroenterology, 2014. **147**(5): p. 1043-54.

57. Khetchoumian, K., et al., *Loss of Trim24 (Tif1alpha) gene function confers oncogenic activity to retinoic acid receptor alpha.* Nat Genet, 2007. **39**(12): p. 1500-6.

58. Pineda, C.T., et al., *Degradation of AMPK by a cancer-specific ubiquitin ligase.* Cell, 2015. **160**(4): p. 715-28.

59. Ai, L., et al., *TRIM29 suppresses TWIST1 and invasive breast cancer behavior.* Cancer Res, 2014. **74**(17): p. 4875-87.

60. Masuda, Y., et al., *TRIM29 regulates the assembly of DNA repair proteins into damaged chromatin.* Nat Commun, 2015. **6**: p. 7299.

61. Koliopoulos, M.G., et al., *Functional role of TRIM E3 ligase oligomerization and regulation of catalytic activity.* EMBO J, 2016. **35**(11): p. 1204-18.

62. Chen, L. and D.B. Flies, *Molecular mechanisms of T cell co-stimulation and co-inhibition.* Nat Rev Immunol, 2013. **13**(4): p. 227-42.

63. Zhang, Q. and D.A. Vignali, *Co-stimulatory and Co-inhibitory Pathways in Autoimmunity.* Immunity, 2016. **44**(5): p. 1034-51.

64. Tan, P., et al., *Optogenetic Immunomodulation: Shedding Light on Antitumor Immunity.* Trends Biotechnol, 2017. **35**(3): p. 215-226.

65. Chen, B.J., et al., *PD-L1 expression is characteristic of a subset of aggressive B-cell lymphomas and virus-associated malignancies.* Clin Cancer Res, 2013. **19**(13): p. 3462-73.

66. Mitteldorf, C., et al., *Tumor Microenvironment and Checkpoint Molecules in Primary Cutaneous Diffuse Large B-Cell Lymphoma-New Therapeutic Targets.* Am J Surg Pathol, 2017. **41**(7): p. 998-1004.

67. Xu, C., et al., *Loss of Lkb1 and Pten leads to lung squamous cell carcinoma with elevated PD-L1 expression.* Cancer Cell, 2014. **25**(5): p. 590-604.

68. Casey, S.C., et al., *MYC regulates the antitumor immune response through CD47 and PD-L1.* Science, 2016. **352**(6282): p. 227-31.

69. Dorand, R.D., et al., *Cdk5 disruption attenuates tumor PD-L1 expression and promotes antitumor immunity.* Science, 2016. **353**(6297): p. 399-403.

70. Sivan, A., et al., *Commensal Bifidobacterium promotes antitumor immunity and facilitates anti-PD-L1 efficacy.* Science, 2015. **350**(6264): p. 1084-9.

71. Shalapour, S., et al., *Inflammation-induced IgA+ cells dismantle anti-liver cancer immunity.* Nature, 2017. **551**(7680): p. 340-345.

72. Marvel, D. and D.I. Gabrilovich, *Myeloid-derived suppressor cells in the tumor microenvironment: expect the unexpected.* J Clin Invest, 2015. **125**(9): p. 3356-64.

73. Gabrilovich, D.I. and S. Nagaraj, *Myeloid-derived suppressor cells as regulators of the immune system.* Nat Rev Immunol, 2009. **9**(3): p. 162-74.

74. Jitschin, R., et al., *CLL-cells induce IDOhi CD14+HLA-DRlo myeloid-derived suppressor cells that inhibit T-cell responses and promote TRegs.* Blood, 2014. **124**(5): p. 750-60.

75. Roussel, M., et al., *Regulatory myeloid cells: an underexplored continent in B-cell lymphomas.* Cancer Immunol Immunother, 2017. **66**(8): p. 1103-1111.

76. Lu, X., et al., *Effective combinatorial immunotherapy for castration-resistant prostate cancer.* Nature, 2017. **543**(7647): p. 728-732.

77. Wang, G., et al., *Targeting YAP-Dependent MDSC Infiltration Impairs Tumor Progression.* Cancer Discov, 2016. **6**(1): p. 80-95.

78. Lim, S.O., et al., *Deubiquitination and Stabilization of PD-L1 by CSN5.* Cancer Cell, 2016. **30**(6): p. 925-939.

79. Gordon, S.R., et al., *PD-1 expression by tumour-associated macrophages inhibits phagocytosis and tumour immunity.* Nature, 2017. **545**(7655): p. 495-499.

80. Deretic, V., T. Saitoh, and S. Akira, *Autophagy in infection, inflammation and immunity.* Nat Rev Immunol, 2013. **13**(10): p. 722-37.

81. Zhong, Z., E. Sanchez-Lopez, and M. Karin, *Autophagy, Inflammation, and Immunity: A Troika Governing Cancer and Its Treatment.* Cell, 2016. **166**(2): p. 288-298.

82. Kim, J., et al., *AMPK and mTOR regulate autophagy through direct phosphorylation of Ulk1.* Nat Cell Biol, 2011. **13**(2): p. 132-41.

83. Kim, J., et al., *Differential regulation of distinct Vps34 complexes by AMPK in nutrient stress and autophagy.* Cell, 2013. **152**(1-2): p. 290-303.

84. Russell, R.C., et al., *ULK1 induces autophagy by phosphorylating Beclin-1 and activating VPS34 lipid kinase.* Nat Cell Biol, 2013. **15**(7): p. 741-50.

85. Mizushima, N., et al., *Mouse Apg16L, a novel WD-repeat protein, targets to the autophagic isolation membrane with the Apg12-Apg5 conjugate.* J Cell Sci, 2003. **116**(Pt 9): p. 1679-88.

86. Johansen, T. and T. Lamark, *Selective autophagy mediated by autophagic adapter proteins.* Autophagy, 2011. **7**(3): p. 279-96.

87. Stolz, A., A. Ernst, and I. Dikic, *Cargo recognition and trafficking in selective autophagy.* Nat Cell Biol, 2014. **16**(6): p. 495-501.

88. Weidberg, H., E. Shvets, and Z. Elazar, *Biogenesis and cargo selectivity of autophagosomes.* Annu Rev Biochem, 2011. **80**: p. 125-56.

89. Martinez, J., et al., *Molecular characterization of LC3-associated phagocytosis reveals distinct roles for Rubicon, NOX2 and autophagy proteins.* Nat Cell Biol, 2015. **17**(7): p. 893-906.

90. Starr, T., et al., *Selective subversion of autophagy complexes facilitates completion of the Brucella intracellular cycle.* Cell Host Microbe, 2012. **11**(1): p. 33-45.

91. Choi, J., et al., *The parasitophorous vacuole membrane of Toxoplasma gondii is targeted for disruption by ubiquitin-like conjugation systems of autophagy.* Immunity, 2014. **40**(6): p. 924-35.

92. Hwang, S., et al., *Nondegradative role of Atg5-Atg12/ Atg16L1 autophagy protein complex in antiviral activity of interferon gamma.* Cell Host Microbe, 2012. **11**(4): p. 397-409.

93. Kimmey, J.M., et al., *Unique role for ATG5 in neutrophil-mediated immunopathology during M. tuberculosis infection.* Nature, 2015. **528**(7583): p. 565-9.

94. Saitoh, T., et al., *Atg9a controls dsDNA-driven dynamic translocation of STING and the innate immune response.* Proc Natl Acad Sci U S A, 2009. **106**(49): p. 20842-6.

95. Matsuzawa-Ishimoto, Y., S. Hwang, and K. Cadwell, *Autophagy and Inflammation.* Annu Rev Immunol, 2017.

96. Lei, Y., et al., *The mitochondrial proteins NLRX1 and TUFM form a complex that regulates type I interferon and autophagy.* Immunity, 2012. **36**(6): p. 933-46.

97. Liang, Q., et al., *Crosstalk between the cGAS DNA sensor and Beclin-1 autophagy protein shapes innate antimicrobial immune responses.* Cell Host Microbe, 2014. **15**(2): p. 228-38.

98. Konno, H., K. Konno, and G.N. Barber, *Cyclic dinucleotides trigger ULK1 (ATG1) phosphorylation of STING to prevent sustained innate immune signaling.* Cell, 2013. **155**(3): p. 688-98.

99. Zhao, P., et al., *TBK1 at the Crossroads of Inflammation and Energy Homeostasis in Adipose Tissue.* Cell, 2018. **172**(4): p. 731-743 e12.

100. Pickup, M., S. Novitskiy, and H.L. Moses, *The roles of TGFbeta in the tumour microenvironment.* Nat Rev Cancer, 2013. **13**(11): p. 788-99.

101. Moscat, J., M. Karin, and M.T. Diaz-Meco, *p62 in Cancer: Signaling Adaptor Beyond Autophagy.* Cell, 2016. **167**(3): p. 606-609.

102. Cianfanelli, V., et al., *AMBRA1 links autophagy to cell proliferation and tumorigenesis by promoting c-Myc dephosphorylation and degradation.* Nat Cell Biol, 2015. **17**(5): p. 706.

103. Takahashi, Y., et al., *Bif-1 interacts with Beclin 1 through UVRAG and regulates autophagy and tumorigenesis.* Nat Cell Biol, 2007. **9**(10): p. 1142-51.

104. White, E., *The role for autophagy in cancer.* J Clin Invest, 2015. **125**(1): p. 42-6.

105. Galluzzi, L., et al., *Autophagy in malignant transformation and cancer progression.* EMBO J, 2015. **34**(7): p. 856-80.

106. Sun, T., et al., *Acetylation of Beclin 1 inhibits autophagosome maturation and promotes tumour growth.* Nat Commun, 2015. **6**: p. 7215.

107. Wang, R.C., et al., *Akt-mediated regulation of autophagy and tumorigenesis through Beclin 1 phosphorylation.* Science, 2012. **338**(6109): p. 956-9.

108. Wei, Y., et al., *EGFR-mediated Beclin 1 phosphorylation in autophagy suppression, tumor progression, and tumor chemoresistance.* Cell, 2013. **154**(6): p. 1269-84.

109. Liu, J., et al., *Beclin1 controls the levels of p53 by regulating the deubiquitination activity of USP10 and USP13.* Cell, 2011. **147**(1): p. 223-34.

110. Elgendy, M., et al., *Beclin 1 restrains tumorigenesis through Mcl-1 destabilization in an autophagy-independent reciprocal manner.* Nat Commun, 2014. **5**: p. 5637.

111. Elgendy, M., et al., *Oncogenic Ras-induced expression of Noxa and Beclin-1 promotes autophagic cell death and limits clonogenic survival.* Mol Cell, 2011. **42**(1): p. 23-35.

112. Katheder, N.S., et al., *Microenvironmental autophagy promotes tumour growth.* Nature, 2017. **541**(7637): p. 417-420.

113. Liu, H.M., et al., *The mitochondrial targeting chaperone 14-3-3ε regulates a RIG-I translocon that mediates membrane association and innate antiviral immunity.* Cell host & microbe, 2012. **11**(5): p. 528-537.

114. Shigemoto, T., et al., *Identification of loss of function mutations in human genes encoding RIG-I and MDA5: implications for resistance to type I diabetes.* J Biol Chem, 2009. **284**(20): p. 13348-54.

115. Subramanian, N., et al., *The adaptor MAVS promotes NLRP3 mitochondrial localization and inflammasome activation.* Cell, 2013. **153**(2): p. 348-361.

116. Willemsen, J., et al., *Phosphorylation-Dependent Feedback Inhibition of RIG-I by DAPK1 Identified by Kinome-wide siRNA Screening.* Mol Cell, 2017. **65**(3): p. 403-415 e8.

117. Leuzzi, G., et al., *WRNIP1 protects stalled forks from degradation and promotes fork restart after replication stress.* EMBO J, 2016. **35**(13): p. 1437-51.

118. Bish, R.A. and M.P. Myers, *Werner helicase-interacting protein 1 binds polyubiquitin via its zinc finger domain.* J Biol Chem, 2007. **282**(32): p. 23184-93.

119. Bonilla, X., et al., *Genomic analysis identifies new drivers and progression pathways in skin basal cell carcinoma.* Nat Genet, 2016. **48**(4): p. 398-406.

120. Zeng, K., et al., *Protein phosphatase 6 regulates mitotic spindle formation by controlling the T-loop phosphorylation state of Aurora A bound to its activator TPX2.* J Cell Biol, 2010. **191**(7): p. 1315-32.

121. Ma, G., et al., *Inside-out Ca(2+) signalling prompted by STIM1 conformational switch.* Nat Commun, 2015. **6**: p. 7826.

122. He, L., et al., *Optical control of membrane tethering and interorganellar communication at nanoscales.* Chemical Science, 2017.

123. Cui, J., et al., *USP3 inhibits type I interferon signaling by deubiquitinating RIG-I-like receptors.* Cell Res, 2014. **24**(4): p. 400-16.

124. He, L., et al., *Near-infrared photoactivatable control of Ca(2+) signaling and optogenetic immunomodulation.* Elife, 2015. **4**.

125. Jing, J., et al., *Proteomic mapping of ER-PM junctions identifies STIMATE as a regulator of Ca(2)(+) influx.* Nat Cell Biol, 2015. **17**(10): p. 1339-47.

126. Crosetto, N., et al., *Human Wrnip1 is localized in replication factories in a ubiquitin-binding zinc finger-dependent manner.* J Biol Chem, 2008. **283**(50): p. 35173-85.

127. Zeng, W., et al., *Reconstitution of the RIG-I pathway reveals a signaling role of unanchored polyubiquitin chains in innate immunity.* Cell, 2010. **141**(2): p. 315-30.

128. Sun, X., et al., *A Hierarchical Mechanism of RIG-I Ubiquitination Provides Sensitivity, Robustness and Synergy in Antiviral Immune Responses.* Sci Rep, 2016. **6**: p. 29263.

129. Myong, S., et al., *Cytosolic Viral Sensor RIG-I Is a 5'-Triphosphate–Dependent Translocase on Double-Stranded RNA*. Science, 2009. **323**(5917): p. 1070-1074.

130. Tsurimoto, T., et al., *Human Werner helicase interacting protein 1 (WRNIP1) functions as a novel modulator for DNA polymerase delta.* Genes Cells, 2005. **10**(1): p. 13-22.

131. Hammond, D., et al., *Melanoma-associated mutations in protein phosphatase 6 cause chromosome instability and DNA damage owing to dysregulated Aurora-A*. J Cell Sci, 2013. **126**(Pt 15): p. 3429-40.

132. Mesman, A.W., et al., *Measles virus suppresses RIG-I-like receptor activation in dendritic cells via DC-SIGN-mediated inhibition of PP1 phosphatases.* Cell Host Microbe, 2014. **16**(1): p. 31-42.

133. Stefansson, B. and D.L. Brautigan, *Protein phosphatase 6 subunit with conserved Sit4-associated protein domain targets IkappaBepsilon.* J Biol Chem, 2006. **281**(32): p. 22624-34.

134. Nistal-Villan, E., et al., *Negative role of RIG-I serine 8 phosphorylation in the regulation of interferon-beta production.* J Biol Chem, 2010. **285**(26): p. 20252-61.

135. Hoeller, D., C.M. Hecker, and I. Dikic, *Ubiquitin and ubiquitin-like proteins in cancer pathogenesis.* Nat Rev Cancer, 2006. **6**(10): p. 776-88.

136. Patel, J.R., et al., *ATPase-driven oligomerization of RIG-I on RNA allows optimal activation of type-I interferon.* EMBO Rep, 2013. **14**(9): p. 780-7.

137. Louber, J., et al., *Kinetic discrimination of self/non-self RNA by the ATPase activity of RIG-I and MDA5.* BMC Biol, 2015. **13**: p. 54.

138. Lassig, C., et al., *ATP hydrolysis by the viral RNA sensor RIG-I prevents unintentional recognition of self-RNA.* Elife, 2015. **4**.

139. Hayakawa, S., et al., *ZAPS is a potent stimulator of signaling mediated by the RNA helicase RIG-I during antiviral responses.* Nat Immunol, 2011. **12**(1): p. 37-44.

140. Hodis, E., et al., *A landscape of driver mutations in melanoma.* Cell, 2012. **150**(2): p. 251-63.

141. Lorin, S., et al., *Autophagy regulation and its role in cancer.* Semin Cancer Biol, 2013. **23**(5): p. 361-79.

142. Yue, Z., et al., *Beclin 1, an autophagy gene essential for early embryonic development, is a haploinsufficient tumor suppressor.* Proc Natl Acad Sci U S A, 2003. **100**(25): p. 15077-82.

143. Qu, X., et al., *Promotion of tumorigenesis by heterozygous disruption of the beclin 1 autophagy gene.* J Clin Invest, 2003. **112**(12): p. 1809-20.

144. Parkhitko, A., et al., *Tumorigenesis in tuberous sclerosis complex is autophagy and p62/sequestosome 1 (SQSTM1)-dependent.* Proc Natl Acad Sci U S A, 2011. **108**(30): p. 12455-60.

145. Grivennikov, S.I., F.R. Greten, and M. Karin, *Immunity, inflammation, and cancer.* Cell, 2010. **140**(6): p. 883-99.

146. Newton, K. and V.M. Dixit, *Signaling in innate immunity and inflammation.* Cold Spring Harb Perspect Biol, 2012. **4**(3).

147. Rickert, R.C., *New insights into pre-BCR and BCR signalling with relevance to B cell malignancies.* Nat Rev Immunol, 2013. **13**(8): p. 578-91.

148. Scott, D.W. and R.D. Gascoyne, *The tumour microenvironment in B cell lymphomas.* Nat Rev Cancer, 2014. **14**(8): p. 517-34.

149. Salvador, E., M. Burek, and C.Y. Forster, *Tight Junctions and the Tumor Microenvironment.* Curr Pathobiol Rep, 2016. **4**: p. 135-145.

150. Goodman, A., S.P. Patel, and R. Kurzrock, *PD-1-PD-L1 immune-checkpoint blockade in B-cell lymphomas.* Nat Rev Clin Oncol, 2017. **14**(4): p. 203-220.

151. Engel, F.B., et al., *p38 MAP kinase inhibition enables proliferation of adult mammalian cardiomyocytes.* Genes Dev, 2005. **19**(10): p. 1175-87.

152. Heckl, D., et al., *Generation of mouse models of myeloid malignancy with combinatorial genetic lesions using CRISPR-Cas9 genome editing.* Nat Biotechnol, 2014. **32**(9): p. 941-6.

153. Trapnell, C., L. Pachter, and S.L. Salzberg, *TopHat: discovering splice junctions with RNA-Seq.* Bioinformatics, 2009. **25**(9): p. 1105-11.

154. Love, M.I., W. Huber, and S. Anders, *Moderated estimation of fold change and dispersion for RNA-seq data with DESeq2.* Genome Biol, 2014. **15**(12): p. 550.

155. Subramanian, A., et al., *Gene set enrichment analysis: a knowledge-based approach for interpreting genome-wide expression profiles.* Proc Natl Acad Sci U S A, 2005. **102**(43): p. 15545-50.

156. Daley, J.M., et al., *Use of Ly6G-specific monoclonal antibody to deplete neutrophils in mice.* J Leukoc Biol, 2008. **83**(1): p. 64-70.

157. Jenssen, T.K., et al., *A literature network of human genes for high-throughput analysis of gene expression.* Nat Genet, 2001. **28**(1): p. 21-8.

158. Huang da, W., B.T. Sherman, and R.A. Lempicki, *Systematic and integrative analysis of large gene lists using DAVID bioinformatics resources.* Nat Protoc, 2009. **4**(1): p. 44-57.

159. Dong, C., *TH17 cells in development: an updated view of their molecular identity and genetic programming.* Nat Rev Immunol, 2008. **8**(5): p. 337-48.

160. Withers, D.R., et al., *Transient inhibition of ROR-gammat therapeutically limits intestinal inflammation by reducing TH17 cells and preserving group 3 innate lymphoid cells.* Nat Med, 2016. **22**(3): p. 319-23.

161. Xiao, S., et al., *Small-molecule RORgammat antagonists inhibit T helper 17 cell transcriptional network by divergent mechanisms.* Immunity, 2014. **40**(4): p. 477-89.

162. Xu, P., et al., *Quantitative proteomics reveals the function of unconventional ubiquitin chains in proteasomal degradation.* Cell, 2009. **137**(1): p. 133-45.

163. Cong, L., et al., *Multiplex genome engineering using CRISPR/Cas systems.* Science, 2013. **339**(6121): p. 819-23.

164. Nie, Y., et al., *The role of CXCR4 in maintaining peripheral B cell compartments and humoral immunity.* J Exp Med, 2004. **200**(9): p. 1145-56.

165. Allende, M.L., et al., *S1P1 receptor directs the release of immature B cells from bone marrow into blood.* J Exp Med, 2010. **207**(5): p. 1113-24.

166. Somasundaram, R., et al., *Transcription factor networks in B-cell differentiation link development to acute lymphoid leukemia.* Blood, 2015. **126**(2): p. 144-52.

167. Puga, I., et al., *B cell-helper neutrophils stimulate the diversification and production of immunoglobulin in the marginal zone of the spleen.* Nat Immunol, 2011. **13**(2): p. 170-80.

168. Cerutti, A., I. Puga, and G. Magri, *The B cell helper side of neutrophils.* J Leukoc Biol, 2013. **94**(4): p. 677-82.

169. Gatjen, M., et al., *Splenic Marginal Zone Granulocytes Acquire an Accentuated Neutrophil B-Cell Helper Phenotype in Chronic Lymphocytic Leukemia.* Cancer Res, 2016. **76**(18): p. 5253-65.

170. Sangaletti, S., et al., *Defective stromal remodeling and neutrophil extracellular traps in lymphoid tissues favor the transition from autoimmunity to lymphoma.* Cancer Discov, 2014. **4**(1): p. 110-29.

171. Shojaee, S., et al., *PTEN opposes negative selection and enables oncogenic transformation of pre-B cells.* Nat Med, 2016. **22**(4): p. 379-87.

172. Yu, H., D. Pardoll, and R. Jove, *STATs in cancer inflammation and immunity: a leading role for STAT3.* Nat Rev Cancer, 2009. **9**(11): p. 798-809.

173. Malin, S., et al., *Role of STAT5 in controlling cell survival and immunoglobulin gene recombination during pro-B cell development.* Nat Immunol, 2010. **11**(2): p. 171-9.

174. Li, X., et al., *Beclin 1 is required for starvation-enhanced, but not rapamycin-enhanced, LC3-associated phagocytosis of Burkholderia pseudomallei in RAW 264.7 cells.* Infect Immun, 2013. **81**(1): p. 271-7.

175. Baldassare, J.J., Y. Bi, and C.J. Bellone, *The role of p38 mitogen-activated protein kinase in IL-1 beta transcription.* J Immunol, 1999. **162**(9): p. 5367-73.

176. Han, J. and R.J. Ulevitch, *Limiting inflammatory responses during activation of innate immunity.* Nat Immunol, 2005. **6**(12): p. 1198-205.

177. Noubade, R., et al., *Activation of p38 MAPK in CD4 T cells controls IL-17 production and autoimmune encephalomyelitis.* Blood, 2011. **118**(12): p. 3290-300.

178. Mueller, S.N. and R.N. Germain, *Stromal cell contributions to the homeostasis and functionality of the immune system.* Nat Rev Immunol, 2009. **9**(9): p. 618-29.

179. Hendriks, R.W., S. Yuvaraj, and L.P. Kil, *Targeting Bruton's tyrosine kinase in B cell malignancies.* Nat Rev Cancer, 2014. **14**(4): p. 219-32.

180. Beck, T.C., et al., *CXCR4 and a cell-extrinsic mechanism control immature B lymphocyte egress from bone marrow.* J Exp Med, 2014. **211**(13): p. 2567-81.

181. Cyster, J.G. and S.R. Schwab, *Sphingosine-1-phosphate and lymphocyte egress from lymphoid organs.* Annu Rev Immunol, 2012. **30**: p. 69-94.

182. Sarosiek, K.A., et al., *Novel IL-21 signaling pathway up-regulates c-Myc and induces apoptosis of diffuse large B-cell lymphomas.* Blood, 2010. **115**(3): p. 570-80.

183. Ware, C.F., *APRIL and BAFF connect autoimmunity and cancer.* J Exp Med, 2000. **192**(11): p. F35-8.

184. Leonard, W.J. and C.K. Wan, *IL-21 Signaling in Immunity.* F1000Res, 2016. **5**.

185. Jarosinski, K.W. and P.T. Massa, *Interferon regulatory factor-1 is required for interferon-gamma-induced MHC class I genes in astrocytes.* J Neuroimmunol, 2002. **122**(1-2): p. 74-84.

186. Garcia-Diaz, A., et al., *Interferon Receptor Signaling Pathways Regulating PD-L1 and PD-L2 Expression.* Cell Rep, 2017. **19**(6): p. 1189-1201.

187. Zou, W., J.D. Wolchok, and L. Chen, *PD-L1 (B7-H1) and PD-1 pathway blockade for cancer therapy: Mechanisms, response biomarkers, and combinations.* Sci Transl Med, 2016. **8**(328): p. 328rv4.